SLAC-R-569

SLAC-R-569

The Search for Millicharged Particles at SLAC

A. A. Prinz

SLAC-Report-569
March 2001

Prepared for the Department of Energy
under contract number DE-AC03-76SF00515

SLAC-R-569
UC-414

The Search for Millicharged Particles at SLAC*

A. A. Prinz

Stanford Linear Accelerator Center
Stanford University
Stanford, CA 94309

SLAC-Report-569
March 2001

Prepared for the Department of Energy
under contract number DE-AC03-76SF00515

Printed in the United States of America. Available from the National Technical Information Service, U.S. Department of Commerce, 5285 Port Royal Road, Springfield, VA 22161.

*Ph.D. thesis, Stanford University, Stanford, CA 94309.

THE SEARCH FOR MILLICHARGED PARTICLES AT SLAC

A DISSERTATION
SUBMITTED TO THE DEPARTMENT OF PHYSICS
AND THE COMMITTEE ON GRADUATE STUDIES
OF STANFORD UNIVERSITY
IN PARTIAL FULFILLMENT OF THE REQUIREMENTS
FOR THE DEGREE OF
DOCTOR OF PHILOSOPHY

Alyssa A. Prinz
March 2001

Abstract

Quantization of electric charge has been probed to a high degree of precision using a variety of experimental techniques. However, the theoretical underpinning of charge quantization has yet to be determined, leaving open the possibility that quantization is not a fundamental law of nature, and that free particles with fractional electric charge may one day be encountered. This dissertation describes a search for particles with very small ($10^{-3}\,e$ or below) electric charge, carried out at an electron accelerator (SLAC). The particles sought were assumed to be long lived or stable and to participate primarily in electromagnetic interactions. The search relied upon a large (1.3-meter) scintillation counter to detect low levels of ionization generated by relativistic fractionally charged particles produced in the collision of a 29.5-GeV electron beam with a six radiation length tungsten target. The data reveal no evidence of fractional charge, and allow for the exclusion of a portion of charge-mass parameter space spanning roughly 10^{-7} to 10^{2} MeV/c^2 and 10^{-2} to $10^{-5}\,e$.

Acknowledgments

There are numerous individuals without whom this work would would not have been possible, and I will mention just a few of them here.

My thanks go to the Millicharge Collaboration, for conceiving of, designing and building the experiment; Morris Swartz for writing the production Monte Carlo; and Michael Peskin and Sacha Davidson for discussions of the theoretical implications of the existence of millicharged particles.

Special thanks to my advisor John Jaros, for his patience and constant encouragement; to Willy Langeveld, for assistance with everything from the writing of the analysis code to the creation of the figures in this document; and to Julie Wroblesky, Anne Matsuura, Robin Erbacher, and Ralph and Kay Nelson, for keeping me sane with their unwavering companionship and good cheer.

And to my family, without whose encouragement, support, love and faith in me I could never have come this far, goes my undying gratitude. To my mother Pat and my father Rudolph, to Vera Prinz, Hugh MacMahon and Jane Sillman, I am infinitely indebted.

This dissertation is dedicated to the memory of Boots Nelson.

Contents

List of Tables

List of Figures

Chapter 1

Introduction

Quantization of electric charge is a principle supported by a great deal of experimental evidence. Violations of this principle have been sought using a wide variety of experimental techniques (including some that have probed the neutron charge and the proton–electron charge difference to the astonishing precision of $10^{-21}\,e$, where e is the electron charge[1, 2, 3]), without ever achieving a reproducible positive result. But the mechanism that leads to quantization of charge remains elusive, and the possibility of encountering free fractional charge in a context not yet examined experimentally (*e.g.,* in a new particle species) or of a magnitude below the current experimental precision, has not yet been eliminated.

In the Minimal Standard Model, without the additional constraint of equality of quantum numbers between the three lepton families, charge quantization is not inevitable. Deviations characterized by a small charge difference between two of the three charged leptons, and a finite charge on two of the three neutrinos, are permissible[4]. In order to be in agreement with experimental evidence sensitive to neutrino charge, these deviations must be of order $10^{-9}\,e$ or smaller. The possible fractional charges of exotic particle species are not subject to this constraint.

Grand Unified Theories in general enforce quantization of charge. But even in this context there exist mechanisms that could lead to an observation of apparent fractional charge. These mechanisms pertain in the case that the gauge group describing particle interactions at low energy contains more than one U(1) (electromagnetism) factor. Under certain circumstances (proposed in the theoretical discussions of Holdom[5, 6]), charged fermions in an additional U(1) could interact with normal fermions as though they carried conventional electric charge of non-standard magnitude. There would be no genuine violation of charge quantization in this scenario: within their own U(1), the charge values of the exotic fermions remain quantized. The possibility to find evidence of particles dwelling within an alternate U(1) provides additional motivation for the search for fractional charge.

In light of the lack of a theoretical underpinning for charge quantization, and the compelling but nonetheless inconclusive experimental evidence in its favor, continued efforts to seek evidence of fractional electric charge are warranted.

Certain values of charge and mass are excluded by the results of direct measurements and by cosmological and astrophysical predictions that would be affected by the existence of fractionally charged particles. The portions of charge-mass parameter space ruled out by direct measurements, which include previous searches for fractional charge, as well as a precise measurement of the Lamb shift, are shown in Figure 1.1. Areas excluded on the basis of Big Bang Nucleosynthesis and the total mass density of the universe (sufficiently low that the universe not be overclosed) are also shown in Figure 1.1. Regions ruled out on the basis of astrophysical arguments, such as the effect of light fractionally charged particles on the cooling rate of stars, are shown in Figure 1.2. (A detailed discussion of these excluded regions will be given in the next chapter.) The yellow region on the upper right side of Figure 1.1, spanning mass values between 1 MeV/$c^2$and 1 GeV/c^2, and charge values between 10^{-2} and $10^{-6}\,e$, represents an area that is not excluded by any of the above considerations.

The experiment described in this thesis was designed to investigate a portion of this unexplored area. Specifically, it was a search for particles with tiny electric charge ($q \lesssim 10^{-3}\,e$) and mass below about 100 MeV/c^2, that are stable (or fairly

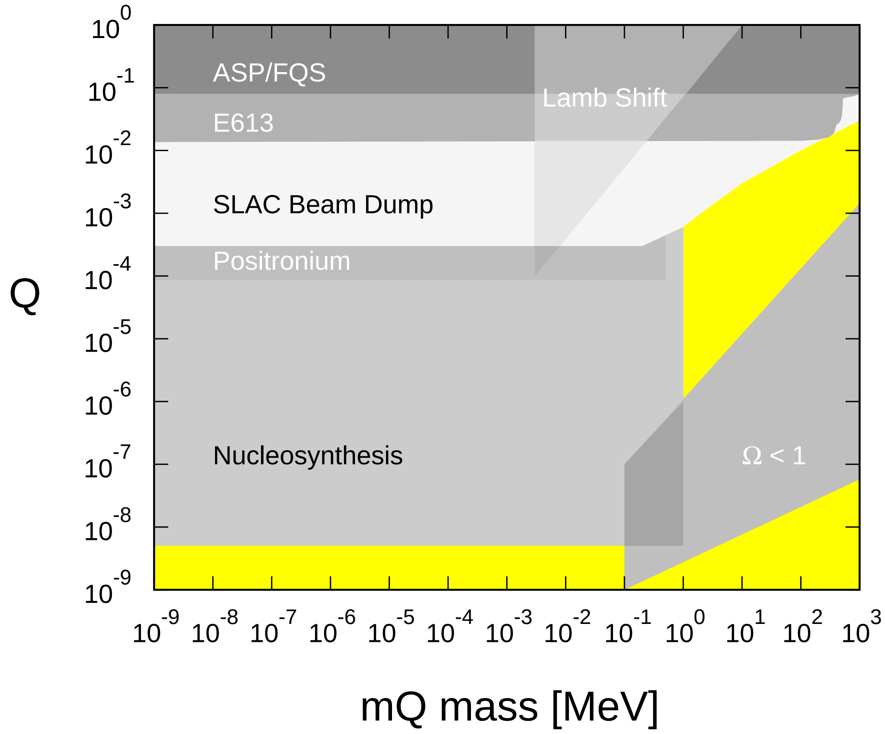

Figure 1.1: Regions of charge-mass parameter space ruled out by direct measurements and by cosmological arguments. Unexplored regions are shown in yellow.

long lived) and subject only to electromagnetic and gravitational interactions. These "millicharged" particles, or "mQs" as we will refer to them, would interact very weakly. Over most of their charge-mass parameter range they would be incapable of forming bound states with matter, and would have a very low probability for interaction in a typical detector. Their range in matter would be far greater than standard charged particles (by a factor of Q^{-2}, where Q is the charge in units of e), with ionization being their primary means of energy loss.

We searched for mQs at a particle accelerator, in a beam-dump type of experiment. There are several advantages to this approach. An accelerator has the potential to produce both conventional particles and exotic species in high abundance. A beam dump arrangement allows for generation of a beam of the particles of interest, providing maximal flux into an appropriately placed detector. And, in contrast to

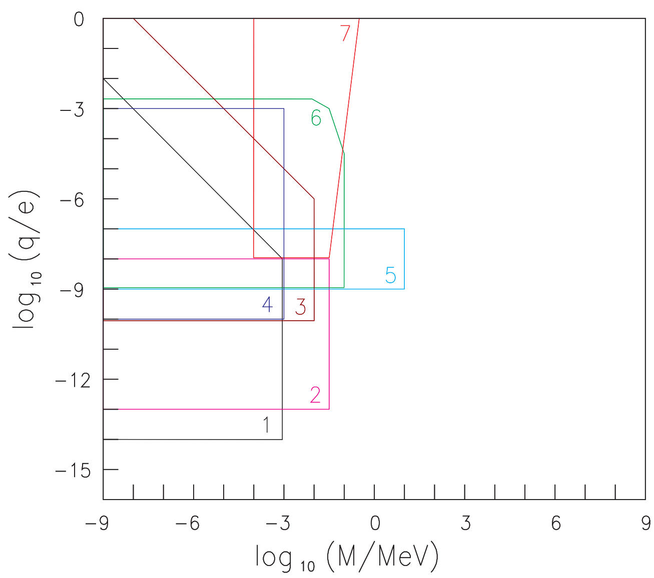

Figure 1.2: Regions of charge-mass parameter space excluded by astrophysical arguments. 1. Plasmon decay and heat conduction in red giants. 2. Cooling rate of white dwarfs. 3. Cooling rate of white dwarfs. 4. Energy loss from the sun. 5. Energy loss from SN 1987A. 6. Heat transport in red giants. 7. Hidden-sector photon emission from red giants.

many other search techniques, there is no need for the particles to be bound up in samples of matter.

We located our search at the Stanford Linear Accelerator Center (SLAC). An electron accelerator such as SLAC was deemed the ideal facility by Dobroliubov and Ignatiev[7], who first proposed a search for mQs. SLAC generates a high-current electron beam (3×10^{10} electrons per bunch, at 120 bunches per second) with very short (~ 10 picoseconds) bunch duration. There is an advantage associated with short bunch time: improvement in the signal-to-noise ratio of the experiment (by orders of magnitude) can be achieved by restricting data collection to a narrow window surrounding the bunch arrival time. When the SLAC beam strikes a solid target, electromagnetic showers are generated. The abundance of relativistic electrons and positrons in the shower is ideal for producing large numbers of mQs.

Our experiment was designed to detect the ionization trail of a passing relativistic mQ. For this we used a scintillation counter with a long (1.3-meter) path length for mQs, that was designed to have the best possible sensitivity to the smallest energy deposition (a single ionization). (With such a low cross section for interaction, the most likely outcome of a mQ crossing 1.3 meters of scintillator, other than no interaction at all, would be a single ionization.) We placed our detector along the axis of the beam of electrons incident on SLAC's SLC positron production target (a metal target six radiation lengths in thickness), on the downstream side. We arranged to have sufficient material between the target and detector to shield out all conventionally charged particles, leaving only neutrinos, mQs, and a small number of neutrons capable of reaching the detector. A Monte Carlo simulation of mQ production in the target predicted the mQ beam to be quite narrow: $\theta \lesssim 20$ milliradians. Our detector covered angles up to 2 milliradians, providing an acceptance, according to the predicted mQ angular distribution, of roughly 20%.

We recorded the time and pulse height of events occurring within roughly 100 nanoseconds of the predicted arrival time of mQ bunches at the detector. The presence of mQs would be most readily discernible by a peak (a few tens of nanoseconds wide) in the time spectrum of these events.

The chapters that follow will provide a detailed discussion of theoretical issues relevant to mQs; our methods for predicting the number of mQs that should arrive at the detector; our experiment setup and the expected signature of mQs therein; our analysis technique; and the experiment's results.

Chapter 2

Theoretical Background

2.1 Introduction

There is compelling empirical evidence that the electric charges of free elementary particles are quantized. A large number of experiments seeking evidence of fractional charge (by which we mean any charge q not equal to an integral multiple of e) have been performed, without a single (reproducible) positive result. But there is insufficient experimental evidence to completely rule out the possibility of a particle having fractional charge, particularly if the charge is very small in relation to e. And we have, as yet, no experimentally verified model that can provide insight into the mechanism that leads to charge quantization. This chapter will explore some of the experimental and theoretical background relevant to a search for particles with small fractional charge, including the evidence in favor of quantization, some appealing extensions of the Standard Model that would provide an explanation for quantization, a number of models that do not involve quantization (including the Minimal Standard Model), and a review of the constraints on fractionally charged particles imposed by the available experimental evidence.

The chapter begins with a short summary of the properties of the fractionally charged particles ("millicharged particles" or "mQs") sought in the present experiment, followed by a discussion of the experimental evidence in favor of charge quantization. Quantization (or rather, the lack thereof) in the Minimal Standard Model is explored in some detail. Two appealing new-physics possibilities (grand unification, and the existence of magnetic monopoles) which would provide an explanation for charge quantization are described, along with a mechanism (involving multiple U(1) factors in the gauge group) by which particles whose charge was truly quantized could exhibit an apparent fractional charge. The set of models capable of accommodating fractional charge via this mechanism is surveyed briefly, followed by a description of some rather speculative models in which charge is neither quantized nor conserved. The remainder of the chapter is devoted to a discussion of the parameter space (in charge and mass) that can be excluded based upon the available experimental evidence.

2.2 Brief Review of mQ Properties

MQs are stable (or long-lived) particles with electric charge $0 < q \lesssim 10^{-3}\,e$. For purposes of calculating mQ yield and assessing the interactions of mQs with matter, we assume mQs are fermions that do not participate in the strong or weak interactions. Their coupling to gravity is assumed to be the same as for normal matter.

For certain combinations of mQ charge and mass, a negatively charged mQ can form an electromagnetic bound state with a normal atom. The binding energy is given by $\mu\,(QZc\alpha)^2/2$, where $\mu = \frac{M_{\mathrm{N}} M_{\mathrm{mQ}}}{M_{\mathrm{N}}+M_{\mathrm{mQ}}}$ is the reduced mass of the mQ–nucleus system, Z is the atomic number, and Q is the mQ charge in units of e. The Bohr radius of a bound mQ is given by $a_0 = \hbar/(QZ\mu\, c\, \alpha)$. If the Bohr radius is larger than the average radius of the atom's electron cloud ($r \cong 0.90\, Z^{-1/3}$ in the Thomas-Fermi model), or the binding energy is lower than ambient thermal energy, a stable bound state will not be formed. For silicon at room temperature ($r \cong 0.37$ Å, $k_{\mathrm{B}}T \cong 0.026$ eV), the mQ parameters that permit a bound state are shown in Figure 2.1. Relic mQs or mQs

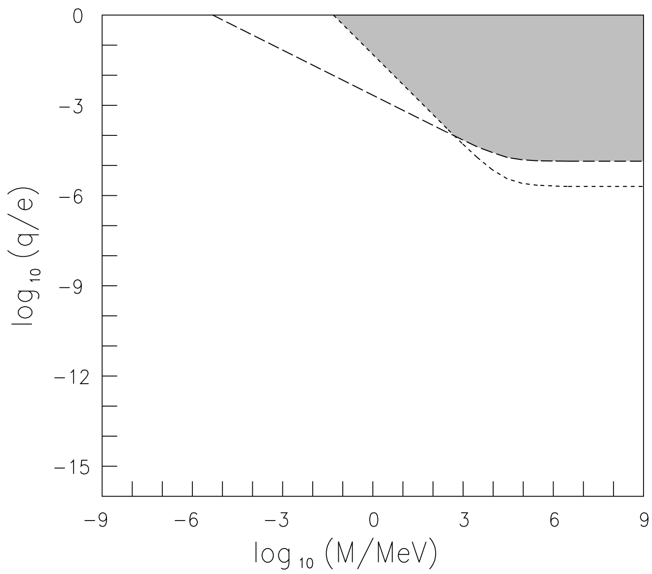

Figure 2.1: Region of charge-mass parameter space in which negative mQs can bind to matter (shaded area). Above the dashed curve, the binding energy is greater than room-temperature thermal energy. Above the dotted curve, the Bohr radius is smaller than the average electron-cloud radius for silicon.

produced in the atmosphere would tend to accumulate in the earth's crust if their parameters lie within the shaded region of the figure, possibly making them amenable to discovery by experiments seeking fractional charge in terrestrial materials. MQs that do not bind to atoms will either pass right through the earth (like neutrinos), or become gravitationally bound, eventually settling into the earth's core. The presence of a significant mass of mQs at the center of the earth would be readily noticed given that mQs do not respond to seismic shock like normal matter, and thus any disturbance (*e.g.,* a meteorite impact or an earthquake) would set up an oscillation between the mQ center of mass and that of the earth [8].

A fast mQ moving through a medium loses energy via ionization and, at high enough energy (or very low mass) via radiative processes. The cross section for elastic scattering from an electron (diagram A in Figure 2.2) is suppressed by a factor of Q^2, where Q is the mQ charge in units of e, relative to that of a charge–1 particle. We therefore expect the ionization energy loss to be well represented by the Bethe-

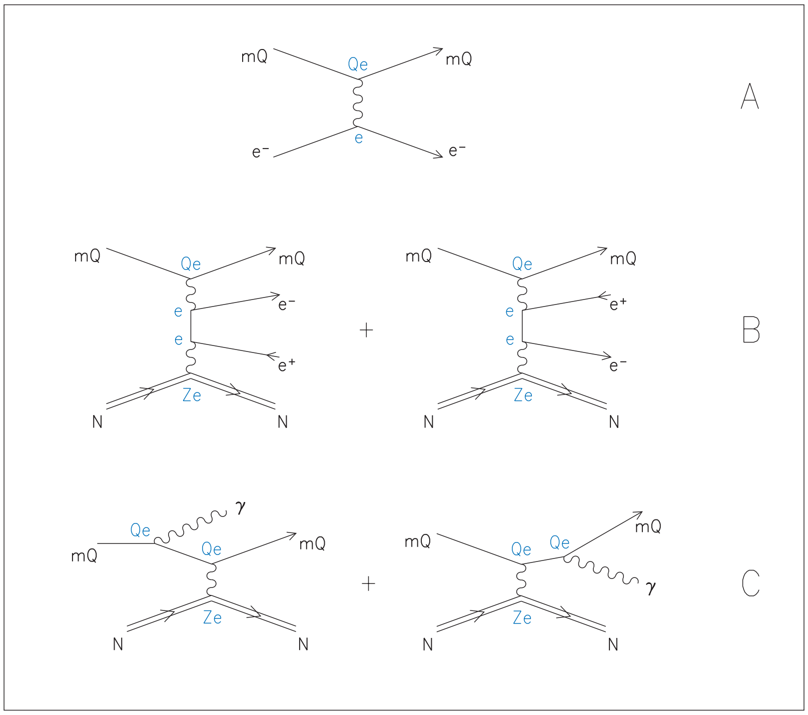

Figure 2.2: Feynman diagrams for mQ energy loss in matter. A. Scattering from atomic electrons (excitation/ionization). B. e^+e^- pair production. C. Bremsstrahlung.

Bloch formula [9], scaled by an overall factor of Q^2. For the radiative processes, e^+e^- pair production is suppressed by Q^2, while Bremsstrahlung is suppressed by Q^4 (the dominant diagrams are shown in Fig. 2.2 B and C). Radiative energy loss mechanisms will be discussed in greater detail in the next chapter. Typical mQ parameters to which our search should be sensitive are $Q = 10^{-4}$ and $M_{\mathrm{mQ}} = 10$ MeV/c^2. A relativistic ($\gamma = 4$) mQ with these parameters would lose about 2×10^{-8}MeV cm^2/g to ionization, and a negligible amount of energy to other processes. It would travel 2×10^6 meters in lead, or 7×10^6 meters in SiO_2 (earth's crust) before coming to a halt.

2.3 Experimental Evidence in Support of Charge Quantization

There is much empirical evidence suggesting that the electric charge of unconfined particles is quantized in units of e. Attempts to uncover deviations from this behavior have been made using several different experimental techniques, but none to date has generated a reproducible positive result. Some of these experimental investigations include the following. The neutron's charge has been probed by seeking deflections in a beam of cold neutrons passing through an electric field [1], resulting in a limit of $|q_{\mathrm{n}}| \lesssim 10^{-21}\, e$. The sum of the electron and proton charges was investigated by applying an alternating electric field to a gas (SF_6) within a resonant cavity containing a sensitive microphone [2]. The absence of detectable sound waves leads to the limit $|q_{\mathrm{e}} + q_{\mathrm{p}}| \leq 1 \times 10^{-21}\, e$. A different experimental method, consisting of observation of the motion of magnetically levitated tiny ($\sim 10^{-5}$g) steel spheres in an alternating electric field [3], has given an almost identical limit: $|q_{\mathrm{e}} + q_{\mathrm{p}}| < 0.8 \times 10^{-21}\, e$. Under the assumption of charge conservation in beta decay, the above results constrain the charge of the electron antineutrino: $|q_{\bar{\nu}_{\mathrm{e}}}| \lesssim 10^{-21}\, e$; by CPT symmetry, the same bound applies to the electron neutrino. (However, the above neutrino bounds involve certain assumptions which have not been tested at the $10^{-21}\, e$ level. See reference [10].) The muon neutrino charge must satisfy $|q_{\nu_\mu}| < 10^{-9}\, e$ in order not to violate agreement between the theoretical and measured cross sections for ν_μ–e scattering [11], and it may be possible to derive a stronger bound on the basis of the mean free path of muon neutrinos in matter.

These constraints apply to familiar Minimal Standard Model (MSM) particles, and would not necessarily restrict the possibilities for exotic species. A number of searches for fractional charge in candidates not limited to the MSM have been carried out. The list below, while not exhaustive, gives a feel for the variety of approaches that have been employed, and their levels of charge sensitivity. (For a discussion of the best current constraints on mQ charge, see Section2.9.)

- Searches for fractionally charged products of Z^0 decays [12] (via ionization energy loss) report charge sensitivities down to $\sim 2e/3$;
- Searches for fractional charge in $\overline{\mathrm{p}}$-p collision products [13] (based on time of flight and calorimeter data) reach $2e/3$ sensitivity;
- A search for bound states between a fractionally charged atom and an electron (or hole) within solid silicon, using infrared photoionization and field ionization [14], also provides $2e/3$ sensitivity;
- Searches for low-charge signatures among particles traversing neutrino detectors (both water Cerenkov [15] and liquid scintillator [16]) have sensitivity down to $e/3$;
- A search for fractional charge on tiny liquid drops in a Millikan-type experiment [17] reaches sensitivity to $0.2\,e$;
- Searches for fractional charge on small (< 1 mm) pieces of solid material, including Nb, W, WC, steel and various meteorites, magnetically levitated and subjected to an alternating electric field [18], have maximum sensitivity of $0.1\,e$;
- Searches for fractionally charged fragments from heavy-ion collisions [19] (based on ionization energy loss) report sensitivity to $0.06\,e$;
- Re-analysis of data from a beam dump experiment carried out at SLAC [20] gives the highest charge sensitivity, reaching $\sim 10^{-3}\,e$ (see Fig. 2.4).

(Note that searches relying on recoil nuclei for detection of exotic particles are poorly suited for mQ detection, since mQs cannot be assumed to participate in the strong or weak interactions.) It is certainly suggestive of an underlying principle at work when such a varied set of experimental techniques fails to produce any evidence of non-quantization of charge. On the other hand, the possibility of fractional charge small enough to be overlooked in such experiments ought not be entirely discounted.

2.4 Charge Quantization in the Minimal Standard Model

In the review by Foot *et al.,* [4] careful consideration is given to the question of whether the MSM produces charge quantization as a natural consequence. The authors' conclusions are as follows.

2.4.1 The One-Generation MSM

In the MSM with only one generation of quarks and leptons, there are two constraints on the possible weak hypercharge values of the particles. One comes from the classical structure of the Lagrangian (in particular, from the requirement that $\mathcal{L}$ be U(1)-symmetric), and the other follows if we insist upon cancellation of the gauge anomalies (which is necessary to ensure the renormalizability of the theory). Together these two constraints are sufficient to fix the hypercharges of all the particles and ensure that they assume their standard values. The electric charge Q is related to the hypercharge Y (without loss of generality) via

$$Q = I_3 + Y/2 \tag{2.1}$$

where I_3 is the weak isospin, and thus the electric charges of the particles have their standard, quantized values in the one-generation MSM.

2.4.2 The Three-Generation MSM

In the three-generation MSM the picture is a bit more complicated. There is no *a priori* reason to assume that the generations are perfect copies of one another, and without this assumption we are free to consider the possibility that the hypercharge values differ between generations.* In this case the two constraints mentioned above are insufficient to uniquely determine the hypercharges. This is because the Lagrangian of the three-generation MSM contains a two-parameter family of unbroken global U(1) symmetries (independent of standard hypercharge) that are free of gauge anomalies. These symmetries are given by [4]

$$L' = \alpha L_{\rm e} + \beta L_\mu + (-\alpha^3 - \beta^3)^{\frac{1}{3}} L_\tau + \frac{1}{3}\left[-\alpha - \beta - (-\alpha^3 - \beta^3)^{\frac{1}{3}}\right] B, \tag{2.2}$$

where $L_{\rm e}, L_\mu, L_\tau$ are the family lepton numbers, B is the baryon number, and α and β are free parameters. The *actual* hypercharge Y may be any linear combination of standard hypercharge $Y_{\rm SM}$, and L'.

With faith in quantum gravity, one may insist on a further restriction: the cancellation of the mixed gauge-gravitational anomaly. This reduces the possibilities for L' to three discrete sets, each dependent on a single free parameter δ [4]:

$$L' = \begin{cases} \delta\,(L_{\rm e} - L_\mu) & \text{or} \\ \delta\,(L_{\rm e} - L_\tau) & \text{or} \\ \delta\,(L_\mu - L_\tau)\,. \end{cases} \tag{2.3}$$

But clearly this is not sufficient for a unique determination of Y. It therefore follows that the three-generation MSM does not enforce charge quantization.

Some important points to note here are the following. For each of the three possible L' sets, the neutrinos in two out of the three generations will have nonzero electric charge. The first two sets lead to atoms (including hydrogen) having nonzero charge. Experimental investigations of the neutrality of matter impose an upper limit on δ in this case: $\delta < 10^{-21}$ [4]. The last set ($L' = \delta(L_\mu - L_\tau)$) leaves first-generation particles with their standard charges, but implies a nonstandard charge

*Several authors [21, 22, 23, 24] have investigated charge quantization under the assumption that the generations are identical, from which they conclude that charge is quantized in the three-generation MSM.

for the muon and tau, and nonzero charges for ν_μ and ν_τ. Agreement between the theoretical and measured cross sections for ν_μ–e scattering (which would include a contribution from photon exchange if ν_μ had nonzero charge) constrains δ to be less than 10^{-9} [4]. Stricter but less certain bounds can be obtained from cosmology and astrophysics: charged relic neutrinos would impart a thermal electric mass to the photon, leading to an effective long-distance violation of Gauss's law, for which the experimental evidence implies $|\delta| < 10^{-12}$, while the contribution of charged ν_μ and ν_τ to the cooling rate of red giants implies $|\delta| < 10^{-14}$ [4].

2.4.3 Some Simple Extensions of the MSM

The methods used above to investigate charge quantization in the MSM can be summarized by the following general result [4]: Lagrangians with anomaly-free global U(1) symmetries that are independent of standard hypercharge Y_{SM} do not enforce charge quantization. Applying this result to some simple MSM extensions, Foot *et al.* [4] conclude the following:

- In the MSM with only one generation, plus a massless right-handed neutrino, charge is not quantized. ($B - L$, where L is lepton number, is anomaly free.)
- In the MSM with only one generation, plus a right-handed Majorana neutrino, charge is quantized. (The Majorana mass term breaks the $(B - L)$ symmetry.)
- In the three-generation MSM with Dirac neutrinos, charge is not quantized. ($B - L$ is anomaly free.)
- In the three-generation MSM with three right-handed Majorana neutrinos, charge is quantized. (No global U(1) symmetries other than Y_{SM} are unbroken.)
- In the three-generation MSM with exactly one right-handed neutrino (with or without Majorana mass), charge is quantized. (No anomaly-free global U(1)'s other than Y_{SM} are unbroken.)

- In the three-generation MSM with an extra Higgs doublet, charge is quantized. (No anomaly-free global U(1)'s other than Y_{SM} are unbroken.)

2.5 Magnetic Monopoles, GUTs and Charge Quantization

It is known that a number of scenarios for new physics have quantization of electric charge as a natural consequence. Among these, grand unification and magnetic monopoles are rather appealing possibilities. Magnetic monopoles are the particles that would complete the symmetry between the electric and magnetic components of Maxwell's equations. Dirac has shown that the existence of monopoles (even a vanishingly small number) would impose a constraint on the possible values of electric and magnetic charge [25]:

$$qg = \frac{n\hbar c}{2}, \tag{2.4}$$

where q is electric charge, g is magnetic charge, and n is an integer. The existence of particles with nonzero g leads immediately to quantization of both types of charge. As yet no firm experimental evidence for monopoles has been found.

The aim of grand unification is to derive a single framework in which to understand the strong and electroweak interactions. By definition, a grand unified theory (GUT) is a Yang-Mills theory whose gauge group G contains the Standard Model gauge group $\mathrm{SU(3)_c}\times\mathrm{SU(2)_L}\times\mathrm{U(1)_Y}$ and has only a single gauge coupling constant [26]. (Symmetry breaking reduces G to the Standard Model group and breaks the degeneracy of the gauge coupling strengths.) For G (a non-Abelian Lie group) to have only a single coupling constant, it must be simple (or semi-simple[†]). In a simple non-Abelian Lie group, the eigenvalues of a generator are integer multiples of the group's smallest eigenvalue. Since the photon is a gauge boson of the GUT group

[†]G can be of the form $H \times H$, where H is a simple group, if G includes a discrete symmetry ensuring the equality of bare coupling constants between the two factors.

G, the electric charge operator Q is a generator of G, and thus the eigenvalues of Q (the electric charges of the particles) are quantized. An alternate derivation of this result is given in an elegant proof by Georgi and Glashow [27]. The possibility of a GUT wherein the charge quantum is smaller than the experimental limit $10^{-21}\,e$ has been considered, but models of this type are unlikely to be realistic [28]. (It should be noted that GUTs and monopoles are not entirely independent, since symmetry breaking from the GUT group to the Standard Model generally gives rise to stable 't Hooft–Polyakov magnetic monopoles [29].)

2.6 Multiple U(1)s and Apparent Dequantization

In models containing more than one U(1) factor, there exists the possibility of producing apparent fractional charge without ever violating charge quantization. Such scenarios are interesting since they provide a means of compatibility between grand unification (or monopoles) and fractionally charged particles. Suppose the low-energy universe were described by a gauge group containing two U(1)s ($\cdots\times \mathrm{U}(1)^{\mathrm{A}}_{\mathrm{em}}\times \mathrm{U}(1)^{\mathrm{B}}_{\mathrm{em}}$), each with its own photon and its own electric charge. The Lagrangian would contain kinetic terms from the U(1)s that are given, in the most general case, by [30]

$$-L^{\mathrm{kin}}_{\mathrm{U}(1)} = \frac{1}{4}F^{\mu\nu}_{\mathrm{A}}F_{\mathrm{A}\,\mu\nu} + \frac{1}{4}F^{\mu\nu}_{\mathrm{B}}F_{\mathrm{B}\,\mu\nu} + \frac{\varepsilon}{2}F^{\mu\nu}_{\mathrm{A}}F_{\mathrm{B}\,\mu\nu}, \tag{2.5}$$

where ε is a free parameter. The last term represents a mixing between the two types of photon. At tree level, such mixing is disallowed within the framework of a GUT. However, an effective mixing of this form can be induced by radiative corrections, as will be described below. One of the physical manifestations of the mixing is a nonzero coupling between the charged fermions of $\mathrm{U}(1)_{\mathrm{B}}$ and the photon of $\mathrm{U}(1)_{\mathrm{A}}$, amounting to an apparent electric charge $\widetilde{q}$ of type A for the B-type fermions. This mixing-induced charge has magnitude [30] $\widetilde{q} = \varepsilon\, q_{\mathrm{B}}$, where q_{B} is the B-type charge of the fermion. In general, $\widetilde{q}$ is not commensurate with the charges of the fermions of $\mathrm{U}(1)_{\mathrm{A}}$.

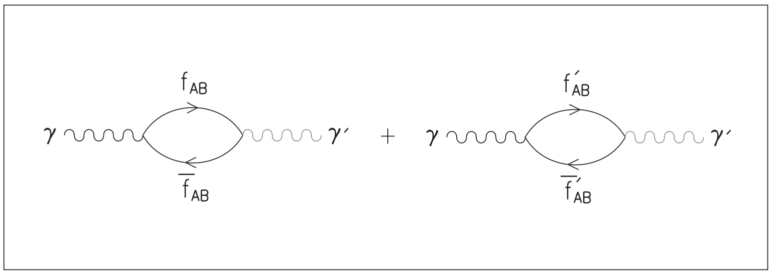

Figure 2.3: Holdom's proposed mechanism for mixing between normal and hidden-sector photons.

A means of obtaining photon kinetic mixing at loop level, due to Holdom [5, 6], is as follows. Suppose there exist fermions carrying both A and B type charge. If there were two such fermions, f_{AB} and f'_{AB}, whose charges were (q_{A}, q_{B}) and (q_{A}, $-q_{\mathrm{B}}$), respectively, then the vacuum polarization diagram (Figure 2.3) mixing the two types of photon would have nonzero magnitude, provided the masses of f_{AB} and f'_{AB} were different. This gives rise to an effective kinetic mixing $\frac{\varepsilon}{2} F_{\mathrm{A}}^{\mu\nu} F_{\mathrm{B}\,\mu\nu}$ with ε given by [5]

$$\varepsilon = \frac{q_{\mathrm{A}} q_{\mathrm{B}}}{6\pi^2} \ln\left(\frac{M'_{\mathrm{AB}}}{M_{\mathrm{AB}}}\right), \tag{2.6}$$

where M_{AB}, M'_{AB} are the masses of f_{AB} and f'_{AB}, respectively. So long as M_{AB} and M'_{AB} are larger than the masses of the known fermions, there are no restrictions on their values. They could be as large as the unification scale, making f_{AB} and f'_{AB} potentially very difficult to detect.

If M_{AB}, M'_{AB} and the difference between them were all of the same order of magnitude, and if the coupling constants of the two U(1)s were not very different, the magnitude of ε would be roughly 10^{-3} [6]. This raises the interesting possibility that a search for fractional charge of order $10^{-3}\,e$ could uncover evidence of fermions dwelling within a second U(1).

2.7 Brief Survey of Hidden-Sector Models

Theories involving a so-called hidden sector represent a class of models that can accommodate small fractional charge via the mechanisms discussed above. "Hidden sector" refers to any set of particles whose interactions with the known particles have strengths far smaller than the usual couplings (with the exception of gravitation, which is expected to be of normal strength). The literature contains explorations of a number of hidden-sector models. Motivation for the development of such models has come from superstring theory (which often predicts the existence of fractionally charged particles [31]), particularly theories involving an $E_8 \times E_8$ gauge group [32, 33], in which one E_8 reduces to the gauge group of the Standard Model while the other becomes a hidden sector after symmetry breaking; from a desire to restore an appealing symmetry (usually CP) to the Standard Model Lagrangian [34] (requiring a doubling of the particle content); and, recently, from attempts to explain the neutrino anomalies, together with the LSND result, via mixing between normal and hidden-sector neutrinos [35]. In the literature, hidden sectors derived from superstring ideas are often referred to as "shadow" sectors, while those developed in hopes of restoring CP or other symmetries to the Lagrangian of the Standard Model generally go by the name "mirror."‡

One set of hidden-sector models is based upon a CP-symmetric extension of the MSM Lagrangian [8]. For every known left-handed fermion there is a right-handed partner (and vice-versa) of the same mass. The normal and mirror sectors have identical coupling constants, and there is a discrete symmetry, A, interchanging the two sectors such that the Lagrangian is symmetric under CP·A. The authors of Ref. [8] have determined that in order for such models to be compatible with experimental data, the normal and mirror sectors cannot be bridged by the strong, weak or electromagnetic interactions. They each must have their own identical set of gauge bosons.

‡The term "mirror" is also sometimes used in reference to exotic particles that couple to normal matter via the strong interaction [36], and which therefore do not represent a hidden sector.

Such models can produce apparent fractional charge via tree-level kinetic mixing between the photons, or, if we wish them compatible with grand unification (as, *e.g.,* $SU(5)_{normal} \times SU(5)_{mirror}$), via Holdom's effective kinetic mixing.

These models tend to be incompatible with Big Bang Nucleosynthesis (BBN), however, since they involve twice the usual number of relativistic particle species in the early universe, predicting an expansion rate that leads to an abundance of primordial ^{4}He in excess of the amount observed experimentally [37, 38]. The conflict could be avoided if the weak coupling constant were 10% larger during nucleosynthesis than it is at present [39], or if the mirror sector were at a lower temperature (*i.e.* lower energy density) than the normal sector [37, 38]. In the latter case, the asymmetry may be attributed to unknown physics of the Big Bang (the universe created more normal than mirror particles), or, within the context of inflation, to different post-inflationary reheating temperatures in the two sectors [37, 40]. Coupling between normal and mirror particles would tend to bring the two sectors back into thermal equilibrium. In the case of an ε–size electromagnetic coupling, which would populate the mirror sector via $e^+e^- \rightarrow e^+_{mirror}\, e^-_{mirror}$, insisting that the time necessary for the sectors to equilibrate be greater than the age of the universe (~ 1 sec) at nucleosynthesis leads to the bound [37] $\varepsilon < 3 \times 10^{-8}$. A non-cosmologically based bound of $\varepsilon < 4 \times 10^{-7}$ has been derived on the basis of the production and decay rates of positronium [41], but this result is not without some controversy [39]. Additionally, it has been argued that realistic grand unification schemes result in a *lower* bound on ε, $\varepsilon > 10^{-6}$, in the context of this type of mirror model [41].

Two variants of the CP$\cdot$A symmetric models discussed above have been advanced recently as a possible means of providing a simultaneous explanation for the solar neutrino anomaly, the atmospheric neutrino anomaly, and the result from LSND. (These models allow for oscillation between normal and mirror neutrinos, in addition to oscillation between families in the normal sector.) The first is a model in which parity (rather than CP), together with a sector-interchanging operation A, form an unbroken symmetry of the Lagrangian [42]. (As in the previous models, the particle content, masses and coupling constants are identical in the two sectors.) Any apparent fractional charge due to tree or loop-level kinetic mixing would have to be extremely small in order to leave this model compatible with both BBN and the neutrino data. The second proposal involves a mirror sector in which the electroweak symmetry is broken at a different ($\sim$ 30 times higher) scale than in the normal sector [43]. The masses of charged fermions and gauge bosons will be 30 times larger in the mirror sector, while neutrino masses (assumed nonzero) will be 30^2 times larger. Unlike the previous models, in which apparent fractional charge, if present, would be carried by particles having the same masses as the electron, muon and tau, the lightest possible fractional-charge carrier in this model would have $M \cong 15$ MeV/c^2.

In addition to the models explored thus far, one could imagine any number of possible hidden sectors in which the coupling constants, masses and/or particle spectrum were different from those in the normal sector. Compatibility with BBN, grand unification or any other desirable framework would depend upon the details of the individual model, and manifestation of apparent fractional charge would be a possibility in any model having an electromagnetism U(1) in its hidden sector.

2.8 Non-conservation of Electric Charge

A very speculative set of models usually leading to dequantization of electric charge is that in which the electromagnetic gauge symmetry is broken (*i.e.* charge is not conserved). For such models to be local and causal, the photon must have nonzero mass. Models involving hard symmetry breaking and predicting nonzero (but tiny) charge for atoms, neutrons and neutrinos have been discussed in the literature [44], but suffer from the "hyperphoton catastrophe," [45] in which the predicted rate of the process $e^- \to \nu + n\gamma_L$, where γ_L is a longitudinally polarized photon, is ridiculously large and diverges when summed over n. Spontaneous, as opposed to explicit, breaking of electromagnetism allows one to avoid this difficulty. Ignatiev *et al.* [46] have argued that within the context of renormalizable gauge theories, any model in which charge is not exactly conserved must include a light scalar particle with 'pseudo-electric' charge εe satisfying $\varepsilon \lesssim 10^{-2}$, along with additional particles having charge $q = (n \pm \varepsilon)e$. (This is necessary to ensure compatibility with the experimental limit on the mass of the photon, $m_\gamma < 6 \times 10^{-22}$ MeV/c^2 [47], and with the measured value of the muon's anomalous magnetic moment.) In these models, charge non-conserving processes with $\Delta q = \varepsilon e$ are allowed, while the details of the model may be tailored to either allow or disallow processes with $\Delta q \geq e$. (Permitting $\Delta q \geq e$, *e.g.,* $\mathrm{e}^- \to \nu\gamma$ or $\mathrm{e}^- \leftrightarrow \mathrm{e}^+$, leads to a number of nonphysical consequences. For a discussion, see Ref. [48].)

A number of authors have investigated models in which a fractionally charged Higgs (with $q \ll e$) breaks the electromagnetic symmetry. In one model [45], the Higgs sector consists of the usual doublet, plus a minicharged singlet h, which is the only particle to carry non-quantized charge. Among the normal particles, only the photon has a direct coupling with h. The photon mass is proportional to $\varepsilon e v$, where εe is the charge of h and v is its VEV, and must satisfy $\varepsilon m_\mathrm{h} \lesssim 10^{-20}$ in order not to conflict with the experimental limit $m_\gamma < 6 \times 10^{-22}$ MeV/c^2 [47]. Consideration of the cooling rate of red giants leads to the bound $\varepsilon \lesssim 10^{-7}$ [45]. Processes with $\Delta q \geq e$ are disallowed.

A second model involves two Higgs doublets and a singlet [49, 50]. The charges of the fermions each differ from their normal values by a term of order ε, so neutrinos, neutrons and atoms will be slightly fractionally charged. The Higgs singlet has charge $q \sim \varepsilon^3$ and doesn't couple to fermions, while the doublets have hypercharges $Y = 1$ and $Y = 1 - \mathcal{O}(\varepsilon^3)$, and couple to quarks and leptons, respectively. The scale of charge non-conservation (the amount by which the charges of right and left-handed fermions differ) in this model is ε^3. The photon mass is also proportional to ε^3, and thus the bound on ε from the experimental limit on m_γ is far weaker than in the previous model. Investigations of this model have been made both with [49] and without [50] the assumption that hypercharge values are the same across generations.

One further model, also predicting ε–charged neutrinos, neutrons and atoms, has been explored [23]. It assumes that generations have identical quantum numbers, and has a Higgs sector consisting of two doublets. The first, with hypercharge $Y = 1 - \varepsilon$, gives mass to the fermions, while the second, with $Y = 1$, does not couple to fermions. Photons have mass proportional to ε, left and right-handed fermion charges differ by ε, and the physical Higgs is ε–charged. The experimental limit on the anti-electron neutrino charge from SN 1987A [51], $|q_{\overline{\nu}_e}| < 10^{-17}\,e$, places an upper limit on ε of 10^{-17}.

2.9 Experimental Bounds on Fractional Charge

Several sections of the charge-mass parameter space for fractionally charged particles can be excluded based upon the available experimental evidence. Some of these bounds rely on relatively few assumptions, while others are dependent on the accuracy of astrophysical and cosmological models. A summary of the presently excluded regions (not including the results of this experiment) will be given in the discussion that follows.

2.9.1 Bounds from Direct Measurements

Five experimental measurements serve to rule out a significant portion of the charge-mass parameter space, particularly in the region of high ($q \cong e$) charge. The ASP (Anomalous Single Photon) search at SLAC sought to measure $\mathrm{e^+e^-} \to \gamma\,\mathrm{X}$, where X is any weakly interacting particle. Its results rule out particles with charge $q > 0.08\,e$ for masses $M \lesssim 10$ GeV/c^2 [20]. Analysis of the data from a proton beam dump experiment, E613, at Fermilab rules out charges between 10^{-1} and $10^{-2}\,e$ for $M < 200$ MeV/c^2 [52]. An electron beam dump experiment at SLAC, which sought to detect neutrino-like particles, has been re-analyzed in the context of trident production ($\mathrm{e^-\,N \to e^-\,N\,mQ^+\,mQ^-}$) and detection ($\mathrm{mQ\,N \to mQ\,N\,e^+\,e^-}$) of mQs, resulting in the exclusion of $q > 3 \times 10^{-4}\,e$ for $M < 200$ keV/c^2, and $q > 3 \times 10^{-2}\,e$

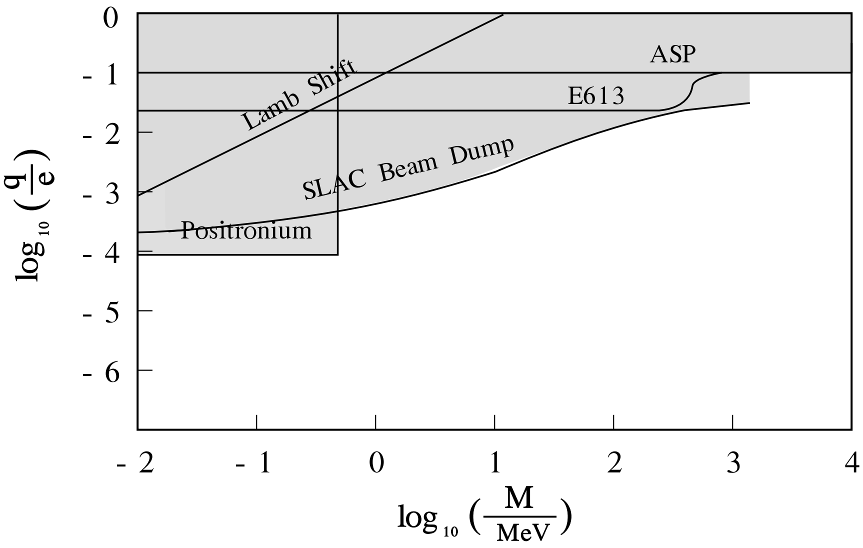

Figure 2.4: Regions of charge-mass parameter space excluded by direct measurements.

for masses up to 1 GeV/c^2 [20]. In addition to these accelerator-based measurements, the results of a search for decays of orthopositronium into "invisible" particles and the precise agreement between the calculated and measured values for the Lamb shift (the energy level splitting between the $2P_{\frac{1}{2}}$ and 2S states of the hydrogen atom, which arises from radiative corrections) can be used to constrain q and M. The orthopositronium data establish an upper bound on the branching ratio to invisible (including low-ionizing) particles of 2.8×10^{-6}, which rules out the existence of mQs with $q > 8.6 \times 10^{-5}\, e$ for $M < 500\,\mathrm{keV}/c^2$[53]. (In models with a hidden sector containing electrons and positrons of the same mass as those in the normal sector, this result also constrains the strength, ε, of mixing between normal and hidden-sector photons to be less than 1.5×10^{-8}[53].) The lowest-order effect of mQs on the Lamb shift comes from their contribution to the photon vacuum polarization diagram. Requiring that this not spoil agreement between calculation and experiment excludes charges satisfying $q/e > (1/9)M$, where M is in MeV/c^2 [55, 20]. (This bound applies for $M \gtrsim 3$keV.) The excluded contours corresponding to these five results are shown in Figure 2.4.

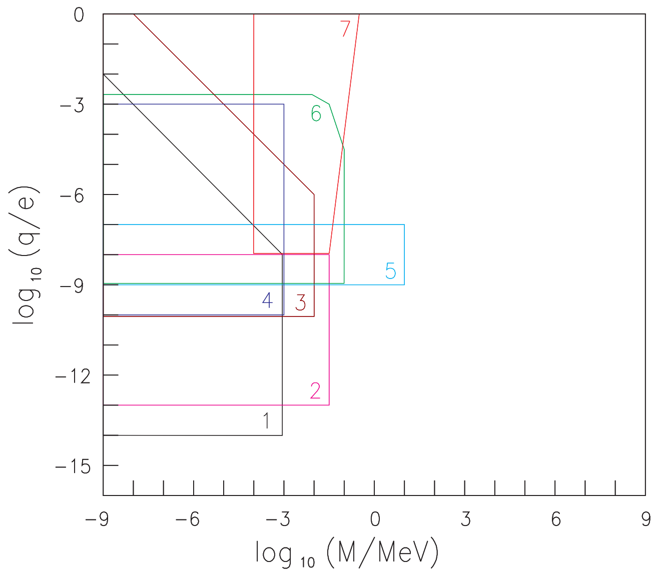

Figure 2.5: Regions of charge-mass parameter space excluded by astrophysical arguments. 1. Plasmon decay and heat conduction in red giants. 2. Cooling rate of white dwarfs. 3. Cooling rate of white dwarfs. 4. Energy loss from the sun. 5. Energy loss from SN 1987A. 6. Heat transport in red giants. 7. Hidden-sector photon emission from red giants.

2.9.2 Bounds from Astrophysics

For certain ranges of q and M, mQs are expected to have a sizeable effect on the dynamics of the sun, red giants, white dwarfs and supernovas. Several bounds have been derived on the basis of these effects. Though not as solid as the bounds from laboratory measurements, these may be considered valid insofar as we have confidence in the solar and astrophysical processes on which they depend. Unless otherwise indicated, the discussion that follows assumes there is no hidden-sector photon into which $\mathrm{mQ}^+\mathrm{mQ}^-$ pairs can annihilate. (Bounds derived from hidden-sector photons will be discussed at the end of this section). The results are shown in Figure 2.5.

For mQs with $M \lesssim 1\ \mathrm{MeV}/c^2$ (the cutoff below which $\mathrm{mQ}^+\mathrm{mQ}^- \rightarrow \mathrm{e}^+\mathrm{e}^-$ is kinematically forbidden) and $q \lesssim 10^{-3}\,e$, the rate of mQ annihilation within a star has been shown to be negligible compared to the rate of mQ production [54]. Depending on their parameters, mQs can either be trapped within the star, or they can escape, carrying away energy from the star as they go. Of the bounds derived from astrophysics, the most reliable is that based upon energy loss from the sun. If the power emitted in the form of escaping mQs is not to exceed the power radiated as photons (assuming mQs do not become trapped), an estimate of the rate of production of mQs within the sun leads to the exclusion of the charge range $10^{-10}\,e < q < 10^{-3}\,e$ for masses $M < 1$ keV/c [54].

Photons travelling within a plasma ("plasmons") acquire an effective mass and can decay into pairs of charged particles. Plasmon decay is the principal means of mQ production within a star. For a red giant (where the plasmon mass is $m_\gamma \cong 2$ keV/c^2 [20]), mQs with $M \lesssim 1$ keV/c^2 contribute to the energy loss of the star. Requiring that the rate of energy loss to mQs not exceed the rate of nuclear energy production excludes values of q greater than $10^{-14}\,e$ [20]. The excluded region extends as far as $q = 10^{-8}\,e$ (for $M = 1$ keV/c^2) or $10^{-5}\,e$ (for $M = 1$ eV/c^2), above which the mQs become trapped in the star and no longer contribute to the energy loss. Trapped mQs do, however, contribute to the efficiency of heat conduction within the red giant, and the requirement that their contribution be less than that from convective heat transport extends the excluded region to $q = 2 \times 10^{-3}\,e$ [55].

Plasmon decay to mQ pairs will contribute to the rate of cooling of white dwarfs. For the present theory of white dwarf cooling to remain consistent with the observed luminosity distribution, mQ charges must be excluded over the range $10^{-13}\,e < q < 10^{-2}\,e$ (for $M < 1$ eV/c^2), $10^{-13}\,e < q < 10^{-6}\,e$ (for 1 eV/$c^2 < M < 10$ keV/c^2), and $10^{-13}\,e < q < 10^{-8}\,e$ (for 10 keV/$c^2 < M < 25$ keV/c^2) [20, 55].

Observation of neutrinos from supernova SN 1987A allows for the exclusion of another piece of charge-mass parameter space. Production of mQs would divert energy from neutrino generation in a supernova. The experimental observation of neutrinos from SN 1987A provides an upper bound to the amount of energy that could have been lost to mQs. Calculation of the expected rate of emission of mQs from the core of the supernova allows one to exclude the charge range $10^{-9}\,e < q < 10^{-7}\,e$ for

$M < 10\,\mathrm{MeV}/c^2$ [56].

In a universe with hidden-sector photons (γ') that couple to mQs with a strength α' close to α, bounds from the energy loss of stars are more stringent than those calculated in the absence of a hidden-sector photon. Within the helium core of a star, a population of mQs in thermal equilibrium with the normal plasma will be established via the process $\mathrm{e^-N} \rightarrow \mathrm{e^-N\,mQ^+mQ^-}$, and hidden-sector photons will be generated through Compton scattering ($\mathrm{mQ}\,\gamma \rightarrow \mathrm{mQ}\,\gamma'$). Radiation of γ's can contribute significantly to the cooling rate of the star. If the mQ mass satisfies $M > 100\,\mathrm{eV}/c^2$, the mean free path of γ's in the star's outer region will be greater than that of normal photons, so the γ' photosphere will begin at a smaller radius, and thus the star will emit γ's more readily than ordinary photons [57]. Requiring that the rate of γ' production via Compton scattering in the helium core be smaller than the ratio of normal-photon luminosity to surface temperature leads to the bound [57] $M \lesssim 0.4 + 0.02\ln(q/e)$ MeV/c^2, from consideration of red giants. A similar argument applied to the sun [57] yields the less stringent but more reliable bound $M \lesssim 40 + 2\ln(q/e)\,\mathrm{keV}/c^2$.

2.9.3 Bounds from Cosmology

With faith in the Standard Cosmological Model, we may derive additional bounds on the mQ parameters. We can insist that the relic density of mQs be insufficient to overclose the universe. We can require that the presence of relic mQs not result in too large an effective mass for the photon. And we can require that the effect of mQs on the predictions of Big Bang Nucleosynthesis be small enough to preserve the agreement between the calculated and measured primordial abundances of the light elements. The regions thereby excluded are shown in Figure 2.6.

In order for the relic density of mQs, ρ_{mQ}, not to exceed the critical density ρ_c that would make the universe flat ($\rho_c = 1.88 \times 10^{-29}\,h^2$ g/cm^3 [58], where h is 1/100 of the Hubble constant in $\mathrm{km\,sec^{-1}\,Mpc^{-1}}$), either the mQ mass must be smaller

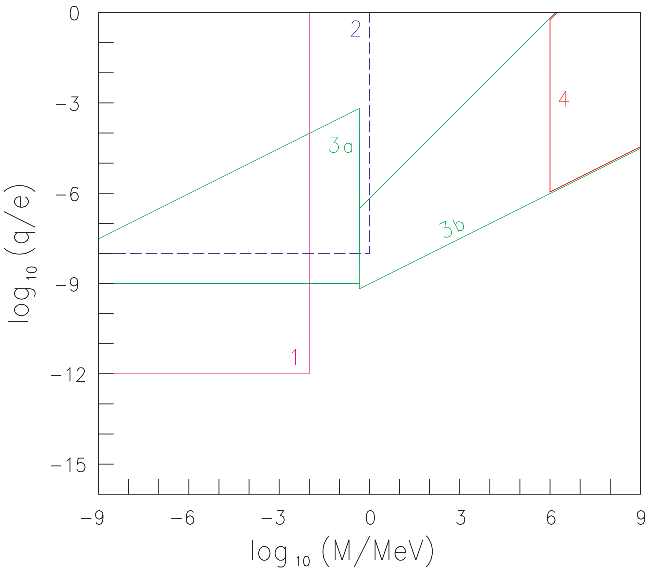

Figure 2.6: Regions of charge-mass parameter space excluded by cosmological arguments. 1. Thermal electric mass of photon. 2. Big Bang Nucleosynthesis. 3. $\Omega < 1$. 4. This area becomes allowed in models with a hidden-sector photon.

than about 100 eV/c^2, the mQ population must have been greatly reduced via annihilation, or the mQ and normal-matter sectors must have been out of thermal equilibrium when the normal-sector temperature T was greater than M. Assuming for the moment the absence of a hidden-sector photon, mQs will annihilate principally via $\mathrm{mQ^+mQ^-} \rightarrow \mathrm{e^+e^-}$ provided $M > m_\mathrm{e}$. In this case, the requirement that ρ_mQ/ρ_c ($\equiv \Omega$) be less than 1 leads to the bound $M < 2 \times 10^3\,(q/e)$ GeV/c^2 [20], assuming the sectors are in thermal equilibrium (which will be the case so long as $M < 10^{15}\,(q/e)^2$ GeV/c^2 [20]). For $M < m_\mathrm{e}$, the dominant annihilation process is $\mathrm{mQ^+mQ^-} \rightarrow \gamma\gamma$, and the corresponding bound is $M < 10^3\,(q/e)^2$ GeV/c^2 [54]. This again presumes thermal equilibrium, which may cease to hold for $q \lesssim 10^{-9}\,e$ [54]. If there exists a hidden-sector photon γ' allowing the process $\mathrm{mQ^+mQ^-} \rightarrow \gamma'\gamma'$, the bounds that apply under thermal equilibrium will be relaxed to $M < 10^5\,\alpha'$ GeV/c^2, where α' is the electromagnetic coupling constant in the hidden sector [20]. (For example, if $\alpha' < 1/10$, we have $M < 10$ TeV/c^2.)

The presence of relic light mQs spread throughout the universe amounts to a thermal bath with $T \cong 2^{\circ}$K [11]. It also represents a background plasma that all particles (in particular, photons) must traverse. Photons will acquire a thermal electric mass m_γ^{el} from interactions with the mQs, which will manifest itself experimentally as a long-range violation of Gauss's law. Comparison between the lowest-order contribution to m_γ^{el} (from the 1-loop vacuum polarization diagram with internal propagators taken at finite temperature) and experimental tests of Gauss's law ($m_\gamma^{\mathrm{el}} < 10^{-25}$ GeV/c^2) excludes mQs with $q > 10^{-12}\, e$ for $M < 10\,\mathrm{keV}/c^2$ [11].

Big Bang Nucleosynthesis (BBN), the widely accepted model describing conditions in the early universe ($t \cong 0.01\mathrm{sec} - 100\mathrm{sec}$) before and during the coalescence of protons and neutrons into nuclei, can be used to exclude a large portion of charge-mass parameter space for light mQs in models with a hidden-sector photon (and those without a hidden-sector photon, assuming the tau neutrino is not too heavy). BBN makes predictions for the primordial abundances of the light elements D, ^{3}He, ^{4}He and ^{7}Li based upon input parameters including the number of relativistic particle species present when the temperature of the universe was above ~ 1 MeV/k_{B}. Within the MSM, these predictions are compatible with the observed abundances. The presence of additional relativistic particle species increases the predicted abundance of ^{4}He, potentially disturbing agreement between the BBN prediction and experiment. If we insist on maintaining compatibility, we can derive restrictions on the parameters of new light particles.

A good review of BBN can be found in Yang *et al.,* [59] and, more recently, in Sarkar [60]. During the BBN era, the universe is filled with a relativistic gas of e$^+$e$^-$ pairs, light neutrinos and photons, together with trace quantities of nucleons (the nucleon to photon ratio, η, is between 10^{-10} and 10^{-9}). The universe's rate of expansion is given by [38]

$$\frac{\dot{R}}{R} = \left(\frac{8\pi\rho G_{\mathrm{N}}}{3}\right)^{\frac{1}{2}}, \tag{2.7}$$

and its rate of cooling is described by the relation [59]

$$t_{\mathrm{sec}} = 2.42\, g_*^{-1/2}\, T_{\mathrm{MeV}}^{-2} \tag{2.8}$$

where R is the cosmic scale factor, G_{N} is Newton's constant, ρ is the energy density, t_{sec} is time in seconds, T_{MeV} is the temperature in MeV, and g_* counts the number of relativistic degrees of freedom. g_* is computed as follows: [59]

$$g_* = \sum_{\mathrm{B}} g_{\mathrm{B}} \left(T_{\mathrm{B}}/T_\gamma\right)^4 + \frac{7}{8} \sum_{\mathrm{F}} g_{\mathrm{F}} \left(T_{\mathrm{F}}/T_\gamma\right)^4 , \tag{2.9}$$

where g_{B} (g_{F}) is the number of helicity states of the boson (fermion), T_{B} (T_{F}) is the temperature ($\leq T_\gamma$) of the species, and the sum runs over particles and antiparticles with $M \lesssim 1\,\mathrm{MeV}/c^2$. (In the MSM, for example, $g_* = 2 + (7/8)(4+6) = 10.75$ from the photon, $\mathrm{e}^+\mathrm{e}^-$, and $\nu_i\,\overline{\nu}_i$, assuming all neutrinos are light.) The energy density ρ is proportional to g_* via [38]

$$\rho = \frac{\pi^2 g_* \left(k_{\mathrm{B}} T_\gamma\right)^4}{30\,\hbar^3 c^3}, \tag{2.10}$$

and thus the rate of expansion depends strongly on the number of light species present (that are not significantly colder than the photons) during BBN.

For $T > 0.4\,\mathrm{MeV}/k_{\mathrm{B}}$, the weak reactions

$$\mathrm{p} + \mathrm{e}^- \leftrightarrow \mathrm{n} + \nu_{\mathrm{e}}, \quad \mathrm{n} + \mathrm{e}^+ \leftrightarrow \mathrm{p} + \overline{\nu}_{\mathrm{e}}, \quad \mathrm{n} \leftrightarrow \mathrm{p} + \mathrm{e}^- + \overline{\nu}_{\mathrm{e}} \tag{2.11}$$

keep neutrons and protons in chemical equilibrium, and the neutron to proton ratio decreases rapidly according to [59]

$$\mathrm{n}/\mathrm{p} = \exp\left(-\Delta m/T\right). \tag{2.12}$$

where Δm is the neutron-proton mass difference. Below $T \lesssim 0.4\,\mathrm{MeV}/k_{\mathrm{B}}$, the weak reaction rates fall below the rate of expansion, and the n/p ratio becomes frozen, except for a slow decrease from beta decay ($\mathrm{n} \leftrightarrow \mathrm{p} + \mathrm{e}^- + \overline{\nu}_{\mathrm{e}}$). Formation of stable nuclei begins around $T = 0.1$ MeV/k_{B}. The amount of each light element produced subsequently depends on the neutron to proton ratio, the nucleon to photon ratio (η), and the rates of the various nuclear reactions which interconvert the different nuclei. The nuclear reactions are fairly well understood [61], while η is essentially an unknown parameter. The neutron to proton ratio depends strongly on the temperature at which the weak reactions freeze out, which in turn depends upon the expansion rate (and thus on the number of light species). (A greater expansion rate means the expansion will out-pace the weak reactions at a higher temperature, which then freezes n/p at a higher value.) Most of the available neutrons get bound into ^{4}He, and the ^{4}He abundance increases with an increase in the number of light species according to [38]

$$\Delta Y_{\mathrm{p}} \cong 0.19 \log_{10}\left(g_*/g_*^{\mathrm{MSM}}\right), \tag{2.13}$$

where Y_{p} is the mass fraction of ^{4}He.

The primordial ^{4}He mass fraction deduced from the best currently available data (as of 1999) has an uncertainty of a few percent, while for the other light elements, the uncertainties are a factor of two, at best. Bounds on η and g_* (which are correlated) have been derived on the basis of these data, the conservative conclusion being that g_* must fall within the range [60]

$$9 < g_* < 13.4. \tag{2.14}$$

(Often the number of degrees of freedom is expressed in terms of the number of equivalent light neutrino species $N_{\nu*}$, with $N_{\nu*}$ and g_* related by $N_{\nu*} = (4/7)(g_*-5.5)$. The bound above corresponds to $2 < N_{\nu*} < 4.5$.) There is a caveat to be considered in comparing the g_* of a particular model to the allowed range, however. Anything which might directly perturb the weak reaction rates (*e.g.,* particles which induce an asymmetry between the numbers of ν_{e} and $\overline{\nu}_{\mathrm{e}}$ [62]) will affect the production of the light elements. Decays or annihilations of a heavy Standard Model neutrino would also impact light element abundances. In such cases it is necessary to define an *effective* number of degrees of freedom g_{eff} (or number of equivalent neutrinos $N_{\nu\,\mathrm{eff}}$) based upon the model's prediction for the abundance of ^{4}He, and interpret the bounds in Eqn. 2.14 as applying to g_{eff}. (The number of effective degrees of freedom may be either larger or smaller than g_*.) Assuming that neutrinos cannot decay or annihilate, and that nothing in the model under consideration would affect the rate of the weak reactions (*i.e.,* assuming $g_{\text{eff}} = g_*$), the implications of Eqn. 2.14 for light mQs can be derived. Massless mQs are excluded by astrophysical considerations for $q > 10^{-12}\,e$ [63], so we will not discuss them. Massive mQs are Dirac particles and thus contribute 3.5 to g_*, assuming they are in thermal equilibrium with the photons, and $M \lesssim 1\,\text{MeV}/c^2$. Coupling between mQs and ordinary particles will keep them in thermal equilibrium if $q \gtrsim 10^{-8}\,e$ [56]. A hidden-sector photon ($\gamma\,'$) would contribute an additional 2 degrees of freedom. The contribution of the Standard Model particles is usually taken to be 10.75, but this assumes all neutrinos are light. The current (1998) upper bound on the mass of ν_τ is $18.2\,\text{MeV}/c^2$ [9], so it would be more conservative to take 9 degrees of freedom as the Standard Model contribution. We then have

$$g_* = \begin{cases} 12.5 & \text{for Standard Model plus Dirac mQ} \\ 14.5 & \text{for Standard Model plus Dirac mQ and } \gamma\,'. \end{cases} \tag{2.15}$$

With the g_* upper bound of 13.4, the former case is allowed, while the latter case is ruled out. (If $M_{\nu_\tau} \lesssim 1\,\text{MeV}/c^2$, both cases are ruled out.)

An idea not considered thus far is the possibility that a mQ could be one of the known particles. The best experimental bound on the charge of the tau neutrino (assuming that ν_τ does not oscillate into one of the other known species), is derived from the results of the SLAC beam dump experiment [20]. This bound is rather weak: $|q_{\nu_\tau}| < 3 \times 10^{-4}\,e$. A Dirac ν_τ with $M \lesssim 1\,\text{MeV}/c^2$ would contribute 1.75 degrees of freedom to the 10.75 of the MSM, for a total of 12.5. (A heavier ν_τ will not contribute to the relativistic energy density during BBN.) Therefore a millicharged tau neutrino is compatible with BBN.

2.10 Conclusions

Millicharged particles, characterized by their small cross section for interaction with matter, are not forbidden within the MSM. Numerous efforts toward the experimental detection of free fractional charge have thus far proven unsuccessful, suggesting that charge quantization may be enforced by some fundamental mechanism. Grand Unification and the existence of a Dirac monopole represent attractive possibilities for such a mechanism, but models have been proposed wherein apparent fractional charge can exist within such scenarios. Superstring theory and models involving imperfect conservation of charge generally predict fractionally charged particles. A number of direct measurements exclude particles with $M \lesssim 1\ \mathrm{GeV}/c^2$ and $10^{-2}\,e \lesssim q < e$. Additional regions of charge-mass parameter space can be ruled out on the basis of astrophysical and cosmological considerations. Among these is a large region ($q \gtrsim 10^{-8}\,e$, $M \lesssim 1\ \mathrm{MeV}/c^2$) excluded by BBN, given certain assumptions regarding the particle spectrum of the universe. Clearly the existence of millicharged particles has not been experimentally ruled out, nor has a definitive mechanism for the enforcement of (real and apparent) charge quantization been found. There remains good motivation for future experimental efforts toward discovery of free fractional charge.

Chapter 3

Production and Transport

3.1 Introduction

Assuming mQs have only electromagnetic interactions, possible sources of mQs at the Earth's surface include the following: relic mQs encountered as the Earth sweeps through its orbit[64, 65]; mQs generated when cosmic rays strike the atmosphere[64, 66]; and mQs produced in particle accelerators[64, 66]. Of these, the last has advantages with regard to mQ detection in that a beam of mQs could be generated. In the case of an accelerator beam directed towards a target, mQ production would be enhanced by electromagnetic showers generated within the target. The use of a high-current electron accelerator as the site of a mQ search was first proposed by Dobroliubov and Ignatiev[66].

SLAC, which directs a 29.5 GeV electron beam, with average current 3.6×10^{12} electrons/second, onto a tungsten target (in order to generate positrons), is among the suitable facilities, and is the site chosen for our experiment. SLAC has the added advantage that the beam is divided into bunches with very short ($\sim$ 10 picosecond) duration, allowing for a sizeable enhancement of signal-to-noise with appropriate timing of data collection. The SLAC beam does, however, produce an abundance of high-energy muons, which necessitates a large amount of shielding between the target and a mQ detector. MQs with mass (M_{mQ}) greater than that of the electron (m_{e}) will readily out-distance these muons. But for $M_{\mathrm{mQ}} \ll m_{\mathrm{e}}$, it is possible that the cross section for Bremsstrahlung and $\mathrm{e}^{+}\mathrm{e}^{-}$ pair production by mQs is sufficiently large that the mQs stop before the muons, and thus escape detection.

The first section of this chapter provides a discussion of mQ production at SLAC, including the means by which we estimate the mQ energy distribution, angular distribution and total yield. The second section describes mQ energy loss in the material between the source and our detector, and, given our experimental setup (described in chapter 4), presents the parameters for which mQs are likely to escape detection.

3.2 Production

The electromagnetic showers within SLAC's SLC positron-production target (PPT) were a favorable place for mQ production to occur. The positron-production beam (PPB) incident on the PPT consisted, at the time of the experiment, of electron bunches 3.17×10^{10} e^{-}in size, with electron energy 29.47 GeV. The duration of each bunch was on the order of a few tens of picoseconds. These bunches collided with the target, consisting of a six-radiation-length ($\sim$ 2-cm) slab of tungsten-rhenium alloy (75% W, 25% Re), at a rate of 120 Hz, inducing electromagnetic and hadronic showers. For purposes of calculating mQ production, we assume only electromagnetic processes are relevant. Production via other mechanisms, such as meson decay, is neglected. We further assume that calculations for fermionic mQs will suffice, with the results for bosons being fairly similar.

The principal electromagnetic production mechanisms are shown in Figure 3.1. The cross section for photoproduction (Fig. 3.1 A) is proportional to $Q^4\alpha^3Z^2$, where Q

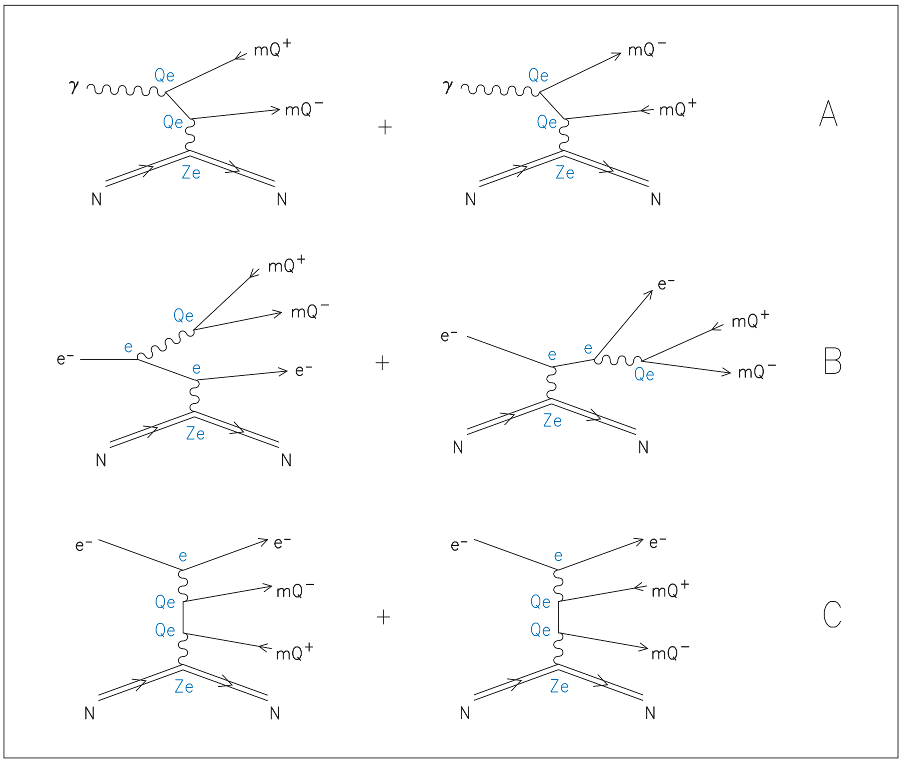

Figure 3.1: Feynman diagrams for mQ production. A. Photoproduction. B. Electroproduction, "Bremsstrahlung" mechanism. C. Electroproduction, "multiperipheral" mechanism.

is the mQ charge in units of e, and Z is the atomic number of the target nucleus. The cross sections for the electroproduction processes labeled "Bremsstrahlung" (Fig. 3.1 B) and "multiperipheral" (Fig. 3.1 C) are proportional to $Q^2\alpha^4Z^2$ and $Q^4\alpha^4Z^2$ respectively. For $Q \lesssim 0.1$ and M_{mQ} not extremely small relative to m_{e}, the Bremsstrahlung electroproduction mechanism dominates. (It is possible that for $M_{\mathrm{mQ}} \ll m_{\mathrm{e}}$, the multiperipheral process overtakes the Bremsstrahlung process, but we have been unable to properly investigate this possibility.)

3.2.1 Published Calculations

The literature contains a number of theoretical investigations of pair production of charged particles. A discussion of several of these can be found in the review article by Wright[67]. Not all the published formulas have reasonable accuracy in the case where the pair-particle mass is different from m_{e}. Among the most rigorous results with stated applicability to arbitrary mass is that of Kelner[68], and the subsequent work of Kokoulin and Petrukhin[69] (hereafter K&P) based on Kelner's result. (The latter is presented as applying to electron pair production by muons, but is readily adaptable to the more general case.) These authors provide the energy distributions of particles produced via the Bremsstrahlung and multiperipheral electroproduction mechanisms, with consideration given to screening and atomic form factors. Their formulas apply when the incoming and outgoing particles (with the exception of the target nucleus) are all highly relativistic. For reference we reprint the cross section for the Bremsstrahlung mechanism, as given in Eqn. 12 of K&P[69]:

$$\frac{\mathrm{d}\sigma\left(\mu\,\mathrm{N}\longrightarrow\mu\,\mathrm{N}\,\mathrm{e}^{+}\,\mathrm{e}^{-}\right)}{\mathrm{d}v\mathrm{d}\rho} \cong \frac{2}{3\pi}\left(Z\alpha r_{\mathrm{e}}\right)^{2}\frac{1-v}{v}\frac{m_{\mathrm{e}}^{2}}{M_{\mu}^{2}}\phi_{\mu} \tag{3.1}$$

$$\begin{aligned}\phi_{\mu} = \Bigg\{&\left[\left(1+\rho^{2}\right)\left(1+\frac{3}{2}\beta\right)-\frac{1}{\xi}\left(1+2\beta\right)\left(1-\rho^{2}\right)\right]\ln\left(1+\xi\right)+ \\ &\frac{\xi\left(1-\rho^{2}-\beta\right)}{1+\xi}+\left(1+2\beta\right)\left(1-\rho^{2}\right)\Bigg\}L_{\mu}\end{aligned} \tag{3.2}$$

$$L_{\mu} = \ln\left\{\frac{189\left(M_{\mu}/m_{\mathrm{e}}\right)Z^{-1/3}\left[\left(1+1/\xi\right)\left(1+Y_{\mu}\right)\right]^{1/2}}{1+\left[2\,m_{\mathrm{e}}\,e^{1/2}\,189\,Z^{-1/3}\left(1+\xi\right)\left(1+Y_{\mu}\right)\right]/\left[v\,E_{\mathrm{in}}\left(1-\rho^{2}\right)\right]}\right\} \tag{3.3}$$

$$Y_{\mu} = \frac{4+\rho^{2}+3\beta\left(1+\rho^{2}\right)}{\left(1+\rho^{2}\right)\left(3/2+2\beta\right)\ln(3+\xi)+1-3\rho^{2}/2} \tag{3.4}$$

where

$$\xi = \left(\frac{M_\mu v}{2m_\mathrm{e}}\right)^2 \frac{1-\rho^2}{1-v}, \tag{3.5}$$

$$\beta = \frac{v^2}{2\,(1-v)}, \tag{3.6}$$

$$e = 2.71828, \tag{3.7}$$

$$v = \frac{E_{\mathrm{e}^+} + E_{\mathrm{e}^-}}{E_\mathrm{in}}, \tag{3.8}$$

$$\rho = \frac{E_{\mathrm{e}^+} - E_{\mathrm{e}^-}}{E_{\mathrm{e}^+} + E_{\mathrm{e}^-}}, \tag{3.9}$$

E_in is the energy of the incoming muon and r_e is the classical electron radius.

To adapt this formula to the case of mQ production by electrons, we make the following substitutions: r_e is replaced by α/M_mQ; M_μ is replaced by m_e; m is replaced by M_mQ; $AZ^{-1/3}$ is replaced by $AZ^{-1/3}/m_\mathrm{e}$; and factors of M_mQ are inserted wherever necessary to make the resulting expression dimensionally correct.

3.2.2 mQ Production in the PPT

To estimate the number of mQs produced when SLAC's electron beam collides with the positron-production target, we consider all electrons and positrons in the resulting electromagnetic showers as incident particles capable of generating mQs. Shower parameters, including angular spread and path length of charged particles as a function of particle energy, were modeled using EGS4[70]. The total yield of mQs (per PPB electron) obtained via numerical integration of K&P's Eqn. 12 is shown in Figure 3.2. (For comparison, the yield from the multiperipheral process, obtained from K&P's Eqn. 12, is also shown.) Estimation of the number of mQs entering the small ($\sim$ 2-milliradian) angular acceptance of our detector required that we also obtain the angular distribution of the mQs. (The formulas of Kelner[68] and of K&P[69] do not provide angular information.) To this end we employed a Monte Carlo calculation of the cross section for the Bremsstrahlung electroproduction process (with code

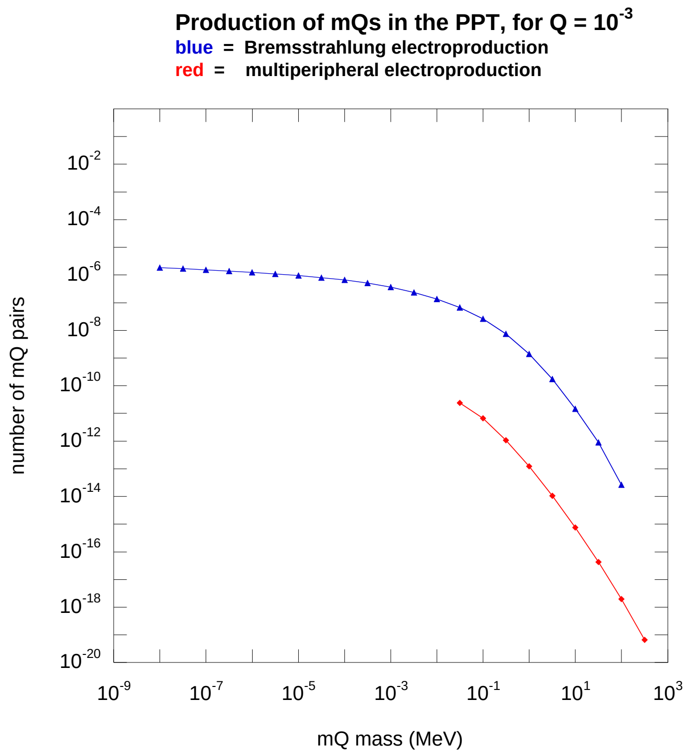

Figure 3.2: Estimate of total mQ yield, per PPB electron, based on the formulas of K&P.

graciously provided by M. Swartz). A detailed description of the Monte Carlo, and results for some representative mQ masses, are given in this dissertation's appendix. The code produced a two-dimensional histogram of mQ yield versus mQ energy and angle.

Figure 3.3 shows the total yield (per PPB electron) predicted by the Monte Carlo over a range of mQ masses, compared to the result obtained by numeric integration of K&P's formula. The agreement is excellent between 0.003 MeV/$c^2$and 3 MeV/c^2. The predicted energy distributions are also in agreement over this interval. Outside this range, however, it appears that the Monte Carlo predictions are inaccurate. To obtain the number of mQs produced within our detector's angular acceptance, we use the Monte Carlo predictions between 3 and 0.003 MeV/c^2. Below 0.003 MeV/c^2we use K&P's formula, and we make the assumption that the angular spread of the

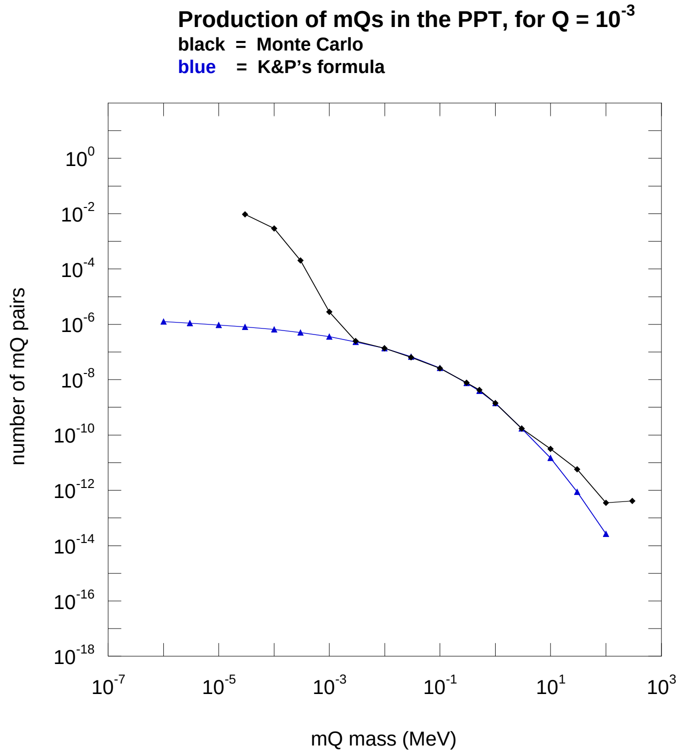

Figure 3.3: Comparison of mQ yield estimated by the Monte Carlo (upper curve) to that from the formulas of K&P.

mQs is due entirely to that of the electromagnetic showers in the target. That this assumption is justified is illustrated in Figure 3.4, where the number of accepted mQs, computed with only the angular spread of the shower, is compared to the Monte Carlo prediction. The acceptance is roughly 20% for masses below 3 MeV/c^2. Above 3 MeV/c^2, we use the total yield obtained from K&P's formula, together with an acceptance fraction extrapolated from the Monte Carlo results in the range 0.1–3 MeV/c^2. The extrapolated acceptance falls off rapidly, and crosses zero just below 100 MeV/c^2. For 100 MeV/$c^2$and above we make the conservative assumption that the mQs are spread over a 4π angular distribution. The results for the number of accepted mQs, over the mass range 10^{-9}–10^2 MeV/c^2, are shown in Figure 3.5. For most of this range (10^{-9} to about 10 MeV/c^2) the majority of mQs exit the target at an angle of less than 20 mr.

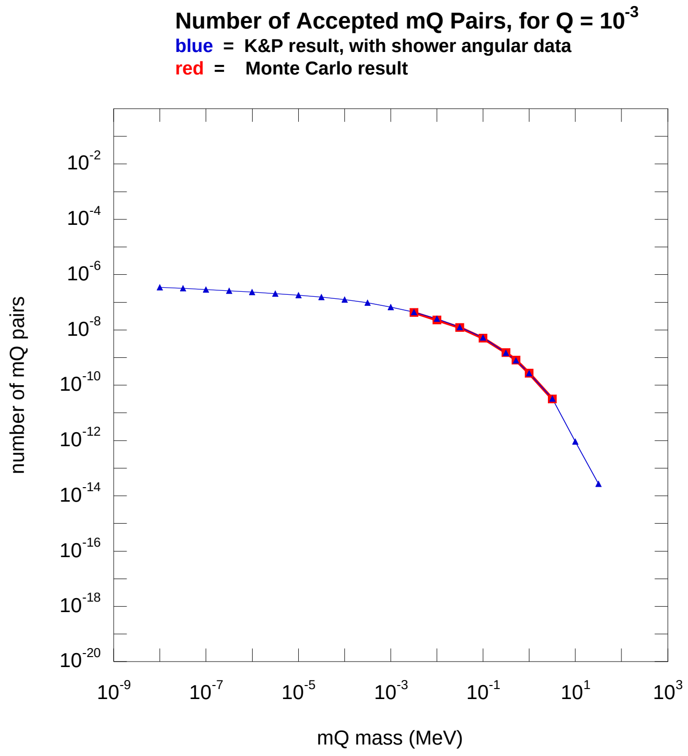

Figure 3.4: The number of mQ pairs accepted into the detector, per PPB electron, estimated via K&P's formulas (assuming the mQ angular distribution is that of the e^+e^- shower), compared to the number of accepted pairs estimated by the Monte Carlo within its range of accuracy.

3.3 Transport

A mQ from the PPT would have to traverse 84.3 meters of bedrock (consisting of sandstone with a density of 2.19 g/cm^3) in order to reach the mQ detector. For certain regions of charge-mass parameter space (particularly, high charge and low mass), energy loss in the bedrock would be sufficient to prevent mQs from reaching the detector. The principal mechanisms of mQ energy loss are ionization and the radiative processes Bremsstrahlung and e^+e^- pair production. In addition, the mQ angular spread will be affected by multiple Coulomb scattering, reducing the number of mQs accepted into the detector. The sections that follow will discuss these mechanisms, along with an additional process specific to the "hidden-sector models" discussed

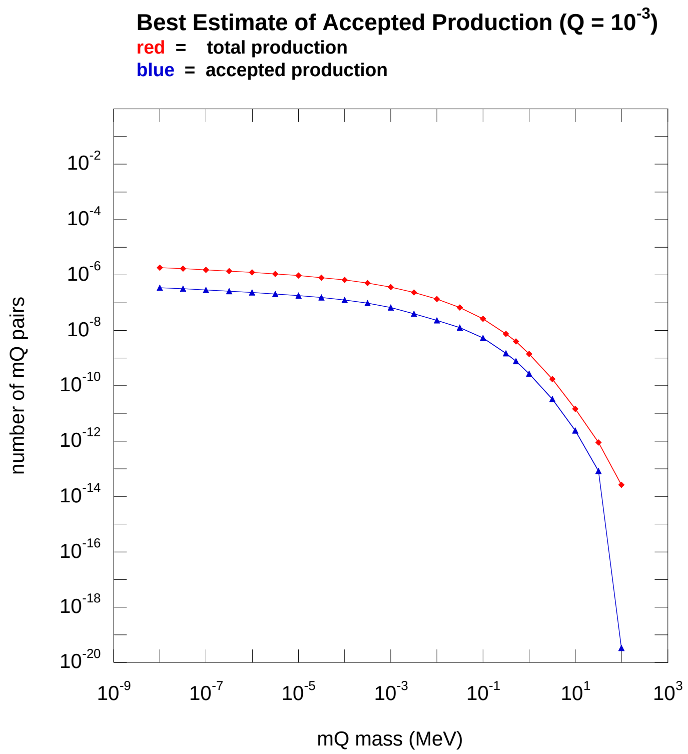

Figure 3.5: Our best estimates of total mQ yield (per PPB electron), and yield accepted into the detector.

in chapter 2, sections 6–7. The regions of charge-mass parameter space rendered inaccessible to the experiment due to the inability of mQs to reach the detector are shown in Figure 3.6.

3.3.1 Ionization Energy Loss

Energy loss of mQs to excitation and ionization is described by the Bethe-Bloch formula[71], with charge dependence contained in an overall factor of Q^2. In the mass range 10^{-9} to 10^2 MeV/c^2, for $Q > 0.8$ the highest-energy mQs produced in the PPT ($E \geq 29.0$ GeV) range out before reaching the detector. Below $Q = 0.8$, the proportion of mQs that fail to reach the detector due to ionization energy loss is insufficient to affect the results of the experiment.

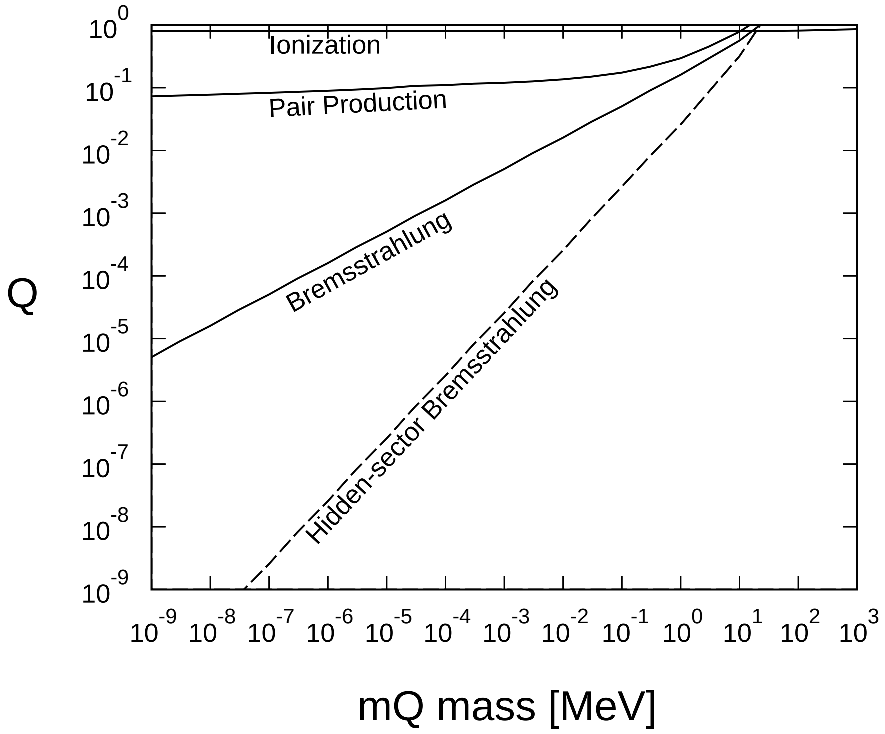

Figure 3.6: Regions of charge-mass parameter space invisible to the experiment due to mQ energy loss in the shielding. In the area above each curve, mQs could range out before reaching the detector due to energy loss by the stated mechanism.

3.3.2 Multiple Coulomb Scattering

To describe the angular spread resulting from multiple Coulomb scattering we use the formula given in the Particle Data Book[72], under the assumption that the radiation length in the formula is that for electrons, and that the formula can be applied to particles of arbitrary mass. The charge dependence of the angle is contained in an overall factor of Q, so the fraction of mQs entering the detector goes as Q^{-2}. The effect of multiple scattering is insignificant when $Q < 10^{-3}$ for mass in the range 10^{-9} to 10 MeV/c^2, and when $Q < 5 \times 10^{-2}$ for mass 100 MeV/c^2, given the the transverse area (1756 cm^2) and position (110 meters downstream of the PPT) of our detector. The predicted signal-to-noise of our experiment is quite large at these charge values (see chapter 5, sections 5–6). At greater charge, the signal increases as Q^4 (one factor of Q^2 from the mQ yield, and one from the ionization energy deposited in the detector) while the acceptance fraction decreases as Q^2, so the effect of multiple scattering never becomes large enough to prevent detection of mQs.

3.3.3 Radiative Energy Loss

Relativistic mQs with high charge and low mass can lose significant amounts of energy to Bremsstrahlung and e^+e^- pair production. The lowest-order Bremsstrahlung and pair-production diagrams are shown in Figure 3.7 (including one that's relevant only in the hidden-sector models described in chapter 2 sections 6–7). The pair-production mechanism in Figure 3.7 B is suppressed by a factor of alpha relative to Bremsstrahlung and thus can be neglected.

Bremsstrahlung

For the Bremsstrahlung cross section we use formulas 3.82 (scaled by Q^4) and 3.46–3.49 of Tsai[73] (with minor typos corrected), under the assumption that these formulas are valid for $M_{\mathrm{mQ}} \ll m_{\mathrm{e}}$. The average energy that a mQ deposits in the bedrock was obtained by numeric integration of Tsai's Eqn. 3.82 over photon energy and mQ path length. The initial mQ energy was taken to be the median value for mQs leaving the PPT at angles below 2 mr, for each mQ mass under consideration. We conservatively estimate that the sensitivity of the experiment cuts off at the charge value resulting in a 10% loss of initial energy. The portion of charge-mass parameter space thus deemed inaccessible due to Bremsstrahlung energy loss is shown in Figure 3.6.

Pair Production

For estimation of the energy loss to e^+e^- pair production, we use the cross-section formulas of K&P[69] (mentioned in section 2.1) and Eqns. 26 and 31 of Kelner[68]. To

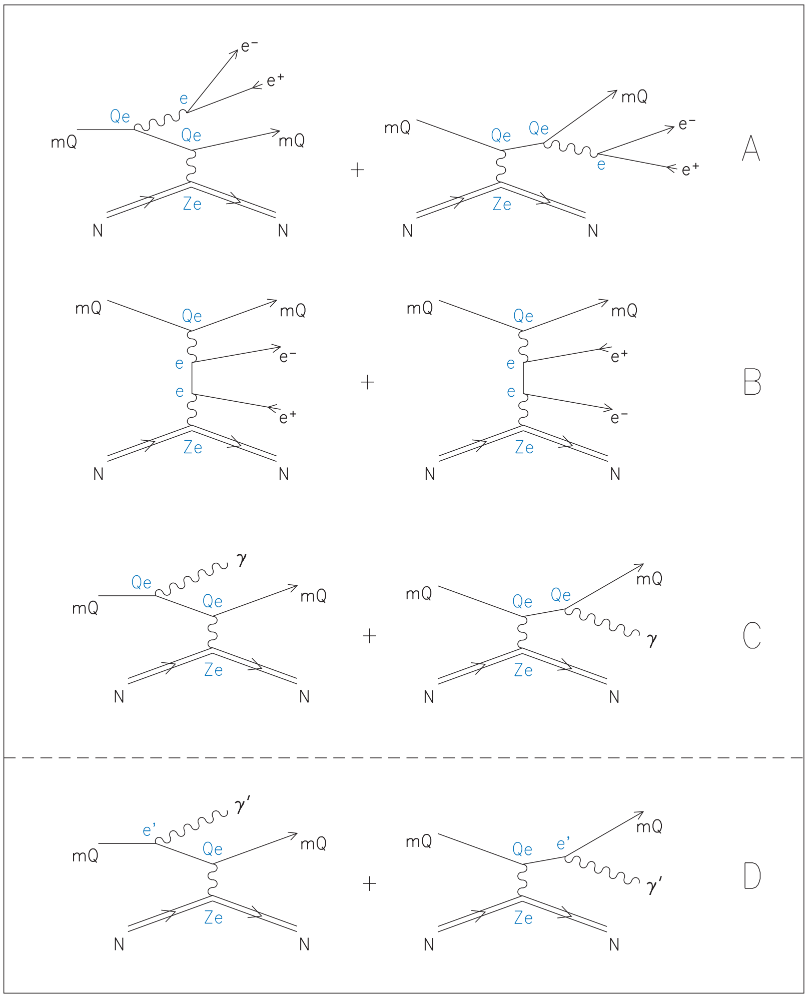

Figure 3.7: Feynman diagrams for radiative energy loss by mQs. A. e^+e^- pair production, "Bremsstrahlung" mechanism. B. e^+e^- pair production, "multiperipheral" mechanism. C. Bremsstrahlung. D. Bremsstrahlung of hidden-sector photons.

adapt Kelner's result to the case of mQs, we substitute M_{mQ} for "m," attach a factor of m_{e}^{-1} to every instance of $137Z^{-1/3}$ and $183Z^{-1/3}$, insert factors of m_{e} wherever necessary to make the expression dimensionally correct, and scale by an overall factor of Q^2. To adapt K&P's Eqn. 12, we substitute M_{mQ} for "μ" and scale by Q^2. K&P's formula was used for the mQ mass range 10^2–10^{-5} MeV/c^2. For masses below 10^{-5} MeV/c^2, Kelner's formula was used, as K&P's becomes negative in this region. (It should be noted that the validity of these formulas for $M_{\mathrm{mQ}} \ll m_{\mathrm{e}}$, both here and as applied to mQ production in section 2.2, has been assumed by us without any attempt at verification.)

Numeric integration over pair energy and mQ path length provides the energy lost by a mQ crossing the bedrock. We again take as the initial mQ energy the median energy of mQs exiting the PPT at angles below 2 mr, and calculate the charge for which 10% of this energy is lost in the rock. The portion of charge-mass parameter space invisible to the experiment due to $\mathrm{e}^+\mathrm{e}^-$ pair production is shown in Figure 3.6. This region is subsumed in the region invisible due to Bremsstrahlung, despite the stronger Q dependence of the Bremsstrahlung cross section.

Hidden-sector Bremsstrahlung

In chapter 2, sections 6–7, a set of models were discussed wherein mQs represent hidden-sector fermions that couple to hidden-sector photons. Pursuant to these models, a mechanism for energy loss exists wherein mQs radiate hidden-sector photons. The lowest-order diagram for this process is shown in Figure 3.7 D. If allowed, this process will dominate over the radiative processes discussed above. To estimate the energy lost to hidden-sector Bremsstrahlung, the same formulas as for conventional Bremsstrahlung can be used, but with an overall factor of Q^2 rather than Q^4, and with one factor of α replaced by the hidden-sector coupling constant α'. Figure 3.6 shows the portion of charge-mass parameter space rendered inaccessible due to hidden-sector Bremsstrahlung, for the case $\alpha = \alpha'$.

Chapter 4

Experiment Setup

4.1 Introduction

An electron accelerator such as SLAC was suggested as an ideal location for a mQ search in Dobroliubov and Ignatiev[7]. The electromagnetic showers generated when SLAC's high-current beam collides with a target provide an excellent environment for the production of mQs. These mQs are predicted to have a low angular spread ($\lesssim 20$ mr, see chapter 3), allowing for high flux into a suitably placed detector. In addition, the short time duration of the electron bunches of SLAC's beam would result in a mQ signal that is well defined in time. Restriction of data collection to a narrow window surrounding the expected signal time allows for a sizeable improvement in signal-to-noise ratio.

This chapter gives an overview of the experiment setup for the mQ search, followed by a detailed description of the experiment site, the expected sources of background at the location of the detector, the design and operation of the detector, the trigger and data-acquisition systems, the calibration (both in time response and pulse height) of the detector, and the methods employed to minimize background noise.

4.2 Overview of Experiment Setup

Midway down the length of the SLAC linac, a beam of electrons is diverted and sent to collide with the SLC positron production target. At the time of our experiment, this beam had 3×10^{10} electrons per bunch, 120 bunches per second, and an energy of 29.5 GeV per electron. The bunch duration was a few tens of picoseconds. The target consists of a tungsten-rhenium alloy six radiation lengths ($\sim$ 2 cm) in thickness. It is located roughly five meters underground. There is a toroid just upstream of the target, which provides a measure of the number of electrons in each bunch. We installed our detector 110 meters downstream of the target, along the axis of the beam (and thus also five meters underground). Solid bedrock, consisting of sandstone with a density of 2.2 g/cm^3, filled 84 meters of the space between the target and the detector. The rock provided all the shielding necessary to block conventional charged particles (including muons, which ranged out just before reaching the detector). A little upstream of the detector we installed small scintillation counters to monitor the muons. This allowed us to confirm that our detector was properly aligned, and provided timing information critical for predicting the time at which mQ bunches would arrive. The detector, designed for sensitivity to the ionization trail of a passing relativistic mQ, consisted of plastic scintillator, of length 1.3 meters along the beam direction, coupled to eight-inch hemispherical photomultiplier tubes (optimized for single-photon counting). It had a width of 42 cm, covering angles up to 2 mr, and providing an acceptance of roughly 20% for mQs with mass below 3 MeV/c^2. The trigger was constructed from NIM and CAMAC modular electronics, and data acquisition was carried out on a desktop computer.

4.3 Experiment Site

Figure 4.1 shows an aerial view of the experiment site, including the locations of the PPT, the muon-counter array, the mQ detector and the building containing the

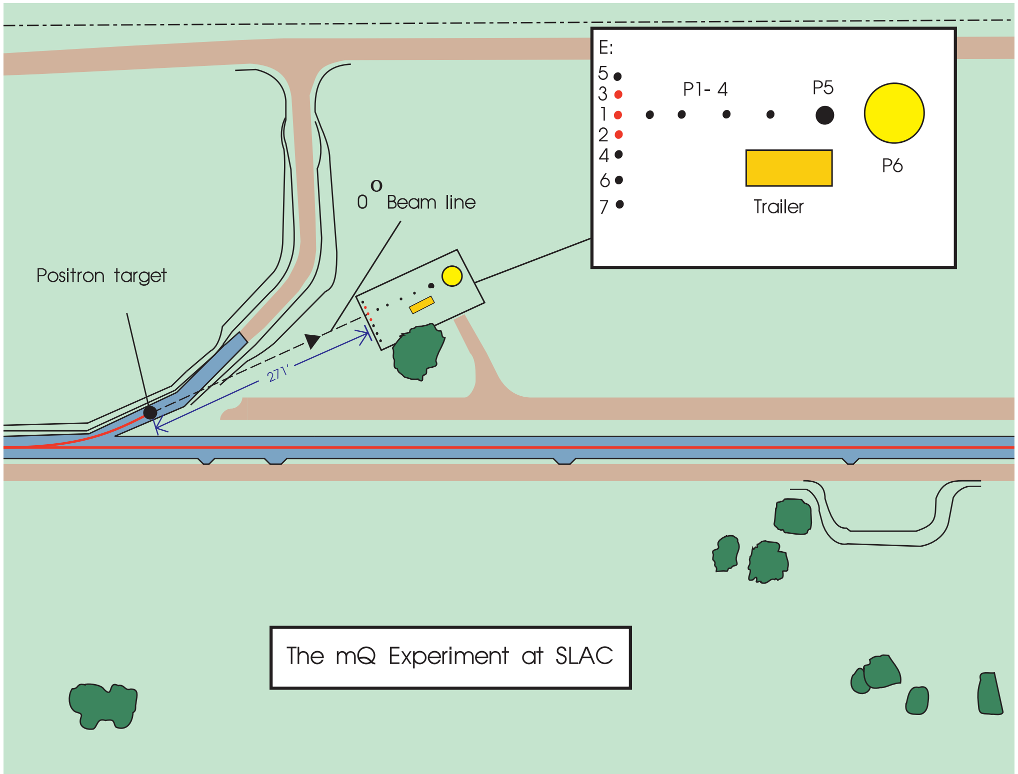

Figure 4.1: Aerial view of the experiment site. The accelerator is shown in blue, and the location of the PPT ("positron target," in the figure) is shown on the left. The white rectangle in the upper right is an expanded view of the experiment facilities (in the smaller rectangle), including the holes (labelled E1–E7 and P1–P5) in which muon flux was measured, the electronics trailer, and the pit (P6) that housed the detector.

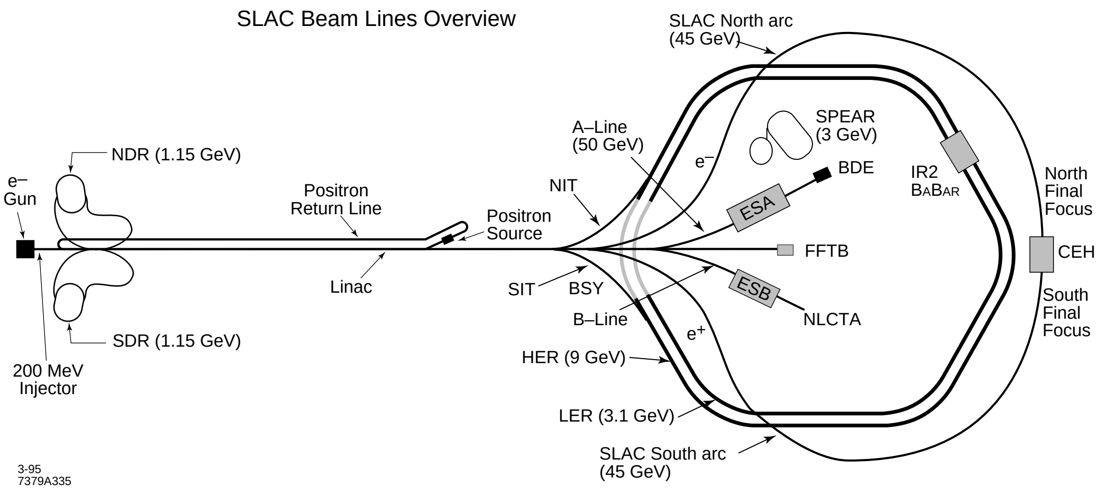

Figure 4.2: Schematic of SLAC, showing the location of the PPT ("Positron Source").

trigger and data-acquisition electronics.

4.3.1 The PPT and its Surroundings

A diagram of SLAC (not to scale) illustrating the location of the PPT in relation to the accelerator is given in Figure 4.2. Midway down the length of the accelerator, part of the SLAC electron beam is diverted and sent toward the PPT. This positron-production beam (PPB) consisted, at the time of the experiment, of bunches containing on average 3.17×10^{10} electrons each, generated at a rate of 120 Hz, with an electron energy of 29.47 GeV. The time required for a bunch to travel past a fixed point (or completely impact with the PPT) was on the order of 10 picoseconds. A timing signal (TS1) synchronized, up to an unknown but fixed offset, with bunch arrival at the PPT was available from the accelerator electronics, and was used extensively in our trigger system. The offset was adjustable within a 2-ms period bracketing the bunch arrival time, and the signal itself was generated regardless of whether an actual PPB bunch was present. The number of electrons in each bunch was monitored via a toroid (the SLC toroid "PT01") just upstream of the PPT. The signal from this toroid, preshaped into a square pulse with height proportional to the charge of the bunch, provided both an indication of bunch presence and (summing over many pulses) a measure of the total charge incident on the PPT over the course of the experiment. Other accelerator data, recorded in SLAC's SLC database and accessible to the mQ search, included the horizontal and vertical angle of the PPB (up to an unspecified but fixed offset), the average rate at which PPB bunches were produced (nominally 120 Hz, but subject to downward fluctuations due to imperfect accelerator performance), the average electric charge of the bunches, and the average energy of the PPB electrons.

The PPT consists of a slab of Tungsten-Rhenium alloy (75% W – 25% Re), 2-cm (6 radiation lengths) in thickness. It is located 10.3 meters to one side of the accelerator, and 5.3 meters underground. Downstream of the PPT are several sections of beam pipe and numerous magnets for gathering and redirecting positrons (but essentially an open drift space for weakly-interacting mQs), followed, at a distance of 23.8 meters, by a concrete wall separating the PPT's enclosure from the surrounding bedrock. The PPB makes an angle of 24° with the accelerator, and is within 0.053° of horizontal, just before arriving at the PPT. Its direction is subject to fluctuations of ± 1 milliradian.

The bedrock surrounding the PPT consists of sandstone with a density of 2.19 ± 0.14 g/cm^3. Rather than install shielding to keep shower remnants (including muons) out of the mQ detector, the detector was placed a sufficient distance from the PPT to allow the bedrock itself to perform this function. Low solid-angle coverage was not expected to be a problem, since our calculations (see chapter 3, section 2.2) predict a very narrow ($\lesssim 20$ mr) mQ beam.

4.3.2 The PPT Muons

The range of the highest-energy (29.36 GeV) muons produced in the PPT determined the minimum distance at which the detector could be installed. In addition, the PPT muons provided the experiment with two very valuable pieces of information: a means of experimentally locating the axis of the PPT-produced particle beam, and a time

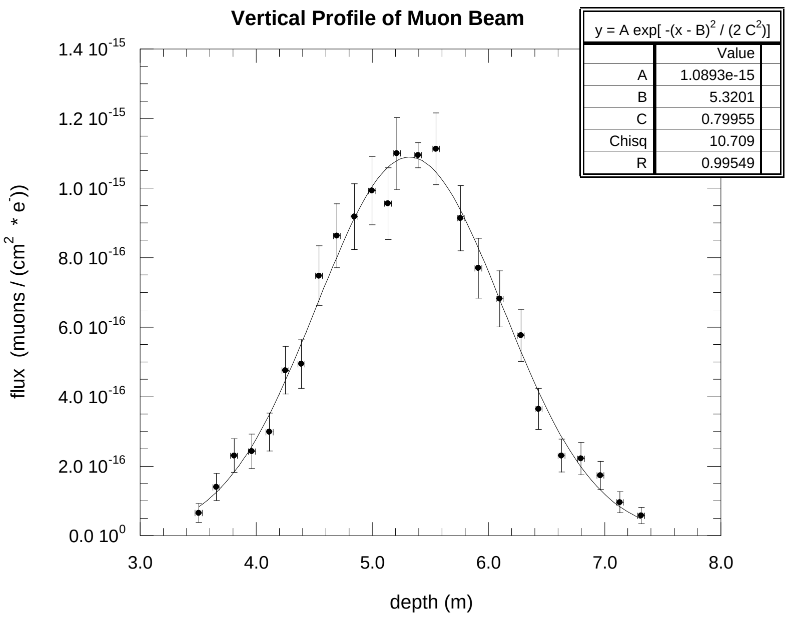

Figure 4.3: Measured vertical profile of the muon beam, with gaussian fit.

reference indicating the expected time of arrival of mQ bunches at the detector.

The maximum range of straggled muons was determined by measuring muon flux at PPT depth in several holes dug along the axis (located using survey data) of the PPT particle beam, at various points within the predicted range-out interval. Small (20-cm square) scintillation counters sensitive to single muons were used for this purpose. At a distance of 82.6 meters from the PPT, less than one muon per PPB bunch was detected, and in the next 4.6 meters the flux dropped by a factor of 300. We conclude that, for a PPB energy of 29.47 GeV, the muons range out in fewer than 87.2 meters.

At a distance of 82.62 meters from the PPT, the depth of the muon beam axis and the vertical spread of the beam were determined by measuring flux at several closely-spaced depths. The results, fit quite well by a gaussian with mean of 5.34 meters and standard deviation of 0.79 meters, are shown in Figure 4.3. The horizontal position of the beam axis, and the beam's horizontal spread, were determined by fitting a

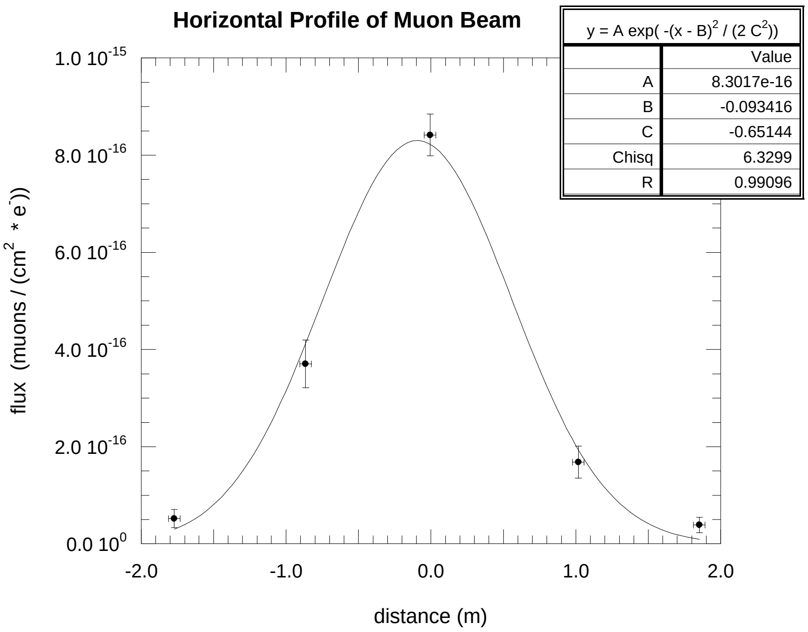

Figure 4.4: Measured horizontal profile of the muon beam, with gaussian fit.

gaussian to flux measurements made at constant depth in three holes positioned along a line perpendicular to the beam direction. The results are shown in Figure 4.4. (The spread is about what one would expect from multiple scattering in the bedrock.)

Determined in this way, the axis of the muon beam is not entirely the same as that of the PPB, however. Muons that do not travel down the center of the beampipe downstream of the PPT lose energy in the pipe and surrounding magnets before entering the bedrock. Since only the highest-energy muons were able to reach our muon counters, we observed only those muons that had been aligned with the beampipe. A beam of mQs would not be significantly affected by objects downstream of the PPT, and would thus remain aligned with the PPB. To determine the magnitude of the difference between the PPB and muon-beam directions, we analyzed a dedicated experiment wherein the PPB was steered to plus and minus one milliradian of nominal, in the vertical and horizontal directions. The measured position of the muon-beam center did not change, but the total measured flux of muons was affected. Fitting flux versus angle with a gaussian over three data points (in the horizontal and vertical directions), we estimated the PPB angle corresponding to maximal flux, which we assume represents the angle of the beampipe. The difference between the PPB direction and that of the muon beam, taking into account fluctuations in PPB angle recorded in the SLC database during the running of the mQ search, was quite small: 0.6 ± 0.6 mr.

The scintillation counters used in these measurements each consisted of a 20-cm square, 2.5-cm thick sheet of plastic scintillator coupled to a 2-inch diameter photomultiplier tube (PMT) via a plastic lightguide. Once the mQ detector was in place, a transverse array of five of these counters (shown in Figure 4.5) was permanently installed so as to continually monitor muon flux and timing.

The time distribution of muon events in the central counter (relative to the timing signal "TS1" discussed in the previous section) was narrow: about 3 ns. This time spectrum is shown in Figure 4.6. Both muons and mQs, if present, would be relativistic upon arrival at the muon counters, and would thus arrive essentially simultaneously. This allows us to extrapolate from the muon arrival time to the expected arrival time of mQs at the detector. (The distance between the muon-counter array and the detector was determined using data from a survey.)

4.3.3 Detector Position and Surroundings

The detector was positioned in line with the PPB, 5.3 meters below ground and 110.11 meters downstream of the PPT (with 86.3 meters of bedrock intervening). This was more than 22.9 meters beyond the range of the muons. With an area of 1760 cm^2 transverse to the beam, the detector covered a solid angle of 1.2×10^{-6} steradians (0 to 2 mr, linearly). The detector was housed in a 3.7-meter diameter cylindrical pit excavated from the bedrock. (The pit had walls lined with steel sheet, floor of poured concrete with a sump along the perimeter, and a removable wooden roof. Electrical power, telephone lines and outside air were piped in, and excess water

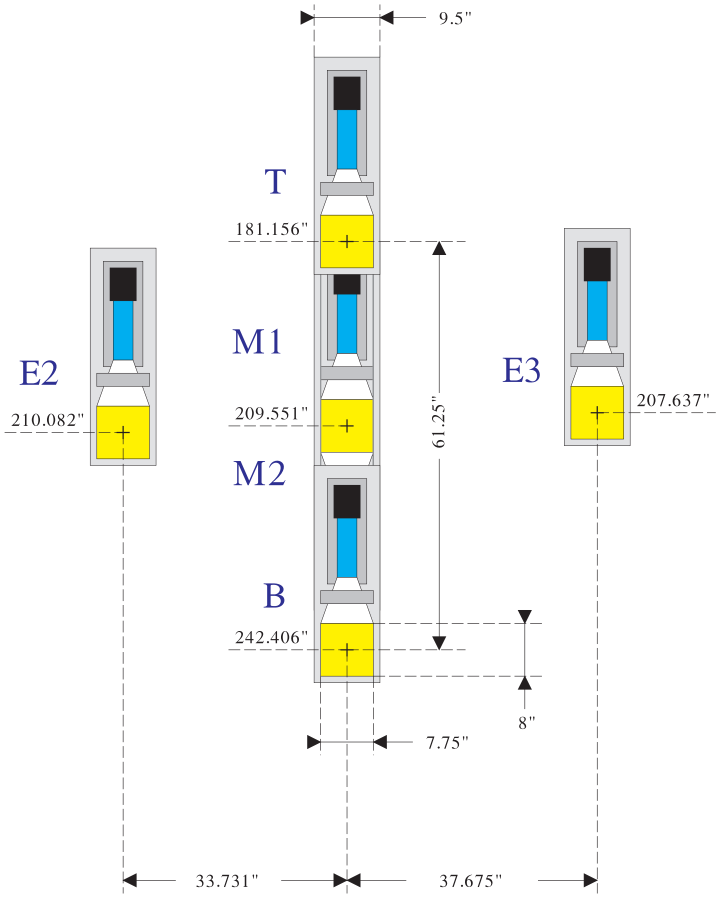

Figure 4.5: Muon counter array. The scintillator panels (shown in yellow) were roughly one meter apart.

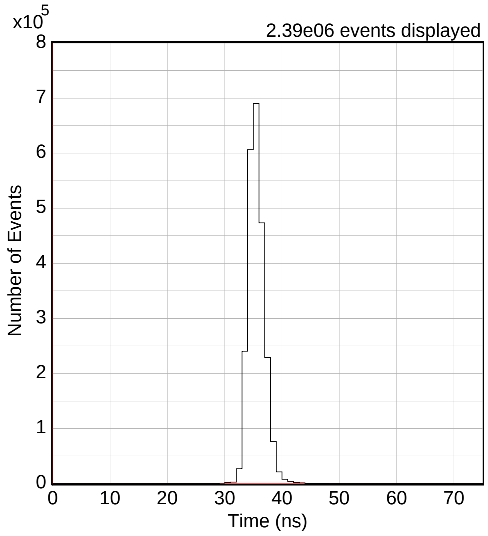

Figure 4.6: Time spectrum of muon events.

was removed via sump pumps.) The detector rested on a mobile platform capable of 1-meter excursions along a line perpendicular to the beam axis, for purposes of gathering background data.

A survey of the experiment site, including the locations of the PPT and the muon-counter array, was carried out to pinpoint the correct spot for detector installation. Following the installation, the detector's alignment with the PPT beam was verified by way of the muons: the axis of the muon beam was determined via the muon-counter array, and extrapolated to the detector's location. The detector was found to be well aligned, its axis within 2.3 cm of the muon beam axis.

The trigger and data-acquisition electronics for the experiment resided above ground, next to the pit, in a small air-conditioned trailer. An ethernet fiber-optic cable linking the trailer with the SLAC network provided access to SLAC's MCC computer, allowing us to query the SLC database and manipulate the TS1 timing signal used in the trigger.

4.3.4 Background Sources at Detector Location

Of the particles generated in the PPT, the only ones capable of reaching the detector were neutrons (including "skyshine" neutrons scattered down from the atmosphere), neutrinos, and any weakly interacting species such as mQs. Background sources unrelated to the PPT included cosmic-ray muons, cosmic-ray neutrons, radioactivity in the bedrock, and x-rays from the accelerator, in addition to backgrounds intrinsic to the detector and its associated electronics. With the exception of accelerator x-rays, backgrounds from sources unrelated to the PPT were not time correlated to the beam pulses, and thus could be greatly reduced by restricting data collection to a narrow window surrounding the mQ bunch arrival time.

The estimated number of events due to PPT neutrons, based on BF_3-monitor data at the experiment site, was 0.03 per PPB pulse. These events would occur at least 5 μs after arrival of a mQ bunch[76], however, and could therefore be excluded by use of a shorter data window. PPT neutrinos were produced primarily via decay of PPT pions and kaons. The expected number of neutrino interactions in the detector was estimated based on calculations by Rothenberg for the SLAC E-56 experiment. Substituting the appropriate parameters for target material, target thickness, detector solid angle and detector nucleon density (leaving the beam energy, 20 GeV, unchanged), leads to a prediction of 10^{-2} neutrino interactions per Coulomb of PPB electrons[76]. In addition, roughly 10 interactions per Coulomb would take place in the bedrock just upstream of the detector. The amount of PPB charge observed during the mQ search was on order one Coulomb, so the background from neutrino-related events would be negligible compared to PMT dark noise.

The flux of cosmic-ray neutrons, and the abundance of radioactive isotopes in the bedrock, were measured experimentally.[77]. The neutron flux ($(5\pm2)\times10^{-3}$neutrons/ $(\mathrm{cm}^2\mathrm{s})$) is an insignificant source of background, while the flux of gamma rays from radioactive decay ($6 \pm 2\gamma/(\mathrm{cm}^2\mathrm{s})$) results in a background rate that can be reduced by over four orders of magnitude with a 250-ns data window, and an additional two orders of magnitude with 10 cm of lead shielding around the detector[78], to a rate of one event per 6000 data windows. X-rays from the accelerator, seen in scintillation counters at ground level, were not observable in either the muon counters or the mQ detector below ground. Noise intrinsic to the detector, followed distantly by cosmic-ray muon events (neither of which was time correlated to mQ-bunch arrival) were the dominant sources of background for the experiment. A discussion of intrinsic backgrounds will be presented in section 7.

4.4 The mQ Detector

In order to gain maximal sensitivity to the ionization induced by a passing mQ, we employed a scintillation counter as our mQ detector. It was designed to provide a fairly long (1.3-meter) path length over which to detect mQ interactions, and to have sensitivity to the smallest possible energy deposition, a single molecular ionization. (For mQ charge $Q < 10^{-3}$, the likelihood that a mQ interacts even once while crossing 1.3 meters of scintillator is quite small.)

4.4.1 Scintillator and PMTs

Plastic scintillator offered clear advantages in terms of fast time response and ease of handling. We selected "BC 408" plastic scintillator manufactured by Bicron. This type consists of an organic phosphor dissolved in polyvinyltoluene. According to the manufacturer, it has a risetime of 0.9 ns, a pulse width of 2.5 ns, and a light attenuation length of greater than 2 meters. It emits violet photons of peak wavelength 425 nm.

The PMTs employed, model "9353 KA" from Thorn EMI (now known as Electron Tubes, Inc.) are hemispherical and 8 inches in diameter. These have a bialkali photocathode and an envelope constructed of low-radioactivity borosilicate glass. They are designed to be efficient for single-photon counting. At room temperature and 10^7

gain, they have a dark count rate on the order of 1 kHz, which decreases to a few hundred Hz upon cooling to -20^o C. According to manufacturer specifications, at peak wavelength (360 nm) these PMTs have a quantum efficiency greater than 25%, and at 10^7 gain the variation in transit time of single electrons from the cathode is roughly 3 ns.

4.4.2 Detector Design

The mQ detector consisted of four separate scintillation counters, providing altogether a $42 \times 42 \times 137$-cm volume of scintillator with a 131-cm path length for potential mQs. The counters were optically and electrically isolated from one another. Each counter consisted of a $21 \times 21 \times 137$-cm block of polished BC 408 scintillator (with a hemispherical depression carved in one end to accommodate the PMT) optically coupled via Bicron "BC 630" silicone grease to a Thorn EMI 9353 KA photomultiplier tube. The end affixed to the PMT was shaped so as to act as a short conical lightguide. A pair of green light-emitting diodes (LEDs) were mounted on the opposite end to allow for periodic tests of the counter's performance.

To optimize light-collection efficiency, the scintillator was wrapped in aluminum foil, followed by a protective layer of black plastic sheet. The exposed portion of the PMT was enclosed in a pyramidal cap of copper foil, attached to the aluminum foil, in order to prevent cross-talk between the PMTs. Both the aluminum foil and copper foil were grounded. Ambient magnetic fields in the region of the PMT were attenuated by a surrounding layer of Netic μ-metal sheet. Figure 4.7 shows a cross section of a completed counter.

The voltage divider for the PMT was somewhat modified from the usual design employed in single-photon counting. It lacked the large capacitors between final dynode stages that serve to minimize the drop in voltage that occurs during events with large pulse height. Its use was motivated by the observation of "afterpulsing" in a prototype counter following large pulse-height events (see section 7), and was

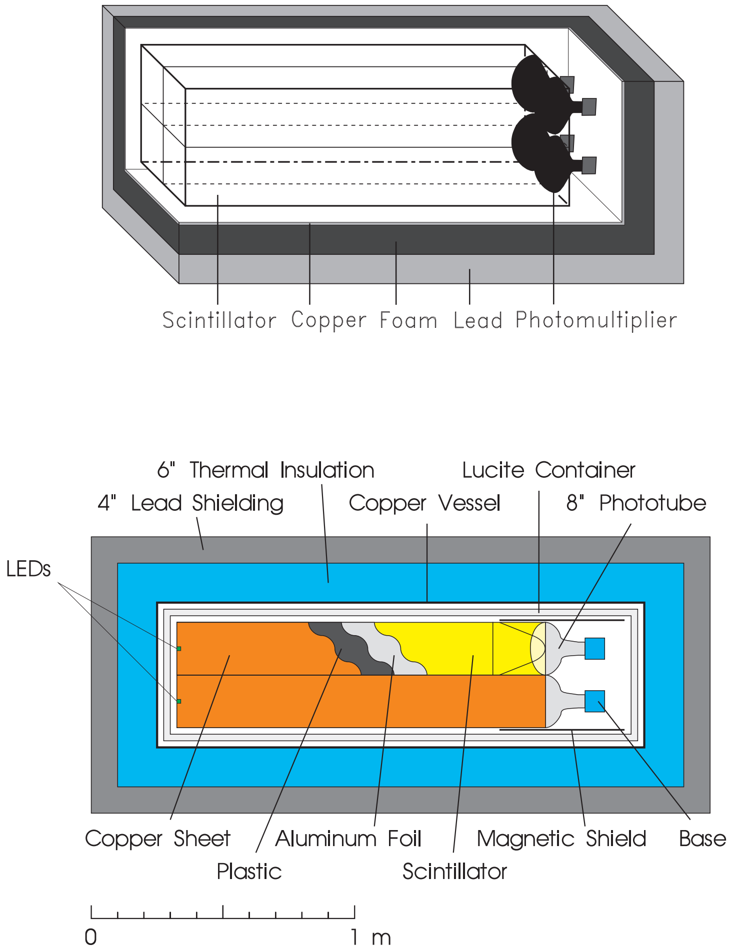

Figure 4.7: Cut-away view and cross section of the mQ detector.

intended to minimize disturbance to the PMT under such circumstances. (Removing the capacitors resulted in a factor-of-two decrease in noise rate.) In addition, an RC circuit at the anode was inserted to eliminate reflections along the high-voltage line.

The four scintillation counters were arranged parallel to one another in a 2×2 array, with 1-mm copper sheet in between and around the exterior (for thermal conduction during cooling). Thermistors were attached in the center, on one side, and at each end of the array. A lucite box surrounding the assembled detector provided structural stability.

4.4.3 External Systems

During operation the detector was enclosed in a solid-copper, light-tight box with sides 0.3 cm in thickness that functioned as both a Faraday cage and a refrigerator. The box was grounded. Fluid from a chilled liquid bath was pumped through copper tubing welded onto the sides of the box in order to maintain the detector at optimal temperature (5^o C). Dry air was circulated through the interior to inhibit condensation, and an external layer of 15-cm thick polystyrene foam provided thermal insulation. This in turn was enclosed in a 10-cm layer of lead shielding to minimize entry of natural background radiation.

Signals from the PMTs were sent into a high-speed amplifier (specifications to be discussed in section 4) which resided on top of the lead shielding. The driving pulses for the LEDs were produced in a pulse generator, also situated atop the lead shielding, which received trigger signals from the above-ground electronics. Penetrating from the exterior of the lead to the interior of the copper box, on the side opposite the PMTs, was a pneumatic tube containing an encapsulated ^{241}Am radioactive source (1 μCi). The source usually resided in the end external to the lead, but could be sent inside the copper box for periodic calibration of the detector.

Amplified signals from the PMTs and signals from the thermistors were carried to the electronics via "RG 238" coaxial cables (a type designed to minimize signal slewing) 23 meters in length. High voltage was supplied to the PMTs over 30-meter segments of "Type C" coaxial cable. All of the cables were found to carry noise into the copper box, so low-pass filters were incorporated into the thermistor and high voltage lines.

4.4.4 Running Conditions

To minimize dark noise the PMTs were operated with cathodes grounded and positive high voltage applied to the anodes. The voltage applied to each PMT was rather low (884, 1188, 975 and 1158 volts, respectively, producing a gain of roughly 4×10^6) with the consequence that the voltage difference between photocathode and first dynode was only about 1/2 the recommended minimum value of 600 volts. This was deemed necessary due to an unexpectedly large increase in noise rate at higher voltage, but may have had an adverse effect on the efficiency of collection of photoelectrons from the cathode.

The detector was maintained at a temperature of 5^o C during normal operation. Investigations of noise rate versus temperature revealed a (reproducible) increase in noise rate as the temperature was reduced below 0^o C, a behavior for which we have no explanation. (Tests of the PMTs alone, prior to incorporation into the detector, showed a steady decrease in dark noise with decreasing temperature over the range +20^o C to -20^o C.) The minimum of the noise-vs-temperature curve for the detector as a whole was found to occur at 5^o C.

4.5 Trigger and Data Acquisition System

Data collection was restricted to a 250-ns time window bracketing the expected time of arrival of a mQ bunch at the detector. The start of the window coincided with the time signal TS1 obtained from the accelerator. The time and pulse height (more accurately, integrated charge) of PMT pulses from the muon counters and the mQ detector were recorded in CAMAC TDCs (LeCroy model 2228A) and ADCs (LeCroy model 2249W). We adjusted the offset of TS1 such that the muon signals came 60 ns after the start of the data window.

Before traversing the 23 meters of cable linking the detector to the above-ground electronics, pulses from the detector's PMTs were sent to a fast amplifier (of a type originally designed for the Mark III straw chamber). This device had an amplification factor of roughly 40, noise of 10 mV (peak to peak), and a risetime of 1 ns. It saturated at 3 V (well beyond the point of PMT saturation at our operating voltage) and had high input impedance, allowing for subsequent use of the original unamplified PMT signal. The height of an amplified PMT pulse from a single photoelectron (SPE) was roughly 150 mV upon arrival in the electronics trailer, while that from a cosmic-ray muon in the detector was over 1 V. The typical width of an SPE pulse was 8 ns.

The TS1 time marker was generated even in the absence of a PPB bunch. The presence of a bunch was indicated by a pulse from the toroid upstream of the PPT. (This toroid pulse was available to us only after preshaping, which entailed a delay on the order of 60 μs.) Data was collected regardless of whether a PPB bunch was present, but those events that did not occur in conjunction with a toroid pulse were recorded separately from the rest. In this way a background data set was gathered during the same time period that the main data set was obtained.

4.5.1 Main Detector Trigger

A schematic of the main trigger for the experiment is shown in Figure 4.8. For each of the four counters in the mQ detector, the PMT signal was sent into three separate modules of the fast amplifier. The pulse height of one of the amplified signals, and of the unamplified signal, were recorded in an ADC. (All ADCs were given a 500-ns gate with leading edge determined by TS1, on each TS1 pulse. TS1 also provided the

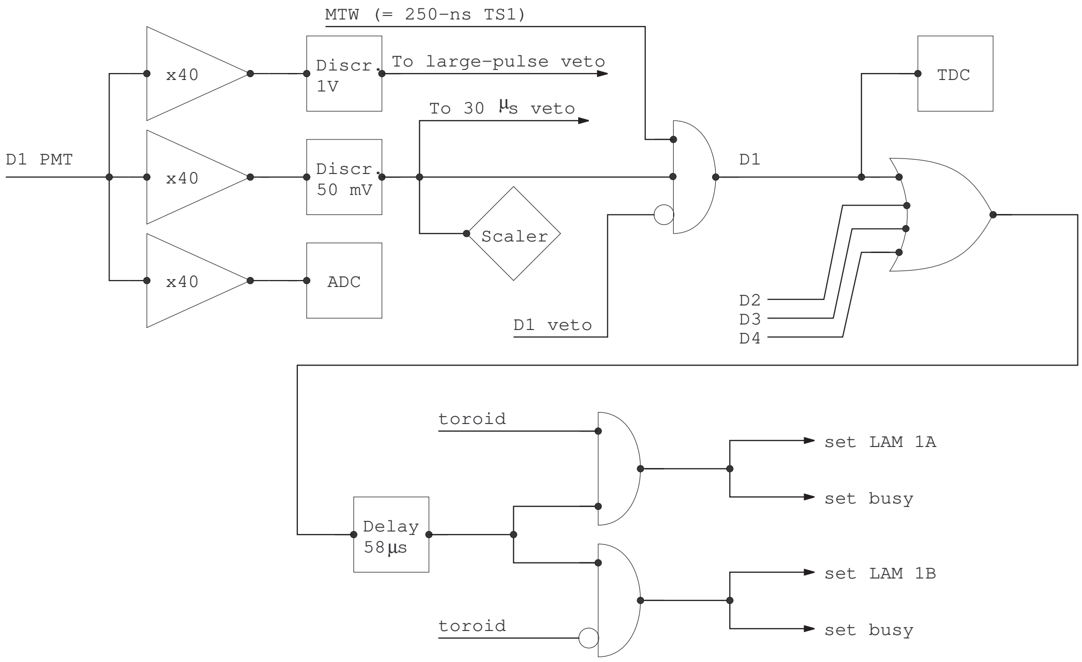

Figure 4.8: Schematic of the main trigger.

'start' for the TDCs.) The second amplified signal was sent to a discriminator with threshold 50 mV (1/3 the pulse height of an SPE) and output-pulse width of roughly 30 ns. One output of this discriminator went to a CAMAC scaler for monitoring the noise rate of the counter. Another output (along with the third amplified signal, after discrimination at a threshold of 1 V) was used in a system (described in section 4.4 below) designed to veto noise pulses. The third output went to a logical AND with the main timing window (MTW). The MTW consisted of TS1 stretched to a length of 250 ns. Discriminated PMT pulses coinciding with the MTW were combined with those of the other three counters in a logical OR. The output of the OR was then delayed sufficiently to allow for coincidence with the toroid signal, if present. In the event that a delayed signal from the OR coincided with a toroid pulse, a LAM ("LAM 1A") was set. (LAM = "Look At Me," a cue for the computer to read the data stored in the CAMAC modules.) A special "busy" level was also set, which would remain set until the computer had finished reading and clearing the CAMAC modules (ADCs and TDCs). The busy level inhibited generation of a new MTW,

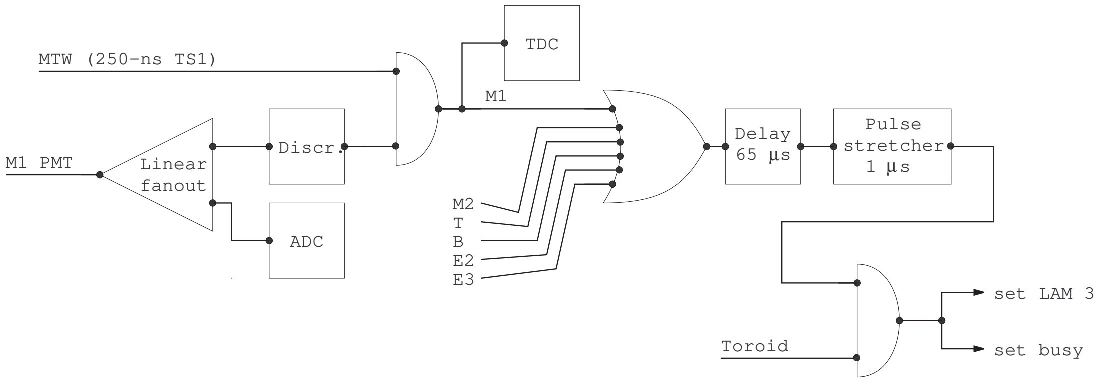

Figure 4.9: Schematic of the trigger for muon events.

inhibited gating of the ADCs and starting of the TDCs, and inhibited the otherwise automatic fast-clear of the CAMAC modules. (For most TS1 pulses there was no PMT pulse in coincidence with the MTW. The ADCs and TDCs would not overwrite their data if given a new gate before being read, so data from uninteresting gates had to be actively erased. A second timing signal, TS2, from the accelerator, arriving 1 ms in advance of TS1, triggered clearing of the ADCs and TDCs if there was no PMT pulse in the previous MTW.) If the delayed signal from the OR of the four counters did *not* coincide with a pulse from the toroid, a different LAM ("LAM 1B") was set, along with the busy level. The data-acquisition computer read and stored the data from all four counters (and cleared the CAMAC modules) after each LAM.

4.5.2 Muon Event Trigger

The time and pulse height of PMT pulses from the muon counters were recorded in ADCs and TDCs. LAM 1A and LAM 1B from the main detector trigger initiated readout of muon counter data as well as detector data. However, a separate, muon-only trigger allowed for observation of the muon beam without requiring activity in the mQ detector. A schematic of this trigger is given in Figure 4.9. The trigger is basically a simplified version of the main detector trigger. Two copies of each muon counter's PMT signal were made in a linear fan-out. One copy went to an ADC. The

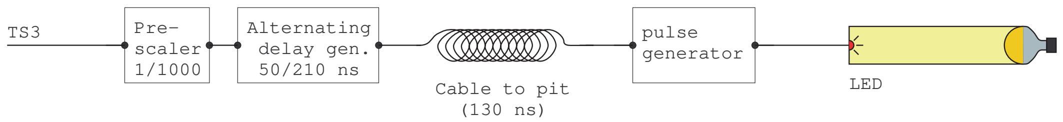

Figure 4.10: LED-driving circuitry.

other was discriminated, then sent to a logical AND with the MTW. One output of the AND went to a TDC, and the other to a logical OR of all the muon counters. The output of the OR was delayed (sufficiently to coincide with a toroid pulse, if present), then sent to a logical AND with the toroid signal. If there was a muon-counter event in conjunction with a toroid pulse, a muon LAM ("LAM 3") was set, along with the busy level.

4.5.3 LED Driver

Various aspects of detector and trigger performance were monitored by way of the LEDs, including overall deadtime, stability of time response, and stability of time resolution. The LEDs (one on each counter) were driven by the electronics shown in Figure 4.10. A timing signal, TS3, from the accelerator was adjusted so as to arrive 320 ns ahead of TS1. One out of every thousand TS3 pulses was sent to a delay generator that alternated between a delay of 50 ns and 210 ns. The delayed pulse was carried over RG 238 cable (23 meters) to the trigger input of a pulse generator situated atop the detector, whose output powered the LEDs. (The LEDs were bright enough to generate a fairly large PMT pulse.) The result was that in 0.1% of MTWs an LED event was recorded. The delays were chosen so that the LED events recorded in the TDCs occurred alternately near the beginning and near the end of the timing window. Instability in time resolution would be reflected in a change in width of the LED peaks in the TDC time spectra. Changes in time response would be seen as a shift in the positions of the LED peaks. And the number of LED events recorded over a given period of time, compared to the number of pulses sent to the LEDs, gave a practical measure of overall system deadtime. Events occurring in conjunction with an LED pulse were recorded in such a way that they could be distinguished from normal events during offline analysis.

4.5.4 Veto System

Observations of noise in the mQ detector indicated a significant increase in noise rate following passage of a cosmic-ray muon through the scintillator. More than a millisecond was required for the noise rate to return to normal after such an event. Additionally, noise pulses (particularly small ones) were seen to cluster in bunches lasting several tens of microseconds. (The mechanism behind this clustering is unknown to us.) In order to reduce the impact of these background events, a system was set up to veto data collection in the aftermath of a cosmic ray or in the midst of a noise cluster. Each of the four counters had a separate veto system. If one of the counters produced a PMT pulse of cosmic-ray size (> 1 V) in the 2 ms before the start of the MTW, or a pulse of SPE size or larger (> 50 mV) in the 30 μs before the start of the MTW, then that counter's ability to generate a LAM for the given MTW was blocked. A schematic of the veto system is shown in Figure 4.11. A cosmic-ray pulse in the 2-ms interval, or a SPE or larger pulse in the 30-μs interval, set the veto flip-flop to "on." The flip-flop remained on throughout the MTW, inhibiting, in the main detector trigger (Fig. 4.8), the logical AND between the counter's signal and the MTW. The veto flip-flop was set to "off" 1 ms before the start of the next MTW. The veto system reduced the noise rate by more than a factor of five, at the cost of an effective deadtime (per counter) of roughly 25%. This was primarily the result of the 30-μs portion of the system.

4.5.5 Trigger for Pulse Height Calibration

A radioactive source (^{241}Am, 1 μCi) was periodically positioned next to the detector (inside the shielding), in order to monitor the detector's response to a known amount

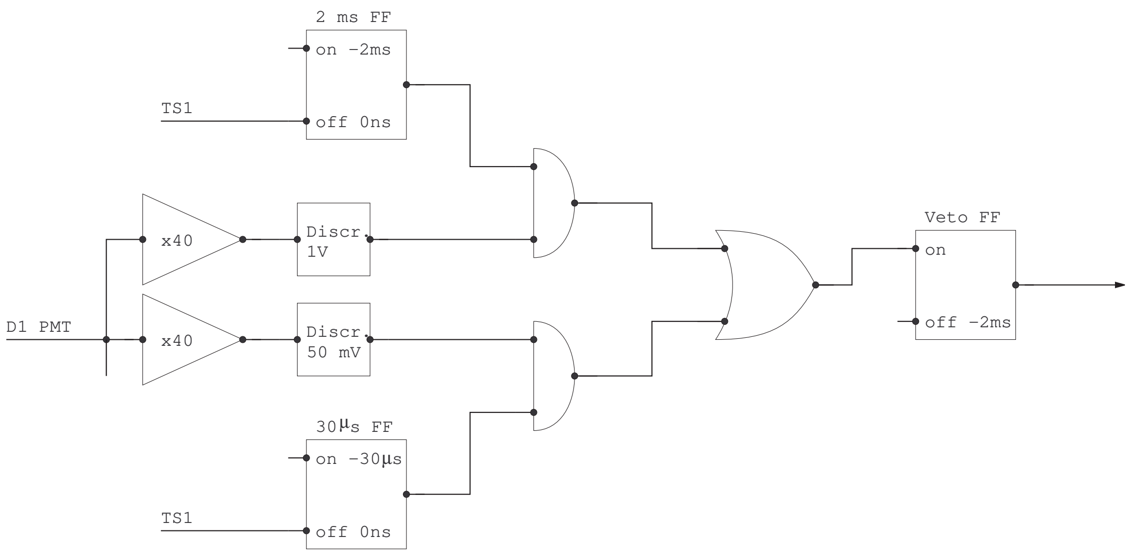

Figure 4.11: Schematic of the veto system.

of deposited energy. Due to the small size of the MTW, collecting this data using the main detector trigger took an inconvenient amount of time. A special trigger (the “source-run” trigger) was set up to allow rapid collection of PMT pulses uncorrelated in time with the MTW. A schematic of this trigger is shown in Figure 4.12. A pulse of SPE size or larger, from any of the four counters, would set the source-run LAM (“LAM 2”), set the busy level, and generate a 500-ns gate for the ADCs. The amplified and unamplified PMT signals were sent to the ADCs after being delayed enough to fall within the 500-ns gate. The computer would then read and clear the ADCs, and turn off the busy level, allowing the process to begin anew. The source-run trigger was activated via a level (the “source-run level”) set to “on” or “off” by the computer.

4.5.6 Toroid Pulse Integrator

Critical to the analysis of the experiment was an accurate measure of the number of electrons that collided with the PPT during data collection. The toroid pulses from

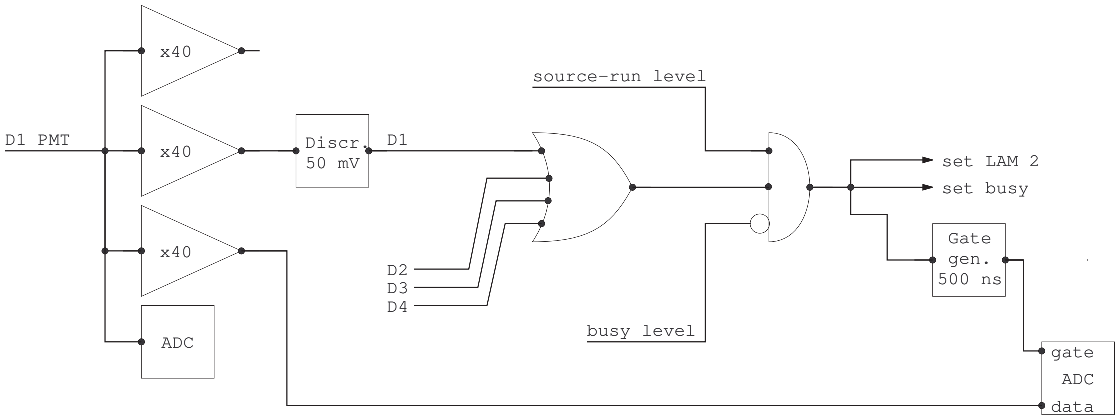

Figure 4.12: Schematic of the "source-run" trigger.

the accelerator had pulse heights proportional to the number of electrons in each PPB bunch, but with an unspecified proportionality constant. While the experiment collected data, a special circuit (the "toroid integrator") measured and summed the heights of the toroid pulses. To calibrate the resulting number, toroid pulse heights were integrated over each of a series of short runs. The number of electrons colliding with the PPT during these runs was estimated from the average PPB-bunch rate and the average PPB-bunch charge recorded in the SLC database over the time interval of the run. The average proportionality constant (from fifteen two-minute runs) was found to be $(9.39 \pm 0.69) \times 10^7$ electrons per toroid-integrator unit. (Difficulty in reliably obtaining the data before its automatic deletion from the SLC database prevented us from using the database's PPB-bunch charge values for the experiment as a whole.)

4.5.7 Data Acquisition System

The computer used for data acquisition was a Commodore Amiga 3000T, with a CAMAC-interface card created at CERN, and a 2-gigabyte data storage capacity. Data from an event consisted of the contents of the ADCs, TDCs and toroid integrator; tags indicating type of LAM, presence of an LED pulse, and identity of the counter that generated the LAM; and the contents of digital scalers recording such things as number of TS1 pulses, number of toroid pulses, number of MTW-coincident PMT pulses from each counter (before and after veto), number of each type of LAM, number of fast-clears, total number of PMT pulses from each counter, etc. (Except for the number of toroid pulses, which was important for the analysis of the experiment, the scaler data served primarily as a means to monitor detector and trigger performance.) A few hundred thousand events would be gathered in runs lasting 12 – 24 hours. After temporary storage on the Amiga, data from each run was sent via Ethernet to SLAC's UNIX-machine cluster, then copied onto magnetic tape. The online software (developed specifically for this experiment) facilitated display of the data during a run, allowing for real-time observation of pulse-height and time spectra.

4.6 Detector Pulse Height Calibration

We assumed a linear relationship (up to the saturation point of the PMT) between energy deposited in the scintillator and the size of the resulting PMT pulse. To determine the proportionality constant, the spectrum of pulse heights from one of the counters (counter D1) was recorded with the radioactive source (^{241}Am) inside the copper box, and the detector under otherwise normal running conditions. Observations of D1 pulses on the oscilloscope confirmed that the PMT was well below saturation. A 5X attenuator was used to bring the amplified signal within the input range of the ADC. The resulting spectrum is shown in Figure 4.13.

Decays of ^{241}Am generate a number of x-rays as well as an α particle. The former were able to penetrate the various layers of plastic between the source and the scintillator. A simulation of the energy lost in the scintillator by the five principal x-rays of ^{241}Am, given the geometry of our setup, was performed using EGS4[70]. This spectrum is given in the top-right diagram of Figure 4.14. The PMT pulse-height distribution that would result from this energy-deposition spectrum, calculated assuming a scintillation efficiency of $1\gamma/100$ eV, a light-collection efficiency of 0.2, a

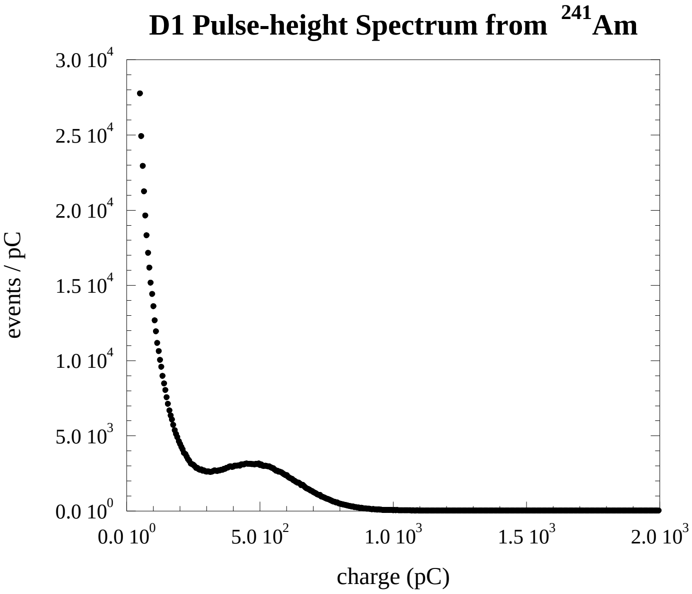

Figure 4.13: Measured pulse-height spectrum of ^{241}Am events.

PMT quantum efficiency of 0.2, and Poisson smearing of the pulse heights, is shown in the bottom diagram in Figure 4.14.

The broad bump in the measured pulse-height spectrum was identified as corresponding to the rightmost bump (entirely due to the 59.5-keV x-ray) in the simulated spectrum. (The large peak on the left side of the simulated spectrum was below ADC pedestal in the measured spectrum, due to the attenuation.) The pulse charge at the center of the measured bump (corrected for attenuation) was 450 ± 13 picoCoulombs (pC). Expressed in terms of the most-probable charge of an SPE pulse ($\langle$SPE$\rangle = 25.8 \pm 1.5$ pC, for counter D1), this was 17.4 ± 1.1 $\langle$SPE$\rangle$. Converting the center of the simulated bump (22.0 ± 1.2 photoelectrons) back to energy units via the three efficiencies mentioned above gives 55.0 ± 3.0 keV. Taking the ratio of output pulse height to input energy with these values, one obtains 0.317 ± 0.026 $\langle$SPE$\rangle$/keV.

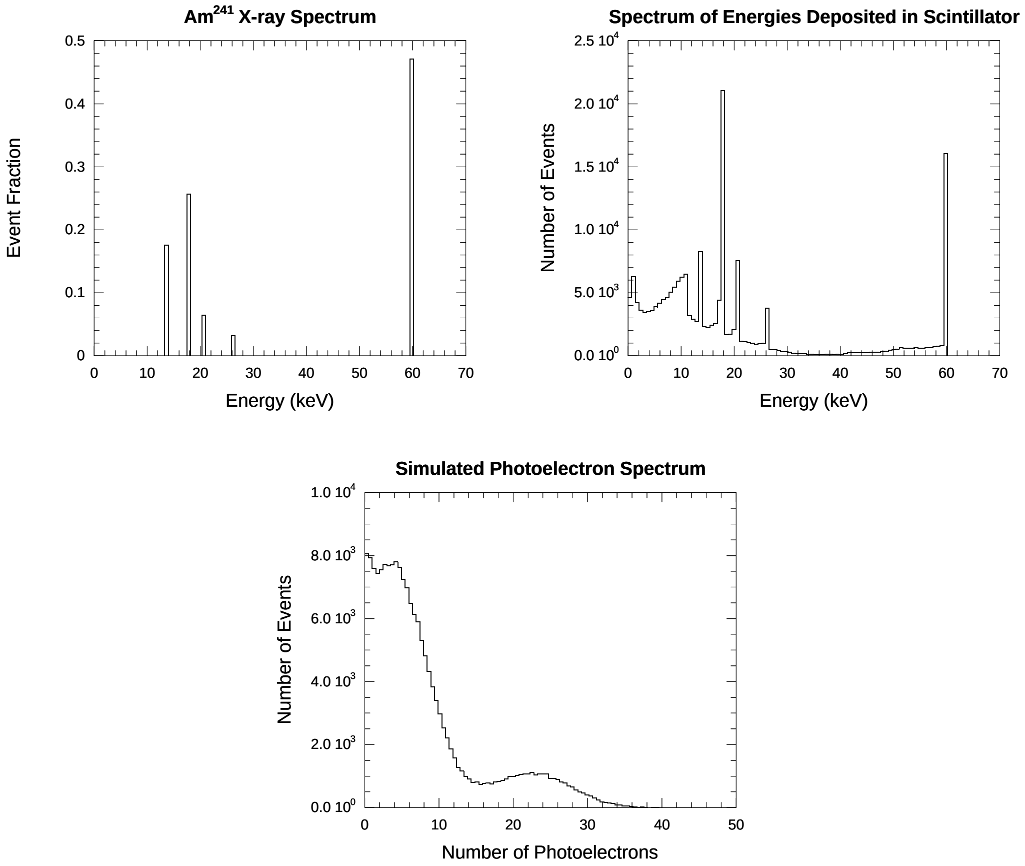

Figure 4.14: Simulated pulse-height spectrum of ^{241}Am events. Upper left plot: the five principal x-rays of ^{241}Am. Upper right plot: the energy deposition spectrum, simulated using EGS4. Lower plot: the simulated pulse-height spectrum (obtained from the energy deposition spectrum by assuming one photon per 100 eV, 20% light-collection efficiency, 20% quantum efficiency, and Poisson smearing of the number of SPE s).

4.7 Time Calibration

MQs from the PPT would arrive at the detector in bunches, at a particular time relative to our main timing reference, TS1. Their signature consists of a peak in the time spectrum of detector pulses. A prediction of the location and width of this peak allows us to focus attention on a portion, rather than the entirety, of the time spectrum, and thus obtain better signal-to-noise.

4.7.1 Expected Shape of Peak in Time Spectrum

Prior to installation of the detector, an experiment was performed to determine the expected shape of the mQ-induced timing peak, using one of the detector's four scintillation counters. The setup is illustrated in Figure 4.15. Over most of the charge-mass parameter space that mQs could occupy, the size of the PMT pulse generated by a typical mQ bunch would be one SPE. (This is discussed in greater detail in chapter 5 section 4.) We wished to ascertain the time spread of SPE-size pulses from the detector. Cosmic-ray muons were used for this purpose. A light filter was placed between the scintillator and the PMT to restrict the number of scintillation photons arriving at the photocathode. The filter was chosen such that, on average, less than one photon reached the PMT per cosmic-ray event. A cosmic-ray telescope consisting of small scintillation counters positioned above and below the main counter served to trigger data collection. Without the filter, the time spectrum of cosmic-ray induced pulses displayed a sharp, narrow peak, 7 ns in width. With the filter in place, the peak widened to about 14 ns (FWHM), and was shifted 16 ns later in time. (These results are shown in Fig. 4.15.) Measurements were made with the telescope at the far end, middle, and near end of the counter. The widening and time shift between filtered and non-filtered peaks were roughly the same in each case, while the positions of the peaks varied in relation to the average distance the scintillation photons had to travel to reach the PMT. In order to simulate the time distribution of SPE pulses induced by mQs (which would travel down the axis of the

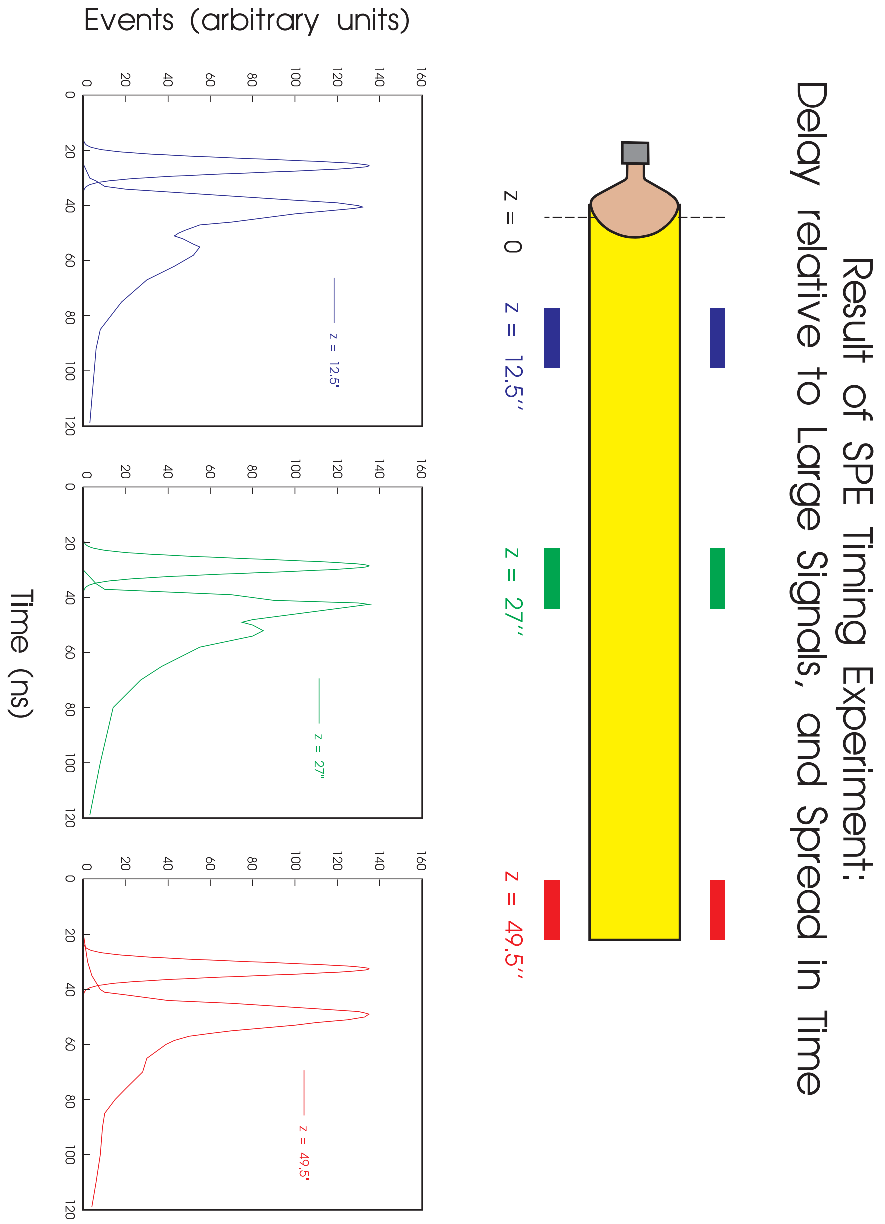

Figure 4.15: Setup and results of the SPE timing experiment. The colors represent different positions of the cosmic-ray telescope. Reflection of photons off the far end of the scintillator accounts for the bimodal shape of the delayed peak.

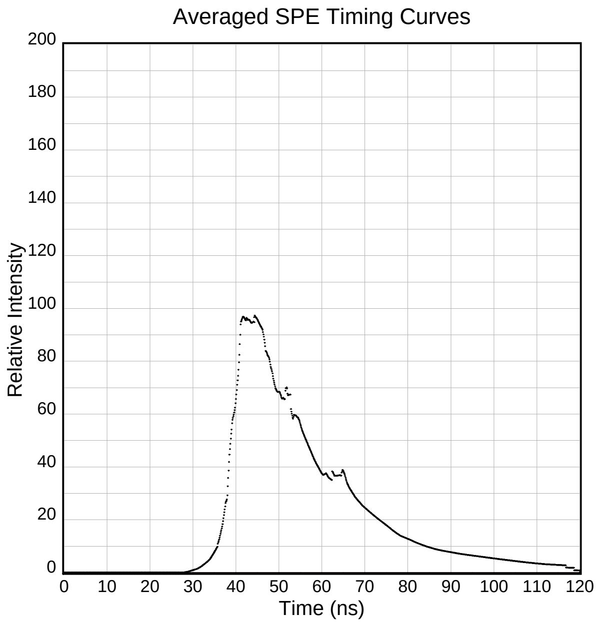

Figure 4.16: Predicted shape of mQ-induced peak in the time spectrum, assuming events of SPE pulse-height.

counter, rather than top-to-bottom), the locations of the measured SPE peaks were adjusted to account for the travel time of a fast ($v = c$) mQ between the far, middle and near end of the counter, then the three time spectra were averaged. The resulting peak, with FWHM of 20 ns, is shown in Figure 4.16.

4.7.2 Expected Position of Peak in Time Spectrum

The time spectrum of events in the muon-counter array upstream of the mQ detector consisted of a sharp peak 60 ns beyond TS1. The time required for a mQ to travel the 27.0 meters between the muon counters and the middle of the mQ detector, at speed c, was 90.0 ns. For a variety of reasons including differences in cable length and PMT type, the response time of the mQ detector was expected to be different from that of a muon counter. This difference could be determined by comparing the time (TDC value) of an event occurring simultaneously in the detector and the muon counters. To this end the muon counters were removed from their normal locations and placed above and below the mQ detector (without replacing their cables), so as to form a cosmic-ray telescope. Coincidences between the upper and lower muon counter triggered collection of data, and a time spectrum of detector events (for each counter in the detector) relative to the lower muon counter was recorded. Differences in time response between the individual muon counters were ascertained by collecting data with the muon counters stacked on top of one another. After adjusting for cosmic-ray time of flight, it was found that an event occurring simultaneously in the central muon counter (M1) and detector counter D1 would appear 21.6 ns earlier in the TDC spectrum of D1. The other three counters (D2, D3 and D4) preceded M1 by 30.4 ns, 32.2 ns, and 28.8 ns, respectively. These values were obtained from events with large pulse height. In order to complete the determination of mQ event time, we added the 16-ns delay of SPE-size events discussed in the previous paragraph. Altogether, the expected locations of the mQ-induced peak in the time spectra of the four counters, relative to TS1, were 144.1 ns, 135.3 ns, 133.5 ns and 136.9 ns.

4.8 Intrinsic Detector Noise

4.8.1 Characteristics of the Noise

Excluding very small pulses (pulse height $< 1/4\ \langle \mathrm{SPE} \rangle$), the vast majority of pulses from the detector were of SPE size. A typical pulse-height spectrum of detector noise is shown in Figure 4.17. The pulses occurred at a rate 2 – 3 orders of magnitude higher than attributable to ambient background radiation. Observation of counter output on an oscilloscope revealed that events with large pulse height (*e.g.* cosmic rays) were invariably followed by a string of several hundred small pulses (SPE size and smaller), whose frequency fell off smoothly with time. (This is in contrast to events due to typical afterpulsing in PMTs, which generally have a larger-than-SPE pulse height, and occur with a specific delay relative to the initiating event.) The

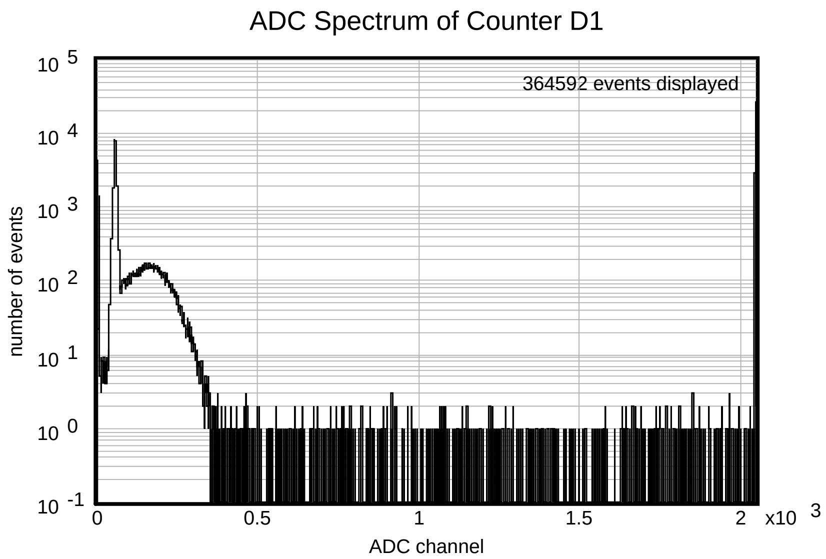

Figure 4.17: Typical pulse-height spectrum from the detector.

time necessary for the noise rate to return to normal following a large pulse ranged from milliseconds to seconds. (Flashes of light from a blue LED also produced this effect, while the effect from green and red LEDs was less pronounced.) In addition to excess noise following large events, dense clusters of small events, lasting tens of microseconds, were observed. (These clusters contained the vast majority of SPE-size events.) A rough measure of the rate at which noise clusters occurred was obtained by extending the output width of discriminated pulses to 30 μs and recording the discriminated pulse rate. At 5^o C, this "cluster rate" was 4.0 kHz per counter, while the single-pulse ("singles") rate was 30 kHz.

The origin of the 'afterpulsing' and the noise clusters is not well understood. Both phenomena were observed in a small prototype detector (consisting of a 20-cm cube of Bicron BC 408 scintillator, a 10-cm lightguide of the same material and a Thorn EMI model 9353 KA PMT, optically coupled with Bicron BC 630 silicone grease and wrapped in aluminum foil), as well as the main detector and, to a lesser extent, the individual PMTs. The plastic scintillator was found to luminesce with a very long time constant ($\sim$ 1 minute) following exposure to long-wavelength ultraviolet light, suggesting that some of the noise pulses might represent delayed release of energy stored in the scintillator.

However, other tests suggest that much of the noise might originate in the PMTs. Exposure of a lone PMT to pulsed LED light (of saturation-inducing brightness, at a pulse rate of 390 Hz, for 15 seconds) resulted in a noise rate, post-exposure, that was 200 times higher than normal. (Lower LED brightness, or lower pulse rate, produced a less dramatic effect.) The elevated rate returned to normal with a time constant of 1.2 minutes. With the LED pulsed at 35 Hz, a pulse-height spectrum was gathered in such a way that PMT pulses occurring within 2.5 ms of the LED were excluded. Comparison of this spectrum with one taken in the absence of LED pulses revealed that the rate of occurrence of large ($>$ 1 SPE) PMT pulses was about the same in both cases, while the SPE-pulse rate was three times higher in the spectrum influenced by the LED. This suggests that stimulation of large PMT pulses results in an increase in the rate of SPE-size dark noise. A second test lends support to this hypothesis. Use of a magnetic field to inhibit electron multiplication in the PMT during bright LED flashes reduced the SPE-noise rate, measured a few milliseconds after each flash, by 50% compared to that recorded with no magnetic field present during the flash. With continuous scintillator light (induced by a ^{60}Co radioactive source) replacing the LED, a similar reduction in SPE noise was observed.

An unexpected behavior observed in both the prototype and detector counters is worth mentioning. It is generally assumed that the dark-noise rate in PMTs falls monotonically with decreasing temperature. This was true of our counters within the temperature range 20^o C to about 5^o C. Below 5^o C, however, the noise rate increased with decreasing temperature. In the prototype, the rate rose by 40% between 5^o C and -20^o C, while in the detector counters, the rate increased by 50%. (The PMTs by themselves exhibited a smooth decrease in noise rate, by a factor of 8, between 20^o C and -30^o C.) The relationship between temperature and noise was the same regardless of whether the counters were being cooled or warmed, and was stable over a time period of several days. The rate at which noise clusters occurred in the prototype counter was seen to decrease by 33% on one occasion, and increased by 24%

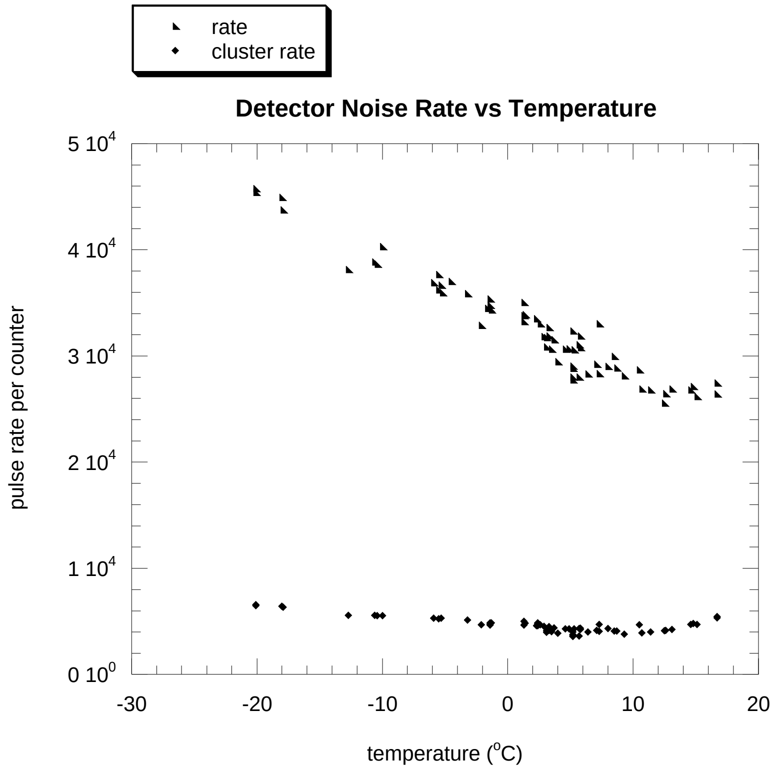

Figure 4.18: Plot of detector noise rate versus temperature.

on another, when cooling from 5° C to −20° C. In the detector counters, the cluster rate consistently rose by 60% between 5° C and −20° C. Figure 4.18 shows a plot of detector noise rates (singles and clusters) versus temperature over the range 17° C to −20° C. Some of the observations mentioned in this section have been discussed also by T. Marvin[79].

4.8.2 Noise Abatement Measures

The principal measures we used to minimize noise were as follows: enclosure of the detector in a copper box; insertion of low-pass filters in the high-voltage and thermistor lines; chilling the detector to 5° C; running the PMTs at a lower than typical voltage, with cathodes grounded; shielding the detector with 10 cm of lead; and employing the afterpulse-veto system described above. The copper box and low-pass filters minimized exposure of the detector to RF backgrounds. Chilling the detector from room temperature to 5^o C actually increased the noise rate by 10%, while reducing the cluster rate ($\cong$ noise rate after veto) by 30%. Running the PMTs at lower than typical voltage ($\sim$ 1000 V rather than $\sim$ 1500 V) reduced the incidence of sudden, large (one to two orders of magnitude) jumps in PMT noise rate. Shielding the detector with 10 cm of lead provided a 100-fold decrease in the flux of gamma rays from radioactive decay. In the prototype counter, the resulting noise-rate reduction was a factor of 3.6, and the reduction in cluster rate was 40%. The afterpulse-veto system, inhibiting data collection on any PPB that was preceded, within 2 ms, by a large pulse from the detector, or within 30 μs by a detector pulse of any size, reduced the background rate by more than a factor of five, at the cost of rendering the detector insensitive to 25% of PPB s.

Chapter 5

Analysis

5.1 Introduction

The experiment sought to detect mQs via the excitation and ionization left behind by a passing relativistic mQ. Electron bunches colliding with the positron-production target (PPT) would generate mQ bunches that were narrow in angle and highly relativistic. These mQ bunches would have a time spread on order of a nanosecond upon arrival at the detector. The presence of mQs would be most readily apparent by a peak in the time spectrum of detector pulses, occurring at the expected arrival time of the mQ bunches.

This chapter will discuss the types and quantity of data collected, the means by which detector performance (including deadtime) was monitored, our prediction of the expected number of mQ events as a function of mQ charge and mass, and our (fairly simple) statistical analysis of the data, leading to an upper limit on the possible value of mQ charge.

5.2 Type and Quantity of Data Collected

The experiment collected data representing the collisions of $(3.35 \pm 0.01) \times 10^8$ electron bunches with the positron-production target (PPT). These 'positron-production' bunches (PPB s) contained an average of $(3.17 \pm 0.25) \times 10^{10}$ electrons each, at an electron energy of 29.47 GeV. Each of the four counters in the detector lost approximately $(21 \pm 1)\%$ of PPB s to deadtime, primarily as a result of the afterpulse-veto system. (In general the dead periods of each counter did not overlap with those of the others.) The data was collected during 55 runs, lasting roughly 24 hours each, over the course of 14 weeks beginning in December 1994.

The data consists of the time and pulse height of photomultiplier-tube (PMT) pulses occurring within the 250-ns "main timing window" (MTW) surrounding the expected arrival time of mQ bunches at the detector. (An MTW was generated every time the TS1 time marker was received from the linac, roughly 120 times per second.) The presence or absence of an electron bunch at the PPT (as indicated by a pulse from the upstream toroid) in conjunction with each event was recorded, in order to separate a set of events which could only be due to background noise. Since PPB production was generally sporadic, this allowed for essentially simultaneous collection of background and real data. Additional items recorded were the total number of TS1 time markers, the total number of pulses ignored (for each counter) due to the afterpulse-veto system, and the identity of events coinciding with trigger pulses sent to the LEDs on the scintillator (these LEDs were triggered once every thousand TS1s in order to monitor detector performance). In addition to the background mentioned above, a second type was obtained, consisting of events recorded while the detector was positioned one meter to the side of the axis of the PPB beam. Since mQs of all but the highest masses are expected to be very forward directed, the detector would miss most of the mQ beam, allowing for a measurement of possible PPB-related backgrounds (*e.g.,* neutrino interactions near the scintillator).

5.2.1 Spectra of Measured Backgrounds

Representative spectra from the two types of background data are shown in Figures 5.1 and 5.2. The large peaks centered at 50 ns and 212 ns in the time spectra are due to the LEDs, and disappear when events concurrent with LED trigger pulses are removed from the data. The remaining events are fairly uniformly distributed in time. The LEDs are responsible for the large peak at 2×10^3 pC in the pulse-height spectrum. The leftmost peak (at 13 pC) is the pedestal of the ADC, and the small peak on the far right, at 10^4 pC, is due to cosmic ray muons. The broad peak centered at 38 pC represents events of single-photoelectron (SPE) size, primarily dark noise from the PMT. With the exception of the width of the LED-induced peak, the shapes of the spectra do not differ much between the two types of background. PPB-related backgrounds (with the possible exception of extremely forward-directed particles) are evidently not readily discernible by this experiment. The overlapping peak (shown in blue) at the bottom of Figure 5.2 is an artificially generated pulse-height spectrum consisting entirely of SPE events. Comparing the areas under the SPE and background-data curves, we find that SPEs account for roughly 94% of all non-LED background events with pulse height above the ADC pedestal.

5.3 Stability of Detector Performance

The LED-generated events, together with spectra (gathered after every 1-2 runs) of events induced by the ^{241}Am source, provide a means to monitor changes in the response time, time resolution, sensitivity to deposited energy, and deadtime of the detector and its accompanying electronics over the course of the experiment. (A drift in response time or a reduction in sensitivity could easily obscure the anticipated mQ signal.)

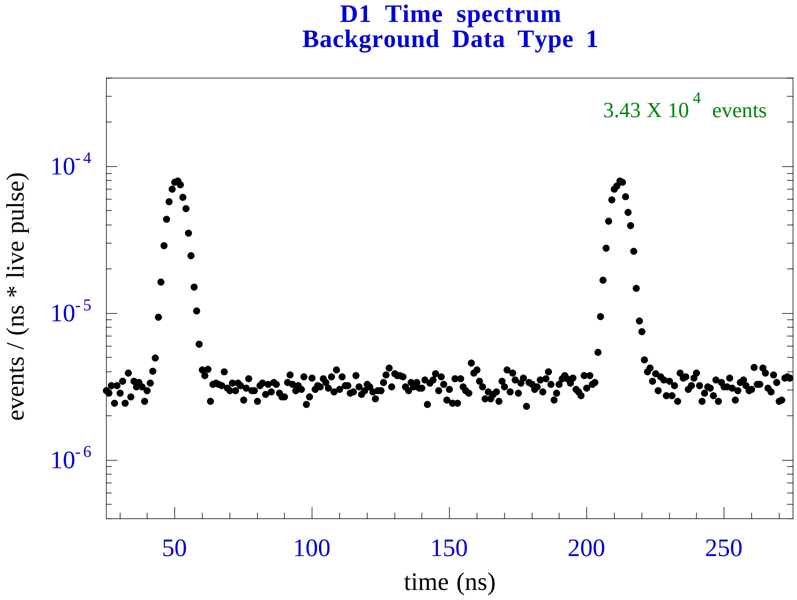

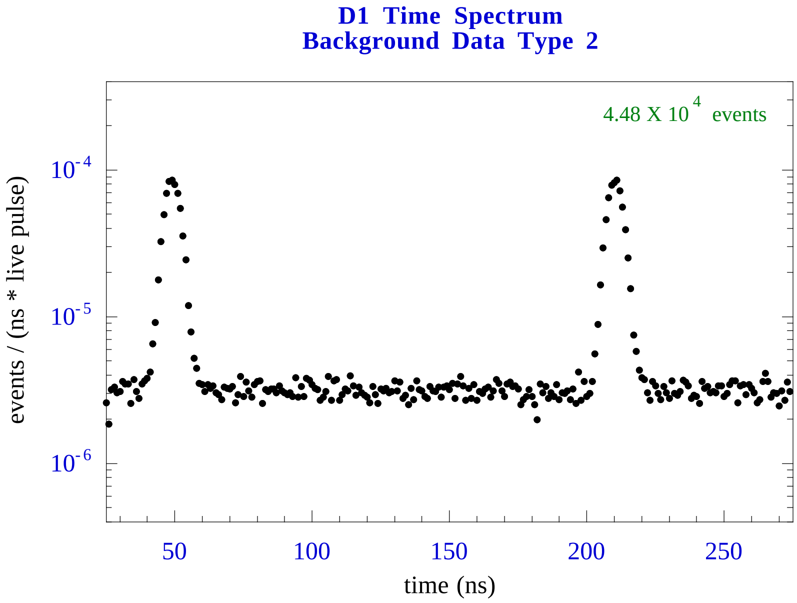

Figure 5.1: Time spectra of background events. Upper plot: events with no PPB present. Lower plot: events recorded while the detector was not aligned with the beam.

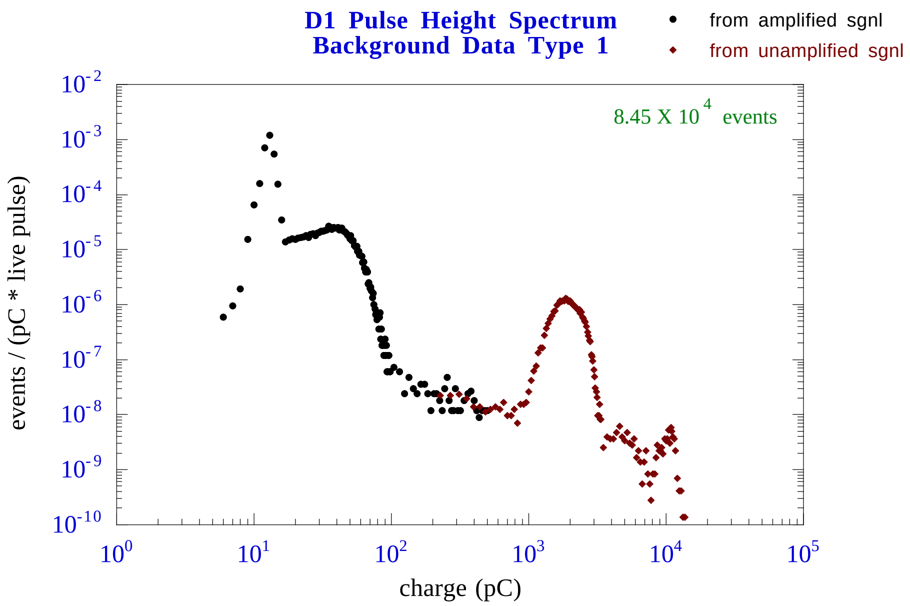

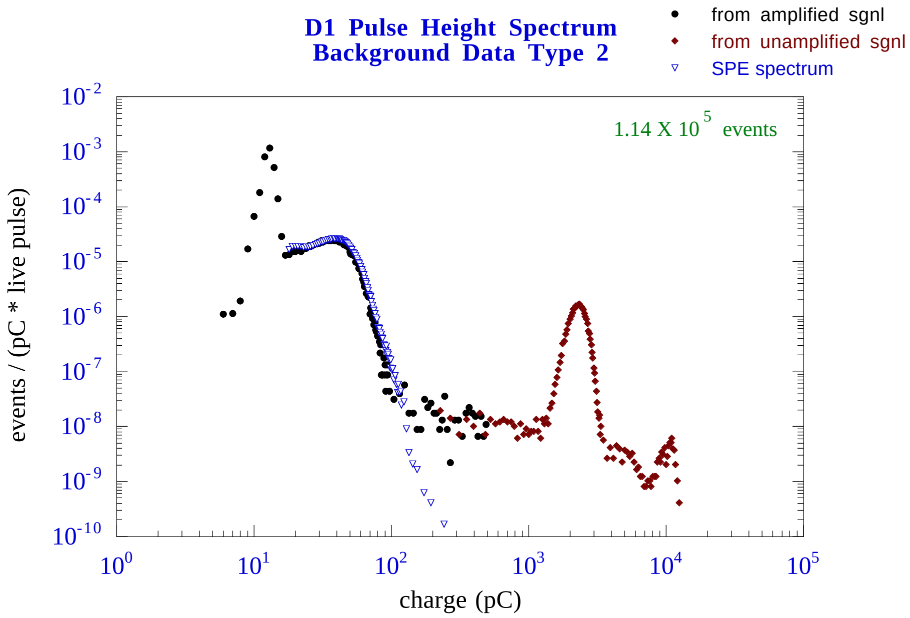

Figure 5.2: Pulse-height spectra of background events. Upper plot: events with no PPB present. Lower plot: events recorded while the detector was not aligned with the beam. The blue curve in the lower plot is a spectrum (generated via LED) of SPE events.

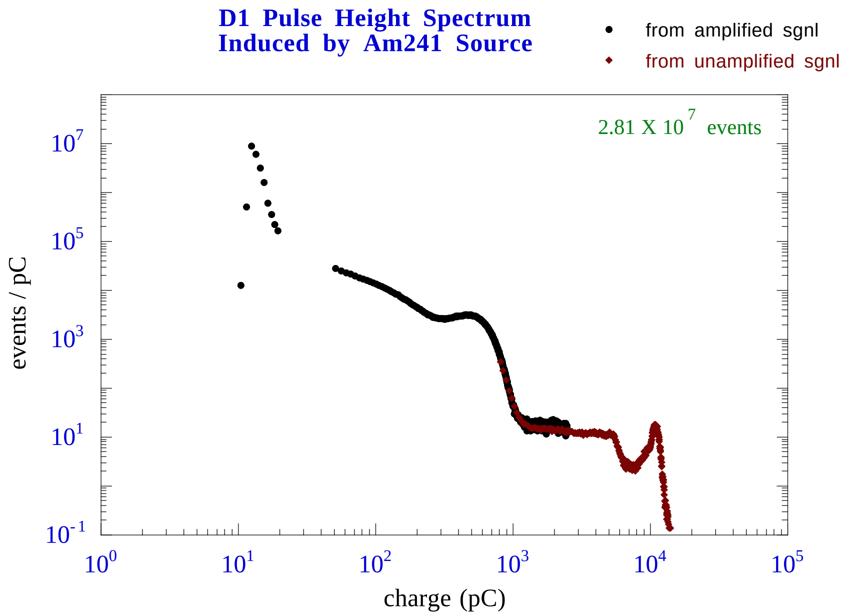

Figure 5.3: Pulse-height spectrum generated by ^{241}Am.

5.3.1 Energy Sensitivity and Resolution

Figure 5.3 shows the pulse-height spectrum due to ^{241}Am, obtained from one of the four counters in the detector (counter D1). Based on an EGS4[70] simulation of the energy deposited in the scintillator by this source (shown in Figure 5.4), the peak at 467 pC ($\cong$ 17 photoelectrons) in the pulse-height spectrum is identified as being due to absorption of the 60 keV x-ray of ^{241}Am. For each of the four counters, the location and width of this peak was obtained from each of 75 ^{241}Am spectra recorded over the course of data collection. Plots of peak position and width versus time were made in order to check for any drift in counter sensitivity. Based on these plots we conclude that, at 60 keV, energy sensitivity had a drift of no more than 3% and a scatter of roughly 2.4%, while energy resolution (a somewhat less important quantity) had a drift of less than 9% and a scatter of about 9% . The plot of peak position versus time is shown in Figure 5.5, and a histogram of the peak positions is given in Figure 5.6.

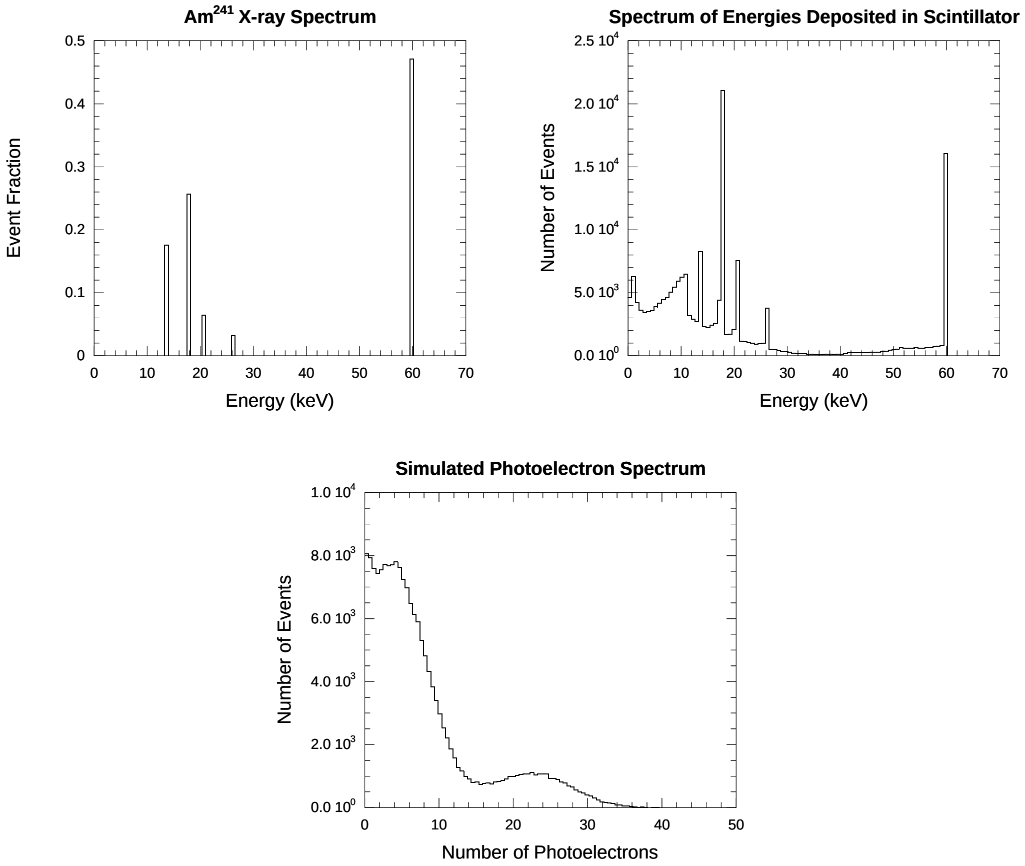

Figure 5.4: Simulated pulse-height spectrum of ^{241}Am events. Upper left plot: the five principal x-rays of ^{241}Am. Upper right plot: the energy deposition spectrum, simulated using EGS4. Lower plot: the simulated pulse-height spectrum (obtained from the energy deposition spectrum by assuming one photon per 100 eV, 20% light-collection efficiency, 20% quantum efficiency, and Poisson smearing of the number of SPE s).

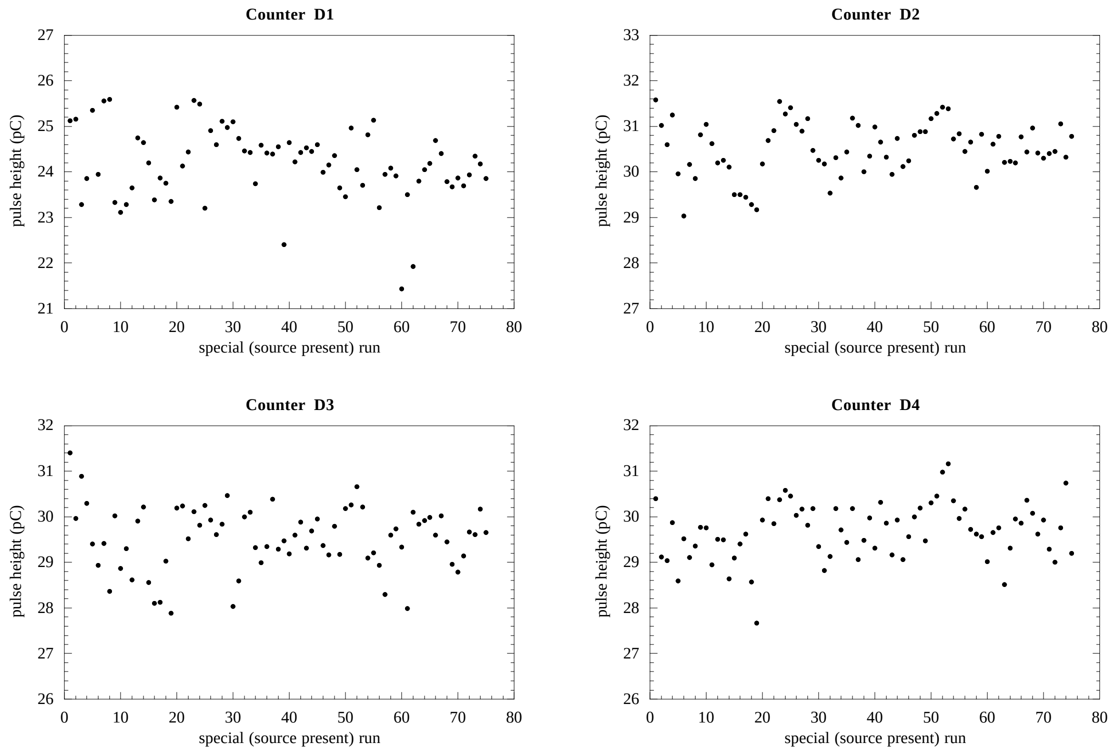

Figure 5.5: Positions of the peak induced by ^{241}Am in the pulse-height spectrum, recorded over the course of the experiment (for monitoring detector performance).

5.3.2 Response Time and Time Resolution

Figure 5.1, discussed above, shows time-spectrum peaks generated by the LEDs. The amount of light from the LEDs was sufficient to saturate the PMTs, resulting in events with large pulse heights. For every (non-background) data-gathering run, fits of the two LED peaks were performed using a gaussian fitting function, and the positions and widths (standard deviations) of the gaussians were recorded. The plot of peak position versus run number for the earlier peak is shown in Figure 5.7. (The results for the later peak are similar.) Figure 5.8 gives a histogram of these peak positions. With the exception of counter D1, which made a temporary excursion to a 5-ns longer response time between runs 38 and 48, the drift in response time of each counter (for events of large pulse height) was below 1.5 ns, and the average scatter in response

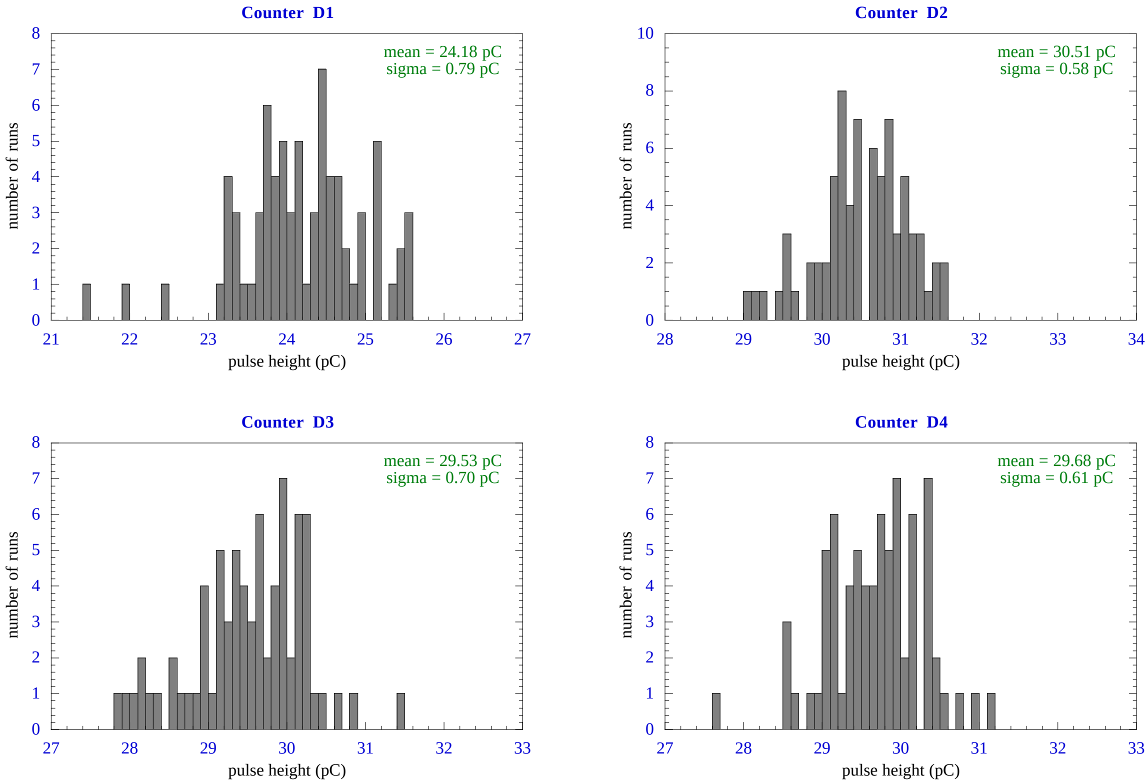

Figure 5.6: Histograms of the ^{241}Am-peak positions recorded over the course of the experiment (for monitoring detector performance).

time (including counter D1) was 0.6 ns. A very rough measure of the time resolution of the detector is given by the widths of the LED peaks. For events with large pulse height, the drift in time resolution was less than 0.3 ns for each of the four counters, and the average scatter in time resolution was 0.19 ns.

5.3.3 Deadtime

The LEDs also provide a means to check the deadtime of the system consisting of the detector, electronics and data-acquisition computer combined. The number of TS1 time-marker pulses, synchronized to the passage of electron bunches in the linac but active even in the absence of bunches, was recorded during every run. The LEDs were

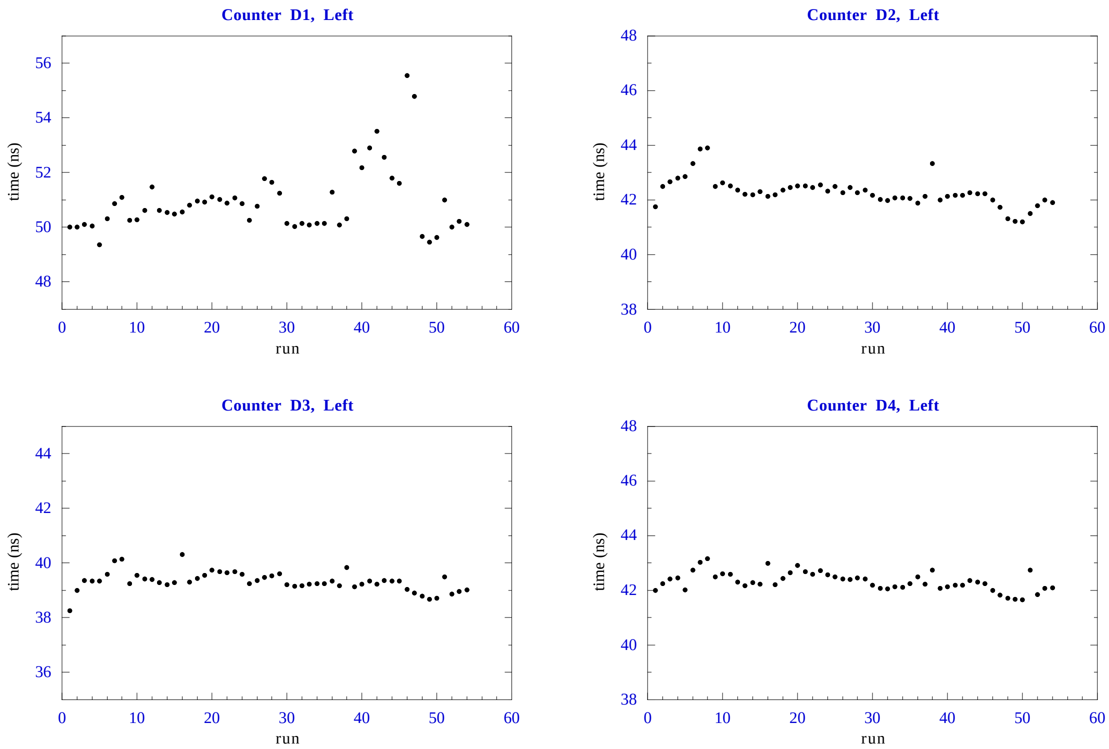

Figure 5.7: Positions of the peak induced by the LED in the time spectrum, recorded over the course of the experiment (for monitoring detector performance).

triggered once every thousand TS1 pulses, regardless of the status of the rest of the system. Any discrepancy between the number of trigger pulses sent to the LEDs ($= N_{\mathrm{TS1}}/1000$) and the number of LED events actually detected during the run (N_{LED}) represents the amount of time the system was, for any reason, unresponsive. Since there is almost no background in the region of the pulse-height spectrum occupied by the LED peak (see Figure 5.2), the value of N_{LED} was taken to be equal to the number of events in this peak. The deadtime fraction, $(N_{\mathrm{TS1}} - 1000N_{\mathrm{LED}})/N_{\mathrm{TS1}}$, averaged over the four counters for 54 of the 55 runs, was found to be 0.198 ± 0.006. (Runs showing an unusual amount of deadtime were excluded from the final data set.)

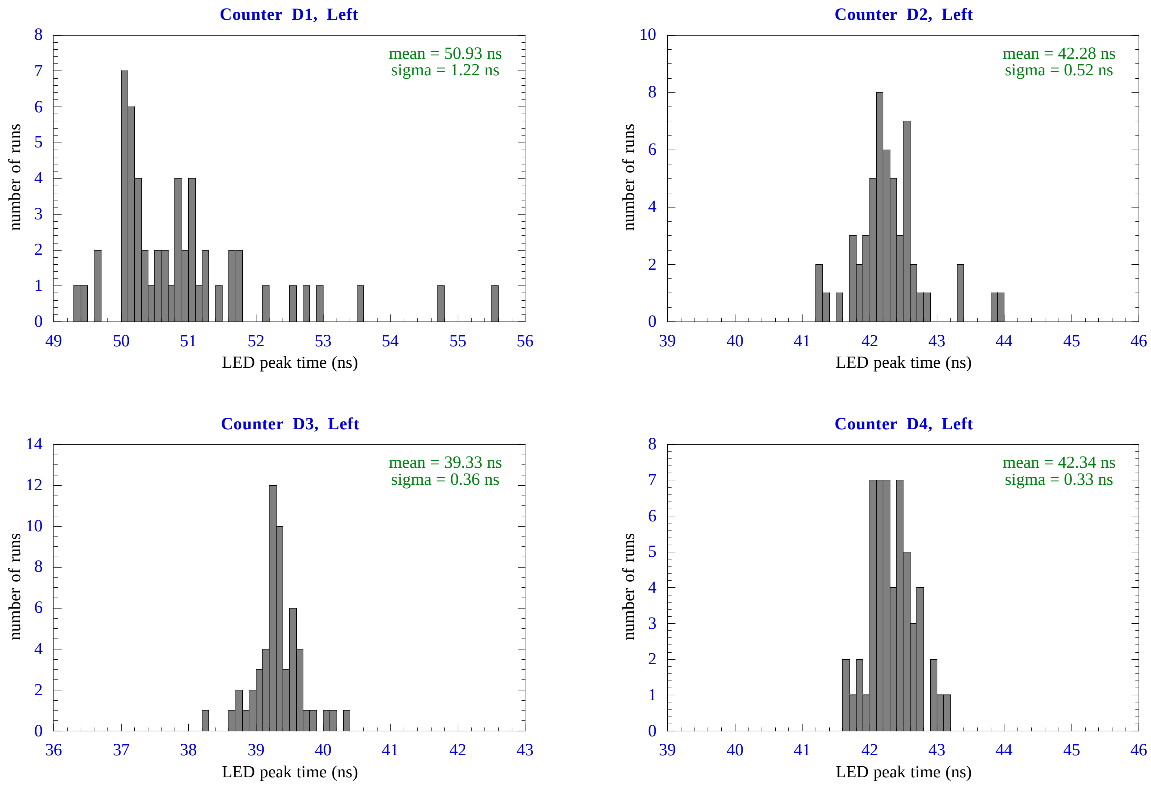

Figure 5.8: Histograms of the LED-peak positions recorded over the course of the experiment (for monitoring detector performance).

5.4 Predicted Number of mQ Events

The most distinct evidence for mQs would be a fairly narrow (20-ns FWHM) peak at a well-defined location in the time spectrum. The pulse-height spectrum would also exhibit a peak, but a less narrow one that could, if occurring in the SPE region, be obscured by the large number of SPE background events. The location of a time-spectrum peak due to mQs should be independent of mQ charge and mass, whereas the size of the peak should depend on both these quantities. Our method for predicting the location of the time-spectrum peak was discussed in chapter 4 section 6. The discussion below concerns the expected size of the peak, which has direct bearing on the charge values that can be excluded by a null result of the experiment.

We define the number of expected events to be the number of mQ-induced PMT pulses that *a)* occurred during the live time of the experiment, *b)* were above discriminator threshold, and *c)* fell within a specific time window of 40-ns length (within the main timing window) deemed most likely to contain a mQ signal. (Selection of this signal window is discussed in section 5 below.) Let the number of expected mQ events be denoted by N, and let S denote the average size, in photoelectrons (PE s) of a mQ-induced PMT pulse.

5.4.1 Prediction of N and S

To compute an estimate of N, two things need to be considered: the rate at which mQs enter the counters (specifically, whether they enter on every PPB, or only on some fraction of PPB s), and the average size of PMT pulse generated when they do enter (specifically, multiple PE s, occurring every time mQs enter, or a single PE, occurring less frequently). The former can be parameterized via the following quantity, which represents the average number of mQs entering a single counter per PPB:

$$F = Q^2 \, n \sum_{i,j} (\mathbb{M}_{ij} \mathbf{A}_j) \tag{5.1}$$

where Q is the mQ charge in units of e; n is the average number of electrons in a PPB; $\mathbb{M}$ is the matrix generated by the mQ production simulation (see the appendix) such that the entries of $Q^2 \, \mathbb{M}$ are the number of mQs produced, per electron, within a given bin of mQ momentum (rows) and angle (columns); and $\mathbf{A}$ is the fraction of mQs within the acceptance of the counter, for each angle bin. The latter item (the PMT pulse size S) can be parameterized as

$$S = \max(1, \mathcal{S}) \tag{5.2}$$

$$\mathcal{S} = \begin{cases} Q^4 \, n \, C \sum_{i,j} (\mathbb{M}_{ij} \mathbf{A}_j \mathbf{E}_i) \,, & \text{if } F > 1; \\ \frac{1}{F} \, Q^4 \, n \, C \sum_{i,j} (\mathbb{M}_{ij} \mathbf{A}_j \mathbf{E}_i) \,, & \text{if } F < 1. \end{cases} \tag{5.3}$$

where C is the counter calibration in PE s per keV, and $Q^2\,\mathbf{E}$ is the energy deposited in the scintillator by a passing mQ for each bin of mQ momentum. (The quantity $Q^2\, n \sum_j (\mathbb{M}_{ij}\mathbf{A}_j)$ represents the number of mQs entering the counter, per PPB, for a given momentum bin, while the quantity $Q^2 C\,\mathbf{E}_i$ is the average PMT pulse size resulting from traversal by a single mQ of the given momentum. $\mathcal{S}$ is therefore the average number of PE s per PPB, restricted to those PPB s for which at least one mQ enters the counter. Note that $\mathcal{S}$ will be less than one in the case of mQ bunches depositing less energy, on average, than is necessary to produce an SPE.) This parameterization does not take into account saturation of the PMT. There are four combinations of F and S that need to be considered separately in obtaining an estimate of N.

1. $F > 1$ (mQs enter the counter on every PPB)
   $S > 1$ (when mQs enter, a PMT pulse of greater than SPE size is generated)
   A negligible number of PMT pulses are expected to fall below discriminator threshold or outside of the signal window when $S > 1$. The estimation of N is straightforward:

   $$N = 4PL \tag{5.4}$$

   where P is the number of PPB s recorded during collection of the main data set, L is the fraction of PPB s for which the counter was live, and the factor of four accounts for the total number of counters. (Over the range of masses for which mQ production was simulated, regardless of F and S, the angular spread of mQs is much larger than a counter diameter.)

2. $F > 1$ (mQs enter the counter on every PPB)
   $S = 1$ (not every mQ bunch results in a PMT pulse)
   In this case, PMT pulses induced by mQs are of SPE size, and $\mathcal{S}$ represents the probability that a mQ bunch entering the counter produces a PMT pulse. Some pulses are expected to fall below discriminator threshold, or outside the signal window.

   $$N = 4PL\,\mathcal{S}\,d\,w \tag{5.5}$$

   where d is the fraction of SPE-size PMT pulses above discriminator threshold, and w

is the fraction occurring within the signal window.

3. $F < 1$ (a mQ enters the counter on only some fraction of PPB s)
   $S > 1$ (a larger-than-SPE size PMT pulse is generated when a mQ enters)
   Here F represents the probability, per PPB, for a mQ to enter the counter.

$$N = 4PLF \tag{5.6}$$

4. $F < 1$ (a mQ enters the counter on only some fraction of PPB s)
   $S = 1$ (not every mQ that enters results in a PMT pulse)
   F is the probability per PPB for a mQ to enter, and $\mathcal{S}$ is the probability that an entering mQ generates a PMT pulse. The resulting pulses are of SPE size.

$$N = 4PLF\,\mathcal{S}\,d\,w \tag{5.7}$$

A complicating factor thus far neglected is the average separation, at the location of the detector, of the positive and negative member of each mQ pair produced in the PPT. For masses below about 0.4 MeV/c^2, this will be smaller than a counter diameter, so mQs would tend to enter a given counter in pairs rather than singly. In this case the quantities of interest for predicting S and N are the number of pairs entering a counter per PPB:

$$\widetilde{F} = \frac{1}{2}F, \tag{5.8}$$

and the PMT response averaged over those PPB s for which at least one pair enters:

$$\widetilde{\mathcal{S}} = \begin{cases} \mathcal{S}, & \text{if } \widetilde{F} > 1; \\ 2\mathcal{S}, & \text{if } \widetilde{F} < 1. \end{cases} \tag{5.9}$$

S is given by

$$S = \max(1, \widetilde{\mathcal{S}}), \tag{5.10}$$

and N is given by the formulas above with F and $\mathbb{S}$ replaced by $\widetilde{F}$ and $\widetilde{\mathbb{S}}$. The result simplifies to the following:

$$N = \begin{cases} 4PL, & \text{if } (\widetilde{F} > 1,\ S > 1); \\ 4PL\,\mathbb{S}\,d\,w, & \text{if } (\widetilde{F} > 1,\ S = 1); \\ 2PLF, & \text{if } (\widetilde{F} < 1,\ S > 1); \\ 4PLF\,\mathbb{S}\,d\,w, & \text{if } (\widetilde{F} < 1,\ S = 1). \end{cases} \tag{5.11}$$

which differs from the original set of formulas only for the case $(\widetilde{F} < 1,\ S > 1)$. Here we have made the assumption that the separation between the positive and negative mQ, at the location of the detector, remains larger than a typical molecular diameter (a few angstroms) for all values of mQ mass. If this proves to be incorrect below some value ($\ll m_{\mathrm{e}}$), then a mQ pair would resemble an uncharged particle and fail to induce ionization in the scintillator.

Quantities that appear in the formulas for N and S

Values for P, L, F, $\mathbb{S}$, d and w were obtained as follows.

P (the number of PPB s)

was taken to be the number of voltage pulses recorded from the toroid (located just upstream of the PPT) during collection of the main data set.

$$P = (3.352 \pm 0.010) \times 10^{8} \tag{5.12}$$

L (the live-time fraction of a counter)

was estimated as the fraction of PPB s occurring while a given counter was *not* inactivated by the afterpulse-veto system, averaged over the four counters.

$$L = 0.7882 \pm 0.0021 \tag{5.13}$$

F (the average number of mQs entering the counter per PPB)

was derived from $\mathbb{M}$, n and $\mathbf{A}$ of Eq. 5.1. Estimation of $\mathbb{M}$ was discussed in chapter 3 section 2, and in the appendix. Values for n and $\mathbf{A}$ were obtained as follows.

n (the average number of electrons in a PPB)

was taken to be the total number of electrons passing through the toroid during collection of the main data set, divided by P. For 45 of the 55 runs, the number of electrons was obtained by summing the amplitudes of voltage pulses from the toroid, as described in chapter 4 section 4.6. For the remaining 10 runs an electronics failure necessitated that the number of electrons be estimated from the number of events in the muon counters. (The number of muon events in a run had previously been found to have a linear relationship to the sum of toroid pulses.) Combining the measured and estimated data, we arrive at

$$n = (3.17 \pm 0.25) \times 10^{10}. \tag{5.14}$$

$\mathbf{A}$ (the fraction of mQs within the counter's acceptance, for each of the mQ angle bins in $\mathbb{M}$)

is derived from the following four quantities: the detector's location relative to the PPT (determined via geographic survey), the detector's ideal location (defined via projection of the axis of the beam of muons produced in the PPT, and estimated to be 2.2 cm laterally offset from the detector's actual location), the jitter in the angle of the PPB beam relative to its nominal axis (0.6 ± 0.6 mr), and the size of the annulus describing the perpendicular cross section of each bin in mQ angle at the detector's distance from the PPT.

Table 5.1: Acceptance Fraction versus Angle

i	0	1	2	3	4	5	6	7
θ (mr)	0.25	0.75	1.25	1.75	2.25	2.75	3.25	3.75
$\mathbf{A}_i$	1.0	1.0	0.94	0.68	0.39	0.12	~ 0	~ 0

$\mathcal{S}$ (the PMT response averaged over those PPBs for which at least one mQ enters the counter)

was derived from the energy deposited in the scintillator by a passing mQ (for each bin of mQ momentum), the detector's calibration C as computed in chapter 4 section 5 ($C = 0.317 \pm 0.030\,\mathrm{PE/keV}$), and the values of n, $\mathbb{M}$ and $\mathbf{A}$ given above. The energy deposited by a mQ was obtained from the Bethe-Bloch formula[71], with density effect adjusted appropriately in the case of very high γ (low mass) mQs[80].

d (the fraction of SPE-size PMT pulses above discriminator threshold)

was estimated from a pulse-height spectrum (from counter D1) comprised almost entirely of SPE-size pulses (shown in the upper left plot in Figure 5.9), generated by an LED. The LED was triggered by voltage spikes sufficiently small that only 1 in 20 spikes resulted in a PMT pulse above discriminator threshold (which was set at 50 mV, roughly 1/3 the size of the smallest PMT pulses observed on the oscilloscope). The discriminator-threshold cutoff is clearly visible at 20 pC in the figure. Triggering on every voltage spike sent to the LED failed to reveal the shape of the spectrum below discriminator threshold, due to a large amount of spillover from the pedestal of the ADC, so the shape was extrapolated three ways as shown in Figure 5.9. The value of d was taken to be the average, over the three extrapolations, of the number of events above 20 pC divided by the total number of (non-pedestal) events.

$$d = 0.88 \ +0.11 \ -0.14. \tag{5.15}$$

w (the fraction of mQ-induced PMT pulses occurring within the signal window)

was taken to be the portion of the predicted time-spectrum peak (shown in Figure 5.10) contained within the signal window.

$$w = 0.86 \ +0.00 \ -0.10. \tag{5.16}$$

Results for N and S

The regions of charge-mass parameter space spanned by the F–S and $\widetilde{F}$–S combinations enumerated above are shown in Figure 5.11. In certain neighboring regions the various formulas for N (and those for S) coincide. The parameter space can

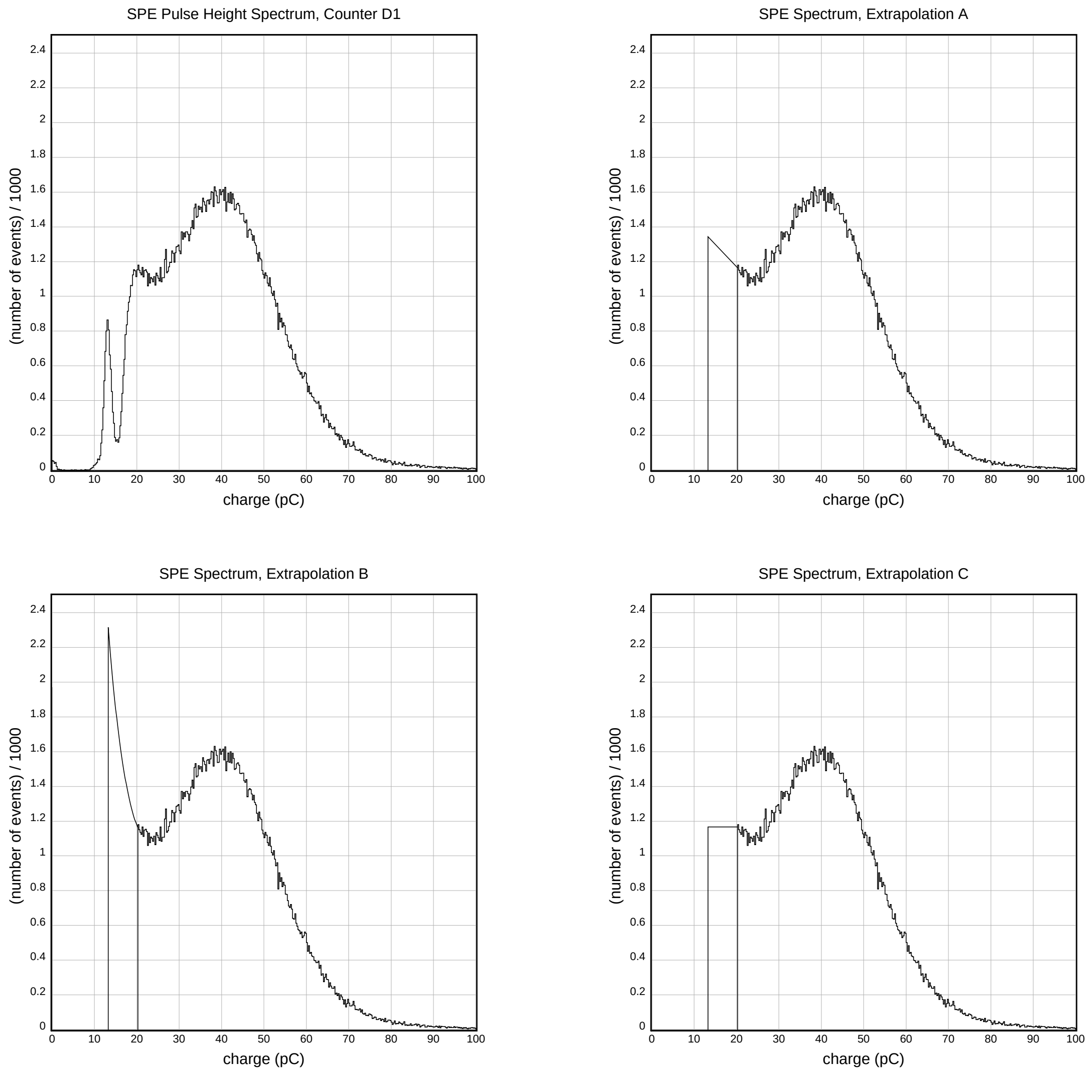

Figure 5.9: Pulse-height spectrum of SPE events. Upper left: the measured spectrum, cut off below 20 pC by the discriminator threshold. Upper right: linear extrapolation down to pedestal position. Lower left: exponential extrapolation. Lower right: constant extrapolation.

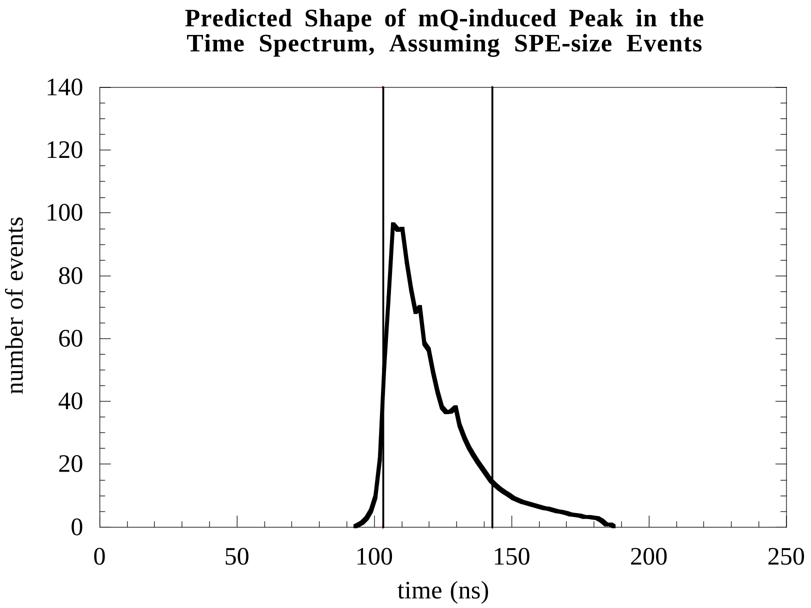

Figure 5.10: Predicted shape of the mQ-induced peak in the time spectrum, together with the signal window.

be divided into three areas corresponding to distinct formulas for S and N. These are shown in Figure 5.11 d. The resulting values of N and S, given in the form of contour plots, are shown in Figures 5.12 and 5.13. Conservative values (equal to the predicted magnitude minus its uncertainty) were used in these figures.

5.5 Data Analysis

The response times of the four counters in the detector were all slightly different (see chapter 4 section 6). We offset the event times in the spectrum from each counter to compensate for these differences, then combined the four spectra into one. With the exception of the necessity that all recorded events be above discriminator threshold (which resulted in a loss of roughly 12% of SPE-size events, as discussed in section 4.1 above), no restrictions on pulse height were imposed in compiling the time spectra. The pulse-height spectra were not combined, due to the difficulty of adjusting for

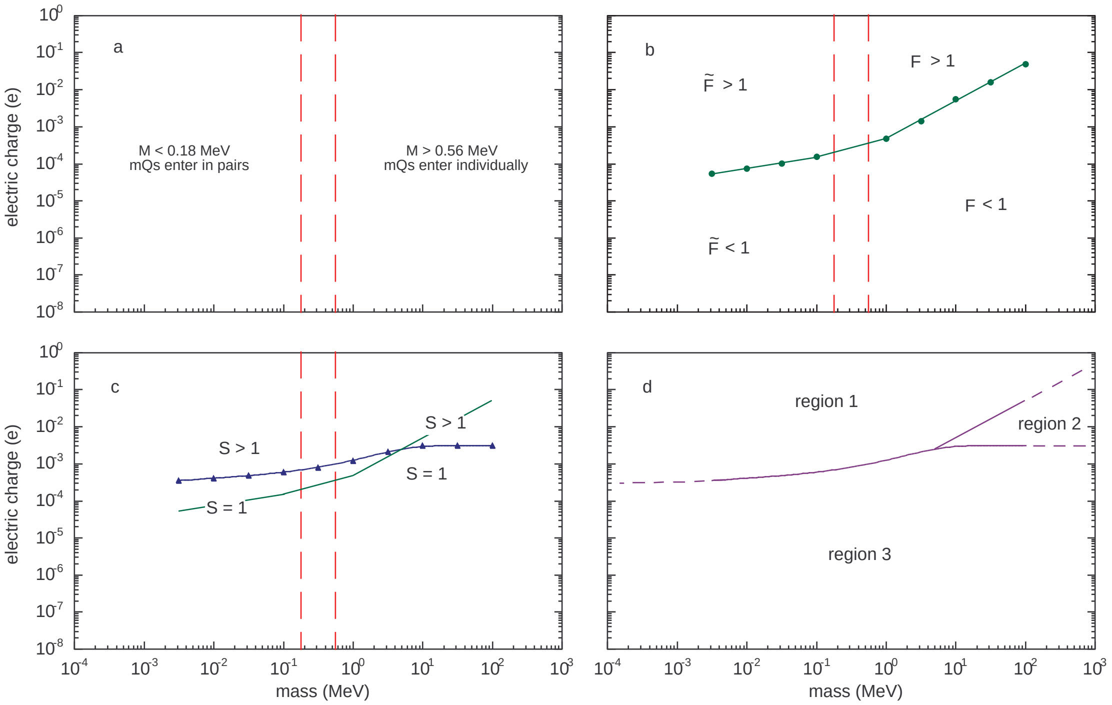

Figure 5.11: Regions of charge-mass parameter space relevant to the prediction of N and S. a) Right side: mQs enter the detector singly. Left side: mQs enter the detector in pairs. b) Above the green line: more than one mQ (pair) enters the detector per PPB. Below: one or fewer enters per PPB. c) Above the purple line: the pulse height of mQ events is greater than an SPE. Below: the pulse height is equal to an SPE. d) Region 1: an mQ event would be recorded for every PPB. Region 2: mQ events would have large pulse height, but would occur on only a fraction of PPBs. Region 3: mQ events would occur on only a fraction of PPBs, and would have SPE pulse height.

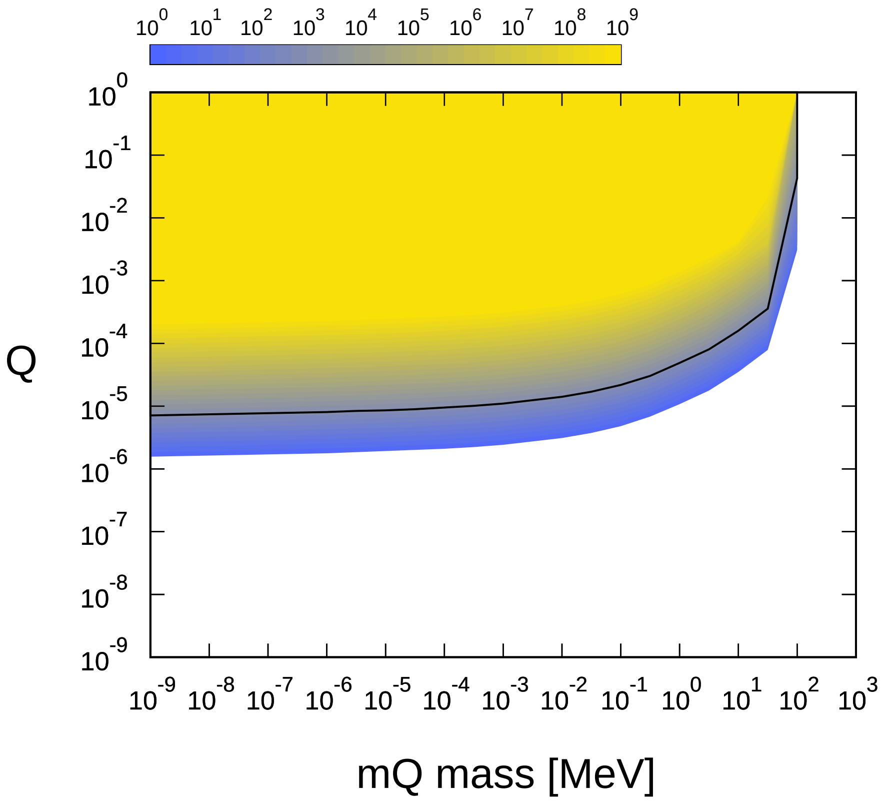

Figure 5.12: Contour plot of the expected number of mQ events (N). The black line is the contour $N = N_{\mathrm{max}}$.

PMT gain differences.

The time and pulse-height spectra of events in the main data set are shown in Figures 5.14 and 5.15. The expected location of the mQ peak in the time spectrum, given the offsets applied to its constituent spectra, and assuming an average pulse-height of one PE, is 108 ns. There are no notable peaks in the time spectrum, and there is nothing incommensurate with background in the pulse-height spectra. Except in region 3 of charge-mass parameter space (defined in Fig. 5.11 d), the minimum value of N for mQ masses below 100 MeV/c^2 is 4×10^6. This exceeds the number of events in the entire data set by a factor of four. With the exception of those portions of charge-mass parameter space for which mQs fail to reach the detector (discussed in chapter 3 section 3), a cursory inspection of the data is therefore all that is required

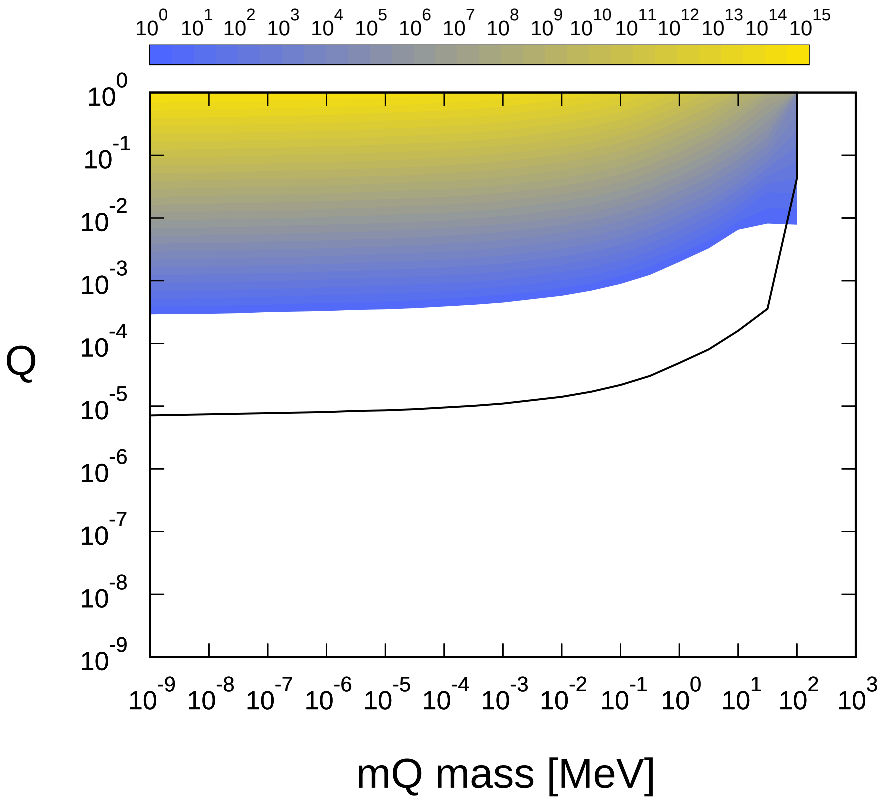

Figure 5.13: Contour plot of the expected pulse height (in SPEs) of mQ events. The black line is an overlay of the $N = N_{\max}$ contour from the N plot.

to exclude regions 1 and 2. In the remaining region, the average pulse-height of mQ events is one PE.

The shape expected for the mQ-induced peak (see Fig. 5.10), is characterized by a sharp leading edge, long tail, and FWHM of 20 ns. A window stretching from 103 ns to 143 ns (enclosing 86% of the expected peak) was chosen in which to seek a statistically significant excess of events. The regions 40 ns in length immediately adjacent to this signal window were used to obtain an estimate of background. The expected number of background events in the signal window (B = 146061) was extrapolated using a linear least-squares fit to the spectrum of events in the background regions. The signal window, background regions and fit used for background estimation are shown in Figure 5.16. The total number of events, T, in the signal window is 146268, an

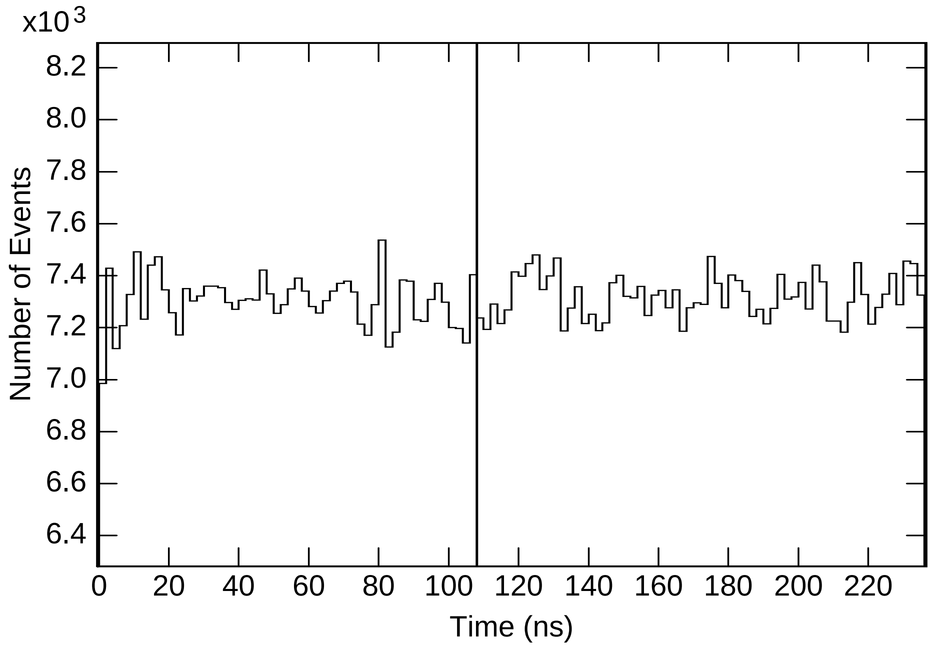

Figure 5.14: Time spectrum of events in the main data set. The vertical line shows the expected position of the mQ-induced peak.

excess of 207 events over the predicted background.

We assume that the number of background events in the signal region would, in an ensemble of identically run experiments, fluctuate according to a Poisson distribution, and use our expected value (146061 events) as an estimate of the mean ($\overline{B}$) of this distribution. With $\overline{B} \gg 1$, the Poisson distribution can be approximated by a gaussian distribution with standard deviation σ_B given by $\sigma_B = \sqrt{\overline{B}}$. The number of excess events in the signal window is only $0.54\,\sigma_B$, not statistically significant.

5.5.1 The Upper Limit on mQ Charge

Let T stand for the total number of events in the signal window. T is equal to the number of background events (B) plus the number of mQ events (N). There is only a 5% probability for B to fluctuate downward by more than $1.645\,\sigma_B$, and thus for N

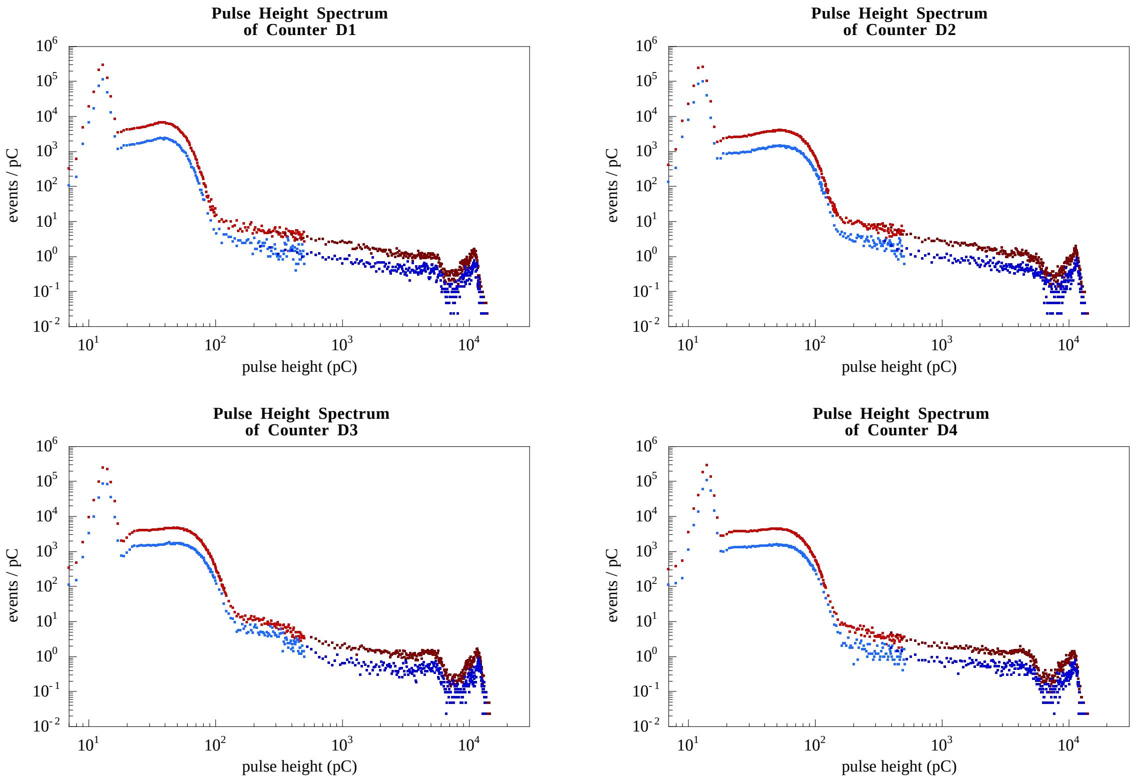

Figure 5.15: Pulse-height spectrum of events in final data set, for each counter. The upper (red) curve is the data. The lower (blue) curve, included for comparison, is comprised of background events (recorded when no PPB was present).

to be higher than $T-(\overline{B}-1.645\,\sigma_B)$. There is thus a 95% probability that $N < N_{\mathrm{max}}$, where $N_{\mathrm{max}} = T-(\overline{B}-1.645\,\sigma_B) = 835.68$. The black line in Figure 5.12 indicates the contour $N = N_{\mathrm{max}}$, and represents the 95% confidence upper limit on mQ charge. The location of this contour in the plot of expected PMT pulse height S (see Fig. 5.13) confirms that our assumption of an SPE for the most likely mQ signal is justified.

The portion of charge-mass parameter space excluded by the experiment, overlayed on the regions excluded by previous experiments and by cosmological arguments, is shown in Figure 5.17. The rightmost edge is determined by the fall-off of mQ yield with increasing mQ mass. The upper edge represents the maximum mQ charge that

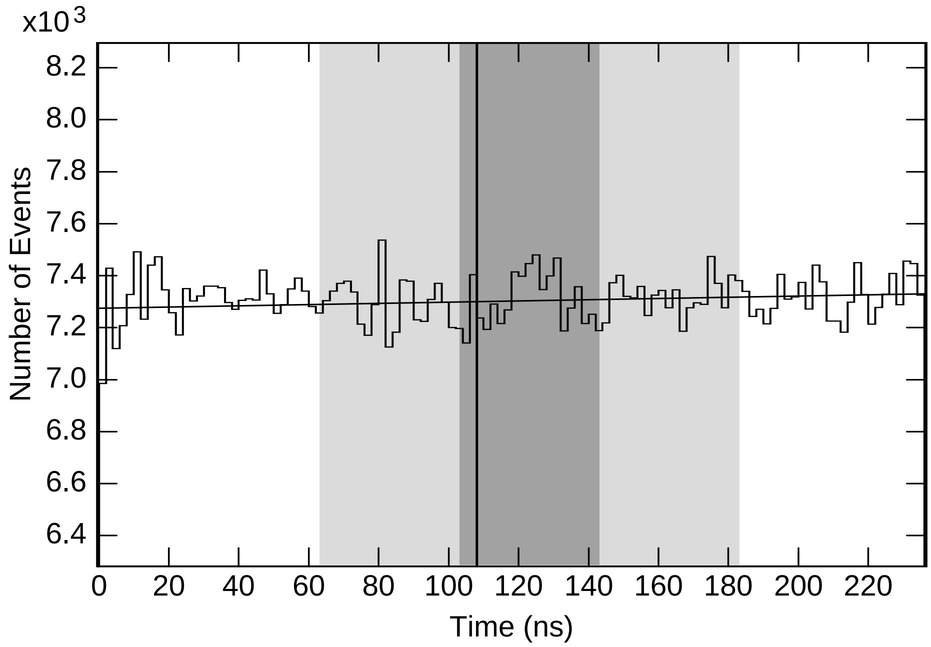

Figure 5.16: Time spectrum of events in the main data set, together with the signal window (darker shading), the regions used for background estimation (lighter shading), and the linear fit of the background.

is expected to reach the detector (given ionization and radiative energy loss in the material between the PPT and the detector, as discussed in chapter 3 section 3). The lower edge is the 95% confidence upper bound on mQ charge derived above.

This analysis relied on the assumption that the pulse-height calibration of the detector, carried out for large energy depositions, was accurate in the case of a single ionization. A separate analysis, involving the energy deposited by mQs in the form of delta rays, was performed as a cross check. The resulting charge limit (the lower edge of the excluded contour) was less stringent than the one from the main analysis, but differed by less than a factor of two.

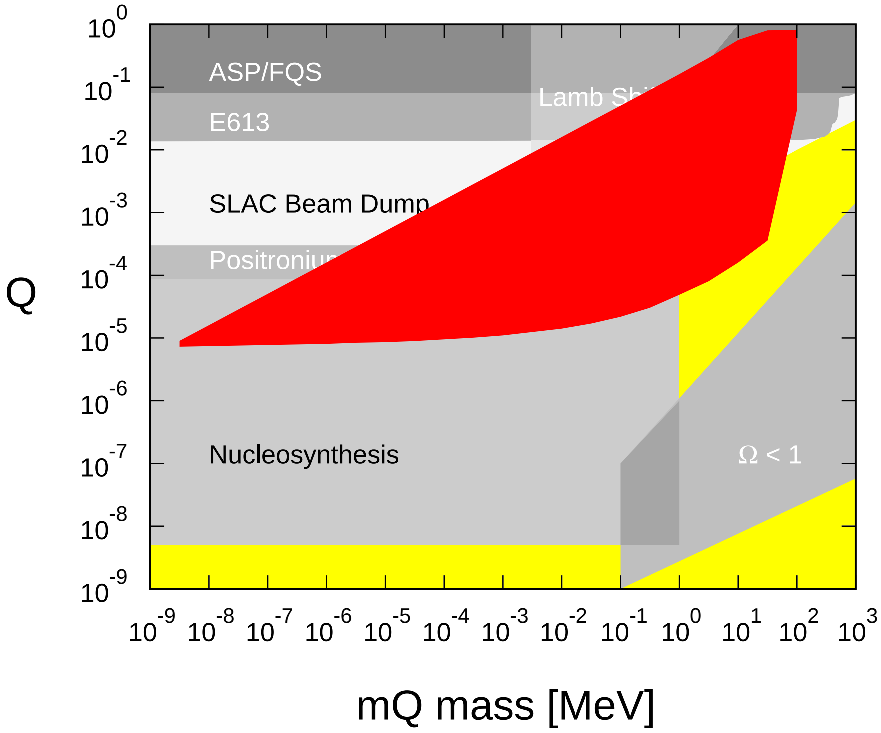

Figure 5.17: Region of charge-mass parameter space (red) ruled out by the mQ search.

Chapter 6

Conclusions

The experiment collected data representing $3.4{\times}10^8$ electron bunches incident on the SLC positron-production target (1.7 Coulombs of charge, total), at an electron energy of 29.5 GeV, using a plastic scintillation counter with a 1.3-meter path length for mQ interactions and a solid-angle coverage sufficient to accept 20% of the mQ beam. No evidence of mQ interactions (which would have been indicated by a peak in the time spectrum of recorded events) was found.

Figure 6.1 shows the contour in charge-mass parameter space that can be excluded, at 95% confidence, by this result. The lower edge of the contour is determined by the expected yield of mQs from the target, together with the maximum sensitivity of the detector. The right side of the contour is determined primarily by the expected yield. The upper left edge is determined by the maximum charge that would allow a mQ to penetrate the shielding between the target and the detector. (At low mass, mQs can lose a significant amount of energy to Bremsstrahlung in the shielding.) Also shown in the figure (in various shades of grey) are regions ruled out by previous experiments and by cosmological arguments. (It should be noted that the nucleosynthesis bound does not apply in the case that the tau neutrino is heavier than one MeV/c^2.)

The sensitivity of the experiment was limited primarily by noise intrinsic to the

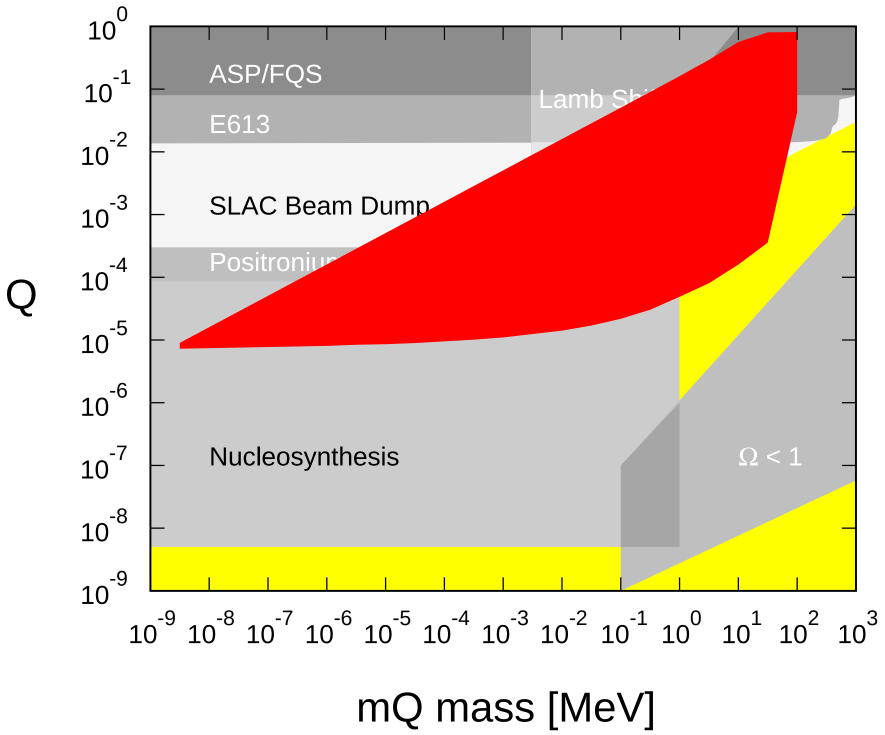

Figure 6.1: Region of charge-mass parameter space (red) ruled out by the mQ search.

detector. The noise pulses were small (single-photoelectron size), and most likely represent dark pulses from the photomultiplier tubes. Since the expected signal varies as the fourth power of mQ charge, an experiment seeking to extend the lower edge of the excluded contour by a modest amount would require a very large improvement in the signal-to-noise ratio.

Some possible avenues for improving upon the present result in future experiments include the following. A search at a higher energy accelerator would allow access to higher values of mQ mass. Use of higher density shielding with a detector placed closer to the source would increase mQ flux by improving solid-angle coverage. (It is probably not cost-effective to increase the width of the detector.) Alternatively, the search could by located at a higher current machine. A reduction in noise level by two to three orders of magnitude may, in the near future, be possible by replacing the photomultiplier tube with a semiconductor-based photon detector, such as a field-effect transistor gated by a layer of quantum dots[81]. And a more effective probe of the low-mass region may be achievable by exploiting the mQ cross section for e^+e^- pair production, *e.g.,* in a detector consisting of alternating layers of scintillator and a high-Z material.

Appendix A

Production Monte Carlo

This appendix describes the Monte Carlo used to estimate the yield, angular distribution and energy distribution of mQs produced in SLAC's positron-production target (PPT). Also included are the results of the simulation for some representative mQ masses.

A.1 Description of Monte Carlo

Each shower e^+ and e^- in the target is considered an incident particle capable of generating mQs. Shower parameters including the abundance, angular distribution and path length of e^+ and e^-, as a function of e^+e^- energy, were obtained via an EGS4[70] simulation. These data serve as input to the Monte Carlo, which generates a two-dimensional histogram of mQ yield (per PPB electron incident on the PPT) versus mQ angle and mQ energy. The Monte Carlo performs a phase-space integration of the differential cross section for Bremsstrahlung electroproduction (Figure A.1 B), computed using REDUCE[74], via the method of weights.

The cross section corresponding to the Bremsstrahlung electroproduction diagram

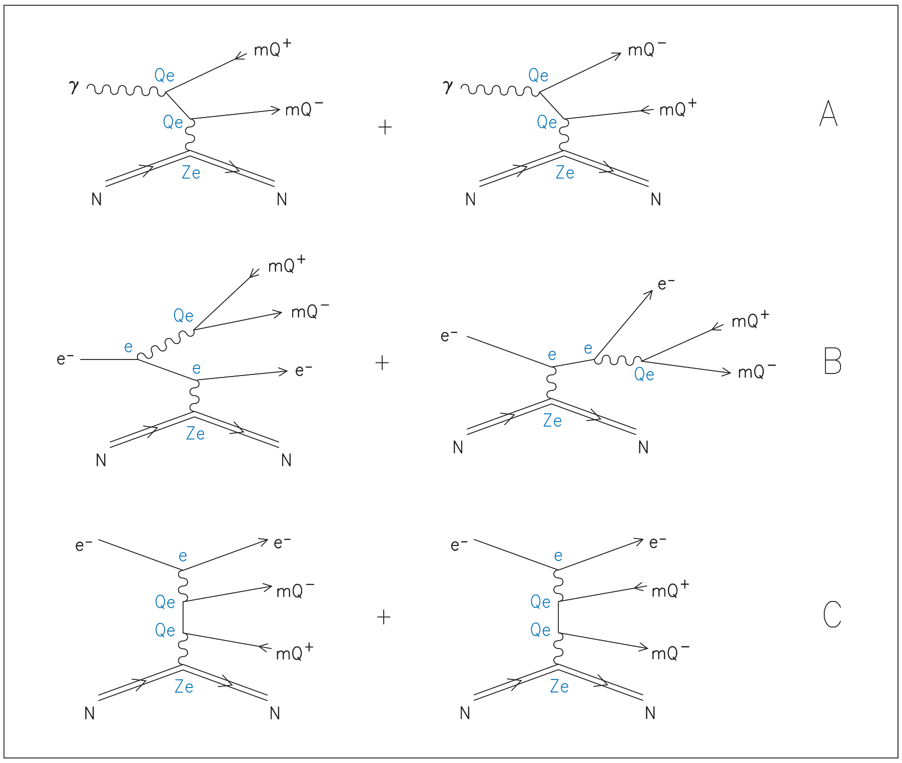

Figure A.1: Feynman diagrams for mQ production. A. Photoproduction. B. Electroproduction, "Bremsstrahlung" mechanism. C. Electroproduction, "multiperipheral" mechanism.

is given by

$$d\sigma = \frac{\delta^4(p'_e + p_{mQ^-} + p_{mQ^+} + p'_N - p_e - p_N)}{2(2\pi)^8\left[(p_e + p_N)^2 - M_N^2\right]} |\mathcal{M}|^2 \frac{d^3p'_e}{2E'_e}\frac{d^3p_{mQ^-}}{2E_{mQ^-}}\frac{d^3p_{mQ^+}}{2E_{mQ^+}}\frac{d^3p'_N}{2E'_N} \quad (A.1)$$

where primes refer to scattered particles, and units are such that $\hbar = c = 1$. We make the following three approximations: $p'_N \cong p_N = (M_N, 0, 0, 0)$ (since the nucleus is far heavier than any other mass scale in the process); the outgoing electron (positron) and mQs are highly relativistic; and $M_e \ll M_N$. Then the cross section in the lab frame simplifies to

$$d\sigma = \frac{\delta(E'_e + E_{mQ^-} + E_{mQ^+} - E_e)}{64(2\pi)^8 E_e M_N^2} |\mathcal{M}|^2 \frac{d^3p'_e}{E'_e}\frac{d^3p_{mQ^-}}{E_{mQ^-}}\frac{d^3p_{mQ^+}}{E_{mQ^+}}. \quad (A.2)$$

For our simulation we take d^3p_x in polar coordinates ($\mathrm{d}^3p_\mathrm{x} = E_\mathrm{x}^2\,\mathrm{d}E_\mathrm{x}\sin\theta_\mathrm{x}\times\ \mathrm{d}\theta_\mathrm{x}\,\mathrm{d}\phi_\mathrm{x}$) and make the change of variables $E_{\mathrm{mQ}^-}, E_{\mathrm{mQ}^+} \longrightarrow E_\mathrm{M}, R$, where $E_\mathrm{M} = E_{\mathrm{mQ}^-}+E_{\mathrm{mQ}^+}$, and $R = E_{\mathrm{mQ}^-}/E_\mathrm{M}$. The cross section becomes

$$\mathrm{d}\sigma = |\mathcal{M}|^2\,\frac{|\vec{p}_\mathrm{e}'|\,|\vec{p}_{\mathrm{mQ}^-}|\,|\vec{p}_{mQ^+}|}{64(2\pi)^7 E_\mathrm{e} M_\mathrm{N}^2} E_\mathrm{M}\sin\theta_\mathrm{e}'\sin\theta_{\mathrm{mQ}^-}\sin\theta_{\mathrm{mQ}^+}\times \tag{A.3}$$

$$\mathrm{d}\theta_\mathrm{e}'\mathrm{d}\theta_{\mathrm{mQ}^-}\mathrm{d}\theta_{\mathrm{mQ}^+}\mathrm{d}\phi_{\mathrm{mQ}^-}\mathrm{d}\phi_{\mathrm{mQ}^+}\mathrm{d}E_\mathrm{M}\mathrm{d}R, \tag{A.4}$$

where the ϕ_e' and E_e' integrations have been carried out, ϕ_{mQ^-} and ϕ_{mQ^+} are defined relative to the azimuthal direction of the scattered electron (positron), and energy conservation is imposed. To obtain the number of mQ pairs produced per e^- incident on the PPT, we integrate the following expression:

$$\mathrm{d}N_{\mathrm{pair}} = n\,l(E_\mathrm{e})\,\mathrm{d}E_\mathrm{e}\mathrm{d}\sigma. \tag{A.5}$$

Here $l(E_\mathrm{e})$ is the sum of the path lengths in the target, per unit energy, of all shower electrons and positrons having a given energy E_e, and n is the number density of atoms in the target. The quantity $l(E_\mathrm{e})$, as well as the angular spread of electrons and positrons for the given energy, is provided by the EGS4 simulation.

For the $\mathrm{d}N_{\mathrm{pair}}$ integration, points are generated in the 8-dimensional space $\big(\theta_\mathrm{e}', \theta_{\mathrm{mQ}^-}, \theta_{\mathrm{mQ}^+}, \phi_{\mathrm{mQ}^-}, \phi_{\mathrm{mQ}^+}, R, E_\mathrm{M}, E_\mathrm{e}\big)$ according to a density function $\rho(\mathbf{x})$, with $\rho(\mathbf{x})$ normalized such that $\int\rho(\mathbf{x})\,\mathrm{d}\mathbf{x} = N_{\mathrm{trials}}$. The number of mQ pairs per incident e^- is

$$N_{\mathrm{pair}} = \sum_{i=1}^{N_{\mathrm{trials}}} \frac{|\vec{p}_\mathrm{e}'|\,|\vec{p}_{\mathrm{mQ}^-}|\,|\vec{p}_{mQ^+}|}{64(2\pi)^7 E_\mathrm{e} M_\mathrm{N}^2}\,\frac{n\,l(E_\mathrm{e})\,|\mathcal{M}|^2\,E_\mathrm{M}\sin\theta_\mathrm{e}'\,\sin\theta_{\mathrm{mQ}^-}\sin\theta_{\mathrm{mQ}^+}}{\rho(\theta_\mathrm{e}', \theta_{\mathrm{mQ}^-}, \theta_{\mathrm{mQ}^+}, \phi_{\mathrm{mQ}^-}, \phi_{\mathrm{mQ}^+}, R, E_\mathrm{M}, E_\mathrm{e})}. \tag{A.6}$$

The quantity to the right of the summation symbol (W_i) is the weight of the ith event, and $\sum_i W_\mathrm{i}^2$ is the statistical uncertainty of $\sum_i \rho_\mathrm{i} W_\mathrm{i}$. Random numbers needed for the simulation are generated by the CERNLIB function RANMAR, which is based on the Marsaglia algorithm[75], with a periodicity of roughly 10^{43}.

E_e is sampled from a flat distribution between 0.5 and 29.5 GeV. R is sampled from a flat distribution between $M_{\mathrm{mQ}}/E_{\mathrm{M}}$ and $1 - M_{\mathrm{mQ}}/E_{\mathrm{M}}$. ϕ_{mQ^-} and ϕ_{mQ^+} are sampled from flat distributions between 0 and 2π. E_{M} is sampled from the distribution

$$h(E_{\mathrm{M}})\,\mathrm{d}E_{\mathrm{M}} = \frac{\mathrm{d}E_{\mathrm{M}}}{E_{\mathrm{M}} \ln\left(\frac{E_{\mathrm{e}}-m_{\mathrm{e}}}{2M_{\mathrm{mQ}}}\right)} \tag{A.7}$$

between the limits $2M_{\mathrm{mQ}}$ and $(E_{\mathrm{e}} - m_{\mathrm{e}})$. E'_{e}, E_{mQ^-} and E_{mQ^+} are computed from E_{e}, E_{M} and R. θ'_{e}, θ_{mQ^-} and θ_{mQ^+} are sampled from the distribution

$$g(\theta)\,\mathrm{d}\theta = \frac{2M_{\mathrm{max}}^2\,\theta\,\mathrm{d}\theta}{\left(E\theta^2 + M_{\mathrm{max}}^2/E\right)^2}, \tag{A.8}$$

which is the small-angle approximation to the distribution

$$g(\theta)\,\mathrm{d}\theta = \frac{M_{\mathrm{max}}^2 \sin\theta\,\mathrm{d}\theta}{2\left(E - E\cos\theta\right)^2}, \tag{A.9}$$

where $M_{\mathrm{max}} = \max(M_{\mathrm{mQ}}, m_{\mathrm{e}})$, and E is the energy of the particle under consideration. This distribution is tailored to avoid both very large and very small angles, and thus will not give good results when $M_{\mathrm{mQ}} \ll m_{\mathrm{e}}$.

The density function ρ is given by

$$\begin{aligned}\rho\left(\theta'_{\mathrm{e}}, \theta_{\mathrm{mQ}^-}, \theta_{\mathrm{mQ}^+}, \phi_{\mathrm{mQ}^-}, \phi_{\mathrm{mQ}^+}, R, E_{\mathrm{M}}, E_{\mathrm{e}}\right) = \\ N_{\text{trials}}\, g(\theta'_{\mathrm{e}})\, g(\theta_{\mathrm{mQ}^-})\, g(\theta_{\mathrm{mQ}^+})\, \frac{1}{(2\pi)^2} \frac{1}{1 - 2M_{\mathrm{mQ}}/E_{\mathrm{M}}} h(E_{\mathrm{M}})\, \frac{l(E_{\mathrm{e}})}{l_{\mathrm{tot}}},\end{aligned} \tag{A.10}$$

where $l_{\mathrm{tot}} = \int l(E_{\mathrm{e}})\,\mathrm{d}E_{\mathrm{e}}$. This leads to the following expression for the weights:

$$\begin{aligned}W_{\mathrm{i}} =& n\,|\mathcal{M}|^2\, \frac{|\vec{p}'_{\mathrm{e}}|\,|\vec{p}_{\mathrm{mQ}^-}|\,|\vec{p}_{mQ^+}|}{64(2\pi)^7 E_{\mathrm{e}} M_{\mathrm{N}}^2} \times \\ & \frac{E_{\mathrm{M}} \sin\theta'_{\mathrm{e}}\, \sin\theta_{\mathrm{mQ}^-}\, \sin\theta_{\mathrm{mQ}^+}\, (2\pi)^2\, (1 - 2M_{\mathrm{mQ}}/E_{\mathrm{M}})\, l_{\mathrm{tot}}}{N_{\text{trials}}\, g(\theta'_{\mathrm{e}})\, g(\theta_{\mathrm{mQ}^-})\, g(\theta_{\mathrm{mQ}^+})\, h(E_{\mathrm{M}})\, l(E_{\mathrm{e}})}.\end{aligned} \tag{A.11}$$

To compute the matrix element $|\mathcal{M}|^2$, we assume the nucleus to be a fermion with charge $ZeF(q^2)$, where Z is the atomic number and $F(q^2)$ is a form factor. For $F(q^2)$ we use the elastic atomic form factor of Schiff as reported in Tsai[73]:

$$F^2(q^2) = G_2^{\mathrm{el}}(q^2) = \frac{(a^2q^2)^2}{(1+a^2q^2)^2} \tag{A.12}$$

where

$$a^2 = \frac{(184.15)^2}{2.718}\frac{1}{m_{\mathrm{e}}^2\, Z^{2/3}}, \tag{A.13}$$

so long as $|q^2| < m_{\mathrm{e}}^2$. For larger $|q^2|$ we use the elastic nuclear form factor of Tsai:

$$F^2(q^2) = \frac{W_2(\mathrm{coherent})}{Z^2} = \frac{2M_{\mathrm{N}}}{\left(1+|q^2|^2/d\right)^2} \tag{A.14}$$

where

$$d = 0.164\, A^{-2/3}\, \mathrm{GeV}^2. \tag{A.15}$$

The traces in the computation of the spin-averaged value of $|\mathcal{M}|^2$ were calculated using REDUCE[74].

To obtain the angular distribution of the mQs, a direction for the incoming electron (positron), relative to the incident e^- beam, is chosen on each trial. θ_{e} is sampled from a gaussian distribution (centered at 0), whose standard deviation was computed in the EGS4 shower simulation. ϕ_{e} is sampled from a flat distribution between 0 and 2π. The direction of the mQ relative to the electron (positron) which produced it is then appropriately rotated to obtain the mQ direction relative to the incident e^- beam.

A.2 Representative Results

The results of the Monte Carlo (from runs of 60-million trials) for mQ masses 0.01, 0.1, 1 and 10 MeV/c^2, are given in the tables that follow. The first lists the total yield, and the yield within our detector's 2-mr angular acceptance, of mQs produced in the PPT per incident PPB electron, assuming the mQ charge is $10^{-3}e$. (To obtain the results for other charges, scale by $10^6 Q^2$.) The next several tables represent two-dimensional histograms of mQ yield versus mQ energy and angle, for angles below 4 mr (again with $Q = 10^{-3}$). The vertical axis is mQ energy in GeV, and the horizontal axis is mQ angle in radians (values on the axes represent bin midpoints).

Table A.1: Total yield and accepted yield of mQs, per PPB electron, for $Q = 10^{-3}$. Mass values are in MeV/c^2.

M_{mQ}	yield	accepted yield
0.01	$(2.75 \pm 0.19) \times 10^{-7}$	$(4.64 \pm 0.47) \times 10^{-8}$
0.1	$(5.16 \pm 0.18) \times 10^{-8}$	$(1.022 \pm 0.065) \times 10^{-8}$
1	$(2.82 \pm 0.12) \times 10^{-9}$	$(5.46 \pm 0.37) \times 10^{-10}$
10	$(6.26 \pm 2.6) \times 10^{-11}$	$(4.0 \pm 2.3) \times 10^{-12}$

Table A.2: Results of Production Monte Carlo for $M_{\mathrm{mQ}} = 0.01$ MeV/c^2.

	Angle (rad)							
Energy(GeV)	0.000250	0.000750	0.00125	0.00175	0.00225	0.00275	0.00325	0.00375
0.125	7.76e-10	1.86e-09	3.98e-09	2.84e-09	2.47e-09	2.81e-09	2.77e-09	2.73e-09
0.375	8.11e-10	1.21e-09	1.66e-09	1.79e-09	1.82e-09	1.38e-09	3.52e-09	1.31e-09
0.625	5.49e-10	9.98e-10	1.21e-09	9.61e-10	1.20e-09	1.20e-09	1.30e-09	8.28e-10
0.875	4.16e-10	7.74e-10	9.63e-10	7.62e-10	1.16e-09	1.02e-09	6.72e-10	6.56e-10
1.125	4.63e-10	7.92e-10	9.08e-10	1.18e-09	6.23e-10	5.52e-10	5.08e-10	4.17e-10
1.375	3.42e-10	5.13e-10	6.49e-10	5.43e-10	6.19e-10	4.70e-10	3.34e-10	3.11e-10
1.625	3.84e-10	7.98e-10	3.99e-10	4.42e-10	3.24e-10	3.16e-10	8.20e-10	3.79e-10
1.875	2.61e-10	4.36e-10	3.37e-10	3.62e-10	3.13e-10	3.31e-10	2.44e-10	1.86e-10
2.125	2.63e-10	4.17e-10	4.02e-10	2.78e-10	3.41e-10	2.47e-10	2.44e-10	3.56e-10
2.375	2.05e-10	3.41e-10	3.41e-10	3.23e-10	2.47e-10	1.65e-10	1.05e-10	1.24e-10
2.625	1.79e-10	2.58e-10	5.18e-10	2.62e-10	1.56e-10	1.41e-10	1.17e-10	8.20e-11
2.875	1.43e-10	2.56e-10	3.22e-10	2.50e-10	1.82e-10	1.37e-10	6.78e-10	8.97e-11
3.125	1.32e-10	2.23e-10	2.14e-10	1.71e-10	1.72e-10	1.21e-10	7.16e-11	4.16e-11
3.375	1.33e-10	2.26e-10	2.15e-10	1.47e-10	1.04e-10	9.47e-11	7.15e-11	5.39e-11
3.625	1.33e-10	1.77e-10	1.79e-10	1.40e-10	1.02e-10	6.34e-11	4.94e-11	3.98e-11
3.875	8.99e-11	1.52e-10	1.46e-10	1.11e-10	1.10e-10	6.90e-11	3.73e-11	2.48e-11
4.125	8.33e-11	3.13e-10	1.74e-10	1.92e-10	7.31e-11	4.84e-11	4.53e-11	1.95e-11
4.375	8.78e-11	1.56e-10	1.76e-10	8.59e-11	6.73e-11	6.96e-11	2.91e-11	2.32e-11
4.625	8.96e-11	1.62e-10	1.12e-10	7.90e-11	6.43e-11	3.93e-11	2.89e-11	1.39e-11
4.875	9.17e-11	1.41e-10	9.97e-11	9.50e-11	4.90e-11	3.33e-11	1.74e-11	1.83e-11
5.125	8.01e-11	1.25e-10	1.09e-10	5.60e-11	4.56e-11	3.66e-11	1.52e-11	1.08e-11
5.375	7.03e-11	1.03e-10	1.17e-10	1.12e-10	4.23e-11	3.44e-11	1.43e-11	1.21e-11
5.625	7.22e-11	1.07e-10	6.84e-11	6.31e-11	4.66e-11	2.55e-11	1.44e-11	7.22e-12
5.875	6.03e-11	1.26e-10	6.43e-11	6.86e-11	4.45e-11	4.41e-11	1.14e-11	9.37e-12
6.125	8.31e-11	7.28e-11	7.53e-11	4.15e-11	3.19e-11	1.92e-11	8.36e-12	8.33e-12
6.375	5.75e-11	7.69e-11	5.59e-11	4.01e-11	2.73e-11	1.76e-11	5.01e-11	4.35e-12
6.625	4.14e-11	6.47e-11	5.89e-11	4.80e-11	2.86e-11	2.25e-11	5.97e-12	4.34e-12
6.875	5.19e-11	8.24e-11	7.48e-11	3.39e-11	1.95e-11	1.16e-11	5.40e-12	5.00e-12
7.125	4.67e-11	7.68e-11	5.33e-11	3.27e-11	2.82e-11	1.33e-11	6.63e-12	1.92e-12
7.375	7.12e-11	9.60e-11	4.23e-11	2.57e-11	2.22e-11	1.66e-11	7.33e-12	2.80e-12
7.625	3.12e-11	7.29e-11	3.97e-11	2.33e-11	1.26e-11	1.03e-11	4.76e-12	4.21e-12
7.875	4.46e-11	5.38e-11	3.67e-11	2.56e-11	1.59e-11	7.34e-12	6.60e-12	1.71e-12
8.125	7.22e-11	8.54e-11	4.67e-11	5.65e-11	1.63e-11	8.21e-12	3.79e-12	1.77e-12
8.375	3.42e-11	5.37e-11	3.87e-11	2.09e-11	2.22e-11	9.55e-12	3.44e-12	1.77e-12
8.625	3.34e-11	5.66e-11	6.52e-11	1.73e-11	1.11e-11	6.53e-12	2.97e-12	1.01e-12
8.875	4.10e-11	4.86e-11	2.26e-11	2.84e-11	2.98e-11	5.00e-12	2.57e-12	9.71e-13
9.125	2.48e-11	5.32e-11	3.06e-11	1.50e-11	1.41e-11	5.54e-12	3.07e-12	1.37e-12
9.375	2.19e-11	4.94e-11	2.51e-11	2.15e-11	8.25e-12	5.80e-12	3.12e-12	1.50e-12
9.625	2.82e-11	5.26e-11	1.95e-11	1.13e-11	5.84e-12	9.21e-12	1.87e-12	1.39e-12
9.875	2.78e-11	4.66e-11	3.66e-11	1.27e-11	8.30e-12	6.41e-12	2.57e-12	1.62e-12
10.125	2.24e-11	3.47e-11	2.57e-11	1.16e-11	1.13e-11	4.98e-12	2.06e-12	8.09e-13
10.375	5.59e-11	3.40e-11	2.73e-11	1.40e-11	6.36e-12	2.86e-12	2.94e-12	7.19e-13
10.625	4.47e-11	2.84e-11	2.03e-11	1.18e-11	1.02e-11	2.69e-12	1.40e-12	8.19e-13
10.875	1.86e-11	3.80e-11	1.57e-11	1.15e-11	4.60e-12	1.45e-12	1.55e-12	3.20e-13
11.125	3.39e-11	2.64e-11	2.27e-11	1.12e-11	1.39e-11	3.69e-12	1.78e-12	8.54e-12
11.375	2.83e-11	2.56e-11	2.44e-11	8.07e-12	3.86e-12	2.90e-12	2.00e-12	4.15e-13
11.625	1.96e-11	3.06e-11	1.66e-11	8.07e-12	5.55e-12	2.18e-12	1.24e-12	7.78e-13
11.875	2.77e-11	2.55e-11	1.41e-11	6.54e-12	1.12e-11	1.77e-12	1.17e-12	1.61e-12
12.125	3.17e-11	3.15e-11	1.44e-11	6.48e-12	4.15e-12	2.42e-12	9.88e-13	2.48e-13
12.375	1.30e-11	2.41e-11	1.11e-11	5.33e-12	4.56e-12	1.63e-12	6.92e-13	1.75e-13
12.625	1.41e-11	2.34e-11	1.19e-11	6.57e-12	5.04e-12	1.88e-12	5.74e-13	2.63e-12
12.875	1.45e-11	2.21e-11	1.03e-11	5.92e-12	2.85e-12	1.65e-12	5.56e-13	1.07e-13
13.125	1.11e-11	2.10e-11	1.17e-11	6.86e-12	4.07e-12	1.15e-12	1.13e-12	1.75e-13
13.375	1.09e-11	2.52e-11	1.88e-11	8.03e-12	1.74e-12	1.01e-12	9.91e-13	2.86e-13
13.625	1.27e-11	2.68e-11	1.18e-11	4.01e-12	1.36e-12	8.95e-13	4.70e-13	6.84e-13
13.875	1.09e-11	2.47e-11	1.11e-11	5.84e-12	4.00e-12	1.23e-12	5.02e-13	9.56e-14
14.125	1.08e-10	1.83e-11	7.49e-12	4.91e-12	2.22e-12	1.77e-12	8.89e-13	4.11e-13
14.375	9.41e-12	1.30e-11	7.83e-12	4.15e-12	1.56e-12	1.19e-12	2.18e-13	4.55e-14
14.625	1.34e-11	1.67e-11	1.08e-11	3.75e-12	1.38e-12	1.74e-12	2.59e-13	9.94e-14
14.875	9.05e-12	1.40e-11	7.46e-12	4.80e-12	1.11e-12	1.60e-12	2.16e-13	1.31e-13

Table A.3: Continuation of Results for $M_{\mathrm{mQ}} = 0.01$ MeV/c^2.

	Angle (rad)							
Energy(GeV)	0.000250	0.000750	0.00125	0.00175	0.00225	0.00275	0.00325	0.00375
15.125	1.09e-11	1.43e-11	5.80e-12	3.14e-12	2.78e-12	1.11e-12	2.97e-13	8.49e-14
15.375	8.73e-12	2.05e-11	8.56e-12	4.43e-12	1.14e-12	8.52e-13	3.24e-13	3.54e-14
15.625	9.50e-12	1.14e-11	6.12e-12	2.75e-12	2.53e-12	7.52e-13	5.93e-13	1.55e-13
15.875	1.25e-11	1.05e-11	5.31e-12	3.55e-12	2.38e-12	1.07e-12	2.31e-13	1.63e-13
16.125	7.70e-12	1.10e-11	6.45e-12	2.23e-12	1.90e-12	4.94e-13	2.11e-13	5.79e-14
16.375	5.48e-12	9.05e-12	1.39e-11	3.53e-12	1.79e-12	9.05e-13	2.22e-13	6.87e-14
16.625	7.85e-12	1.26e-11	3.88e-12	2.06e-12	7.04e-13	4.63e-13	3.69e-13	4.22e-14
16.875	6.44e-12	9.32e-12	4.10e-12	1.34e-12	1.51e-12	5.28e-13	3.25e-13	1.36e-13
17.125	8.25e-12	1.24e-11	5.50e-12	2.66e-12	1.26e-12	3.24e-13	3.59e-13	5.80e-14
17.375	1.05e-11	6.65e-12	4.08e-12	1.67e-12	1.78e-12	7.46e-13	2.22e-13	3.25e-14
17.625	8.64e-12	7.71e-12	6.28e-12	1.09e-12	5.53e-12	3.24e-12	1.46e-13	8.39e-14
17.875	4.44e-12	9.49e-12	1.75e-11	1.17e-12	5.98e-13	6.40e-13	1.67e-12	5.84e-14
18.125	7.96e-12	1.19e-11	7.46e-12	2.10e-12	7.87e-13	7.94e-13	1.47e-13	8.78e-14
18.375	5.93e-12	5.65e-12	3.72e-12	1.46e-12	5.24e-13	4.60e-13	2.23e-13	1.98e-14
18.625	5.95e-12	5.70e-12	2.49e-12	2.38e-12	1.10e-12	8.21e-14	1.94e-13	1.27e-14
18.875	5.33e-12	7.60e-12	2.86e-12	1.35e-12	7.14e-13	9.42e-13	1.03e-13	4.21e-14
19.125	4.41e-12	3.94e-12	2.27e-12	2.25e-12	5.88e-13	1.42e-13	1.07e-13	4.67e-14
19.375	4.62e-12	4.86e-12	5.74e-12	1.15e-12	4.14e-12	1.95e-13	7.49e-14	8.88e-14
19.625	4.93e-12	5.16e-12	1.90e-12	1.05e-12	3.64e-13	4.37e-13	5.00e-14	1.85e-14
19.875	6.89e-12	4.77e-12	2.31e-12	2.13e-12	2.76e-12	2.93e-13	1.18e-13	3.71e-14
20.125	3.42e-12	3.27e-12	2.01e-11	2.73e-12	5.98e-13	3.86e-13	2.76e-13	2.42e-14
20.375	3.85e-12	4.29e-12	3.59e-12	1.31e-12	1.05e-12	8.53e-14	6.48e-14	1.69e-14
20.625	3.20e-12	4.36e-12	4.36e-12	1.54e-12	4.64e-13	2.06e-13	4.04e-14	6.24e-15
20.875	2.10e-12	5.89e-12	3.50e-12	6.20e-13	4.39e-13	2.48e-13	1.01e-13	1.18e-14
21.125	1.77e-12	4.62e-12	1.42e-12	1.16e-12	3.67e-13	1.90e-13	2.28e-13	2.34e-15
21.375	2.50e-12	3.25e-12	1.72e-12	7.55e-13	1.22e-13	1.93e-13	2.83e-14	4.29e-14
21.625	2.80e-12	3.88e-12	1.55e-12	3.34e-13	8.58e-13	1.56e-13	1.12e-14	1.11e-14
21.875	3.34e-12	3.51e-12	1.69e-12	7.32e-13	8.80e-13	3.55e-14	1.71e-13	1.01e-15
22.125	1.96e-12	1.97e-12	7.78e-13	3.61e-13	3.00e-13	3.91e-14	1.29e-14	6.15e-15
22.375	2.45e-12	1.95e-12	1.71e-12	5.38e-13	3.90e-13	3.16e-13	4.56e-14	5.93e-15
22.625	1.18e-12	2.30e-12	4.52e-12	5.85e-13	1.86e-12	9.00e-14	2.18e-12	1.19e-14
22.875	2.07e-12	3.34e-12	1.44e-12	6.77e-13	2.65e-12	5.06e-14	1.16e-13	2.32e-14
23.125	1.72e-12	3.18e-12	7.06e-13	4.46e-13	1.02e-12	4.09e-14	4.91e-14	1.42e-14
23.375	1.35e-12	2.62e-12	1.37e-12	1.56e-12	4.20e-13	5.12e-14	1.43e-14	1.15e-14
23.625	1.42e-12	6.80e-12	5.38e-13	9.83e-13	1.08e-13	3.55e-14	7.73e-15	1.63e-14
23.875	6.41e-13	1.45e-12	7.80e-13	5.62e-13	1.43e-13	6.79e-14	2.34e-13	1.00e-14
24.125	1.05e-12	8.71e-13	7.65e-13	9.82e-13	6.05e-13	2.13e-13	5.58e-14	4.16e-14
24.375	1.53e-12	9.65e-13	6.84e-13	1.35e-12	8.38e-14	1.63e-13	1.95e-14	5.28e-14
24.625	4.72e-13	7.41e-13	1.67e-12	5.04e-13	1.31e-13	3.97e-14	1.24e-14	4.32e-15
24.875	5.21e-13	7.93e-13	7.37e-13	1.70e-13	4.07e-13	6.10e-14	3.85e-14	2.31e-15
25.125	2.80e-12	7.14e-12	5.76e-13	2.86e-13	2.27e-13	1.89e-14	3.46e-14	1.33e-15
25.375	2.69e-12	5.27e-12	8.08e-13	5.10e-13	1.67e-13	1.95e-12	1.98e-15	4.95e-13
25.625	1.40e-12	8.38e-13	3.20e-13	1.46e-13	1.07e-13	1.80e-14	7.44e-15	3.70e-14
25.875	6.23e-13	2.50e-12	2.12e-13	8.97e-14	1.34e-13	5.51e-14	1.51e-14	6.05e-15
26.125	2.25e-13	2.73e-13	2.86e-13	1.01e-13	9.21e-14	2.36e-14	3.88e-14	3.78e-15
26.375	5.88e-13	4.67e-13	1.24e-13	3.73e-14	1.98e-14	4.12e-14	3.82e-14	9.30e-16
26.625	6.95e-13	4.04e-13	3.98e-13	7.24e-14	1.24e-13	3.42e-14	1.28e-14	2.40e-17
26.875	9.66e-14	4.58e-13	2.06e-13	7.60e-14	9.93e-14	2.28e-14	1.87e-14	2.39e-15
27.125	5.50e-14	1.36e-13	2.28e-13	5.86e-14	2.26e-14	1.14e-14	1.50e-14	1.17e-15
27.375	1.03e-13	2.02e-13	3.86e-14	1.16e-13	1.37e-14	2.35e-14	2.86e-15	0.00
27.625	3.82e-14	6.11e-14	1.31e-12	3.52e-13	2.95e-14	1.04e-14	2.08e-16	1.35e-15
27.875	4.07e-13	2.45e-13	3.40e-14	7.38e-14	1.27e-14	5.53e-15	8.67e-16	1.67e-15
28.125	7.81e-15	7.61e-14	1.26e-14	3.02e-14	3.25e-14	6.19e-15	2.05e-16	4.37e-16
28.375	7.76e-15	7.43e-13	5.25e-14	4.79e-12	1.66e-14	5.81e-16	0.00	0.00
28.625	9.00e-15	1.03e-14	2.79e-14	2.73e-14	5.12e-14	4.11e-13	7.66e-16	0.00
28.875	2.61e-15	4.07e-15	7.06e-15	1.97e-14	1.18e-15	1.52e-15	0.00	0.00
29.125	9.51e-17	1.77e-15	4.41e-16	6.44e-16	1.21e-14	0.00	0.00	0.00
29.375	0.00	3.55e-15	0.00	1.92e-15	0.00	0.00	0.00	0.00
29.625	0.00	0.00	0.00	0.00	0.00	0.00	0.00	0.00
29.875	0.00	0.00	0.00	0.00	0.00	0.00	0.00	0.00

Table A.4: Results of Production Monte Carlo for $M_{\mathrm{mQ}} = 0.1$ MeV/c^2.

	Angle (rad)							
Energy(GeV)	0.000250	0.000750	0.00125	0.00175	0.00225	0.00275	0.00325	0.00375
0.125	5.15e-11	2.39e-10	1.90e-10	2.28e-10	2.52e-10	2.59e-10	3.45e-10	2.89e-10
0.375	9.09e-11	2.03e-10	2.53e-10	3.45e-10	3.66e-10	3.14e-10	3.06e-10	2.87e-10
0.625	8.24e-11	2.06e-10	2.06e-10	2.34e-10	2.68e-10	2.43e-10	2.56e-10	2.36e-10
0.875	9.10e-11	1.55e-10	1.81e-10	5.34e-10	5.20e-10	1.99e-10	1.94e-10	1.84e-10
1.125	6.47e-11	1.29e-10	1.49e-10	1.68e-10	1.54e-10	1.74e-10	1.99e-10	1.33e-10
1.375	6.75e-11	1.14e-10	1.43e-10	1.40e-10	1.48e-10	1.43e-10	1.14e-10	1.24e-10
1.625	5.96e-11	1.08e-10	1.11e-10	1.37e-10	1.11e-10	9.51e-11	5.37e-10	7.84e-11
1.875	5.08e-11	1.11e-10	1.07e-10	9.99e-11	1.13e-10	8.88e-11	7.35e-11	8.12e-11
2.125	5.45e-11	1.01e-10	1.03e-10	8.94e-11	7.54e-11	7.83e-11	5.83e-11	7.37e-11
2.375	4.90e-11	7.95e-11	8.03e-11	8.16e-11	6.10e-11	1.01e-10	5.52e-11	4.32e-11
2.625	4.93e-11	7.72e-11	1.93e-10	7.57e-11	6.19e-11	4.93e-11	3.77e-11	3.70e-11
2.875	5.21e-11	7.14e-11	6.76e-11	6.46e-11	5.36e-11	4.09e-11	4.71e-10	2.90e-11
3.125	3.84e-11	6.24e-11	6.04e-11	8.25e-11	4.72e-11	3.58e-11	2.83e-11	2.61e-11
3.375	3.39e-11	6.20e-11	8.11e-11	4.75e-11	3.95e-11	3.85e-11	2.43e-11	1.84e-11
3.625	5.61e-11	5.83e-11	5.26e-11	4.11e-11	4.12e-11	4.08e-11	1.87e-11	1.48e-11
3.875	2.85e-11	5.09e-11	5.27e-11	4.01e-11	3.91e-11	2.20e-11	1.86e-11	1.18e-11
4.125	2.92e-11	5.40e-11	4.45e-11	4.12e-11	2.74e-11	2.10e-11	2.17e-11	9.05e-12
4.375	2.64e-11	1.81e-10	4.34e-11	3.26e-11	2.35e-11	1.66e-11	1.21e-11	8.79e-12
4.625	3.75e-11	4.37e-11	4.08e-11	2.94e-11	2.47e-11	1.80e-11	1.20e-11	6.25e-12
4.875	2.70e-11	4.51e-11	3.74e-11	2.81e-11	1.91e-11	1.47e-11	9.48e-12	5.19e-12
5.125	2.65e-11	3.87e-11	3.33e-11	2.36e-11	2.06e-11	1.57e-11	6.56e-12	4.89e-12
5.375	2.38e-11	3.60e-11	5.39e-11	2.45e-11	1.61e-11	1.11e-11	6.80e-12	5.74e-12
5.625	2.24e-11	3.39e-11	2.56e-11	2.57e-11	1.54e-11	1.03e-11	5.33e-12	3.96e-12
5.875	1.80e-11	3.08e-11	2.66e-11	1.96e-11	1.75e-11	1.15e-11	5.59e-12	2.40e-12
6.125	1.81e-11	3.15e-11	2.45e-11	1.56e-11	1.21e-11	9.54e-12	4.78e-12	1.88e-12
6.375	1.95e-11	2.82e-11	2.25e-11	1.53e-11	1.20e-11	7.28e-12	3.65e-12	2.64e-12
6.625	1.64e-11	2.59e-11	2.23e-11	1.67e-11	9.80e-12	5.74e-12	4.18e-12	2.05e-12
6.875	1.51e-11	2.77e-11	2.14e-11	1.60e-11	1.05e-11	5.13e-12	2.82e-12	1.40e-12
7.125	1.78e-11	2.61e-11	1.70e-11	1.14e-11	9.83e-12	5.47e-12	2.96e-12	1.70e-12
7.375	1.48e-11	2.38e-11	1.61e-11	1.13e-11	6.68e-12	4.82e-12	2.68e-12	1.11e-12
7.625	1.43e-11	2.34e-11	1.84e-11	1.08e-11	6.04e-12	3.79e-12	3.00e-12	1.32e-12
7.875	1.37e-11	2.74e-11	1.56e-11	9.73e-12	5.40e-12	3.24e-12	1.37e-12	1.10e-12
8.125	1.34e-11	2.02e-11	1.33e-11	8.67e-12	6.83e-12	3.23e-12	1.94e-12	1.21e-12
8.375	1.35e-11	1.98e-11	1.34e-11	9.62e-12	5.53e-12	2.89e-12	1.51e-12	8.22e-13
8.625	1.08e-11	1.72e-11	1.27e-11	8.63e-12	5.58e-12	3.30e-12	1.62e-12	6.40e-13
8.875	1.06e-11	1.65e-11	1.10e-11	8.61e-12	6.02e-12	2.59e-12	1.05e-12	4.61e-13
9.125	1.11e-11	2.10e-11	1.13e-11	7.25e-12	3.97e-12	2.26e-12	1.33e-12	4.13e-13
9.375	9.80e-12	1.65e-11	9.80e-12	7.93e-12	3.49e-12	2.00e-12	8.39e-13	6.69e-13
9.625	1.04e-11	1.79e-11	1.00e-11	5.77e-12	3.23e-12	2.18e-12	7.58e-13	8.35e-13
9.875	8.66e-12	1.55e-11	1.09e-11	6.13e-12	2.86e-12	1.92e-12	9.71e-13	4.01e-13
10.125	8.77e-12	1.35e-11	8.44e-12	4.76e-12	3.93e-12	1.82e-12	6.87e-13	1.05e-12
10.375	9.56e-12	1.33e-11	7.65e-12	4.11e-12	2.50e-12	1.58e-12	1.26e-12	2.63e-13
10.625	8.77e-12	1.20e-11	8.26e-12	4.64e-12	3.20e-12	1.72e-12	1.00e-12	6.98e-13
10.875	1.42e-11	1.19e-11	8.09e-12	4.60e-12	2.76e-12	9.10e-13	4.35e-13	3.65e-13
11.125	9.90e-12	1.18e-11	8.31e-12	5.43e-12	2.94e-12	1.16e-12	8.87e-13	2.72e-13
11.375	1.12e-11	1.13e-11	7.42e-12	4.56e-12	2.24e-12	1.36e-12	1.10e-12	2.95e-13
11.625	6.52e-12	1.12e-11	6.23e-12	3.07e-12	2.31e-12	1.34e-12	7.18e-13	2.59e-13
11.875	6.63e-12	1.04e-11	6.90e-12	3.35e-12	2.58e-12	7.63e-13	5.81e-13	2.37e-13
12.125	7.16e-12	1.13e-11	5.74e-12	3.39e-12	2.94e-12	7.17e-13	4.21e-13	2.33e-13
12.375	6.58e-12	1.12e-11	5.22e-12	3.35e-12	1.77e-12	7.63e-13	4.00e-13	8.38e-14
12.625	5.81e-12	8.42e-12	6.85e-12	2.57e-12	1.28e-12	8.79e-13	5.80e-13	1.38e-13
12.875	6.56e-12	1.19e-11	4.53e-12	2.52e-12	1.36e-12	6.32e-13	3.11e-13	8.39e-13
13.125	7.13e-12	7.90e-12	4.74e-12	2.44e-12	1.16e-12	7.73e-13	5.30e-13	7.12e-14
13.375	5.23e-12	7.60e-12	4.39e-12	2.48e-12	2.01e-12	4.76e-13	2.82e-13	1.02e-13
13.625	5.56e-12	8.40e-12	5.02e-12	2.01e-12	9.77e-13	7.60e-13	2.07e-13	1.69e-13
13.875	4.12e-12	7.19e-12	4.51e-12	2.30e-12	1.07e-12	7.17e-13	2.11e-13	6.28e-14
14.125	4.68e-12	1.12e-11	3.73e-12	2.23e-12	8.78e-13	3.74e-13	2.19e-13	6.70e-14
14.375	4.01e-12	6.79e-12	3.57e-12	1.86e-12	7.46e-13	4.38e-13	4.43e-13	6.89e-14
14.625	4.25e-12	5.69e-12	3.28e-12	2.21e-12	6.62e-13	6.13e-13	1.91e-13	8.06e-14
14.875	6.24e-12	5.72e-12	3.51e-12	1.71e-12	8.43e-13	3.54e-13	1.89e-13	6.65e-14

Table A.5: Continuation of Results for $M_{\mathrm{mQ}} = 0.1\ \mathrm{MeV}/c^2$.

	Angle (rad)							
Energy(GeV)	0.000250	0.000750	0.00125	0.00175	0.00225	0.00275	0.00325	0.00375
15.125	3.53e-12	5.34e-12	2.92e-12	1.58e-12	6.03e-13	9.36e-13	3.71e-13	7.22e-14
15.375	1.00e-11	5.75e-12	3.03e-12	1.24e-12	8.88e-13	8.77e-13	1.18e-13	1.21e-13
15.625	4.90e-12	6.53e-12	3.06e-12	1.25e-12	6.66e-13	2.90e-13	1.10e-13	3.10e-14
15.875	4.80e-12	4.79e-12	2.87e-12	1.38e-12	6.85e-13	2.91e-13	1.31e-13	4.66e-14
16.125	3.56e-12	4.51e-12	2.41e-12	1.27e-12	4.93e-13	4.64e-13	1.08e-13	5.41e-14
16.375	3.73e-12	5.01e-12	3.24e-12	8.67e-13	8.63e-13	4.66e-13	1.67e-13	6.17e-14
16.625	3.60e-12	4.92e-12	2.08e-12	1.76e-12	5.43e-13	5.20e-13	2.16e-13	4.08e-14
16.875	2.73e-12	3.33e-12	2.25e-12	9.93e-13	4.69e-13	1.71e-13	2.39e-13	5.35e-14
17.125	2.84e-12	4.60e-12	2.25e-12	1.01e-12	7.69e-13	2.36e-13	1.55e-13	4.49e-14
17.375	2.41e-12	3.45e-12	1.91e-12	1.01e-12	6.57e-13	2.64e-13	1.19e-13	4.71e-14
17.625	2.66e-12	5.16e-12	3.14e-12	1.05e-12	4.77e-13	5.13e-13	5.08e-14	1.78e-14
17.875	2.83e-12	3.42e-12	1.61e-12	7.57e-13	3.17e-13	2.17e-13	2.01e-13	9.28e-14
18.125	2.89e-12	3.05e-12	1.90e-12	8.27e-13	5.60e-13	3.72e-13	8.15e-14	1.38e-14
18.375	2.80e-12	3.12e-12	5.07e-12	6.45e-13	5.62e-13	4.04e-13	1.15e-13	2.19e-14
18.625	2.05e-12	3.09e-12	1.51e-12	4.42e-13	2.67e-13	5.71e-13	5.00e-14	3.04e-14
18.875	3.25e-12	2.84e-12	1.22e-12	4.70e-13	5.96e-13	2.10e-13	9.68e-14	1.87e-14
19.125	1.93e-12	2.60e-12	1.37e-12	9.40e-13	3.19e-13	1.35e-13	4.63e-14	4.22e-14
19.375	1.95e-12	2.77e-12	1.19e-12	8.92e-13	3.20e-13	6.80e-14	6.13e-14	1.80e-14
19.625	1.49e-12	2.36e-12	1.08e-12	4.48e-13	2.27e-13	7.55e-14	8.65e-14	1.26e-14
19.875	2.12e-12	2.31e-12	1.77e-12	5.16e-13	1.42e-13	1.04e-13	5.40e-14	1.00e-14
20.125	2.00e-12	1.85e-12	1.21e-12	1.60e-12	2.92e-12	1.81e-13	6.68e-14	3.01e-14
20.375	1.76e-12	2.12e-12	1.09e-12	4.31e-13	5.12e-13	1.45e-13	4.25e-14	1.27e-14
20.625	2.13e-12	2.75e-12	5.81e-12	5.84e-13	9.17e-14	2.23e-13	6.52e-14	2.60e-14
20.875	1.68e-12	1.35e-12	1.49e-12	5.94e-13	2.89e-13	9.89e-14	3.25e-14	1.15e-14
21.125	9.92e-13	1.62e-12	9.26e-13	3.64e-13	3.30e-13	1.38e-13	4.81e-14	6.81e-15
21.375	1.36e-12	1.68e-12	1.21e-12	6.68e-13	1.79e-13	1.45e-13	2.36e-14	3.60e-15
21.625	1.37e-12	2.21e-12	8.10e-13	2.05e-13	1.96e-13	9.80e-14	2.49e-14	8.90e-15
21.875	1.56e-12	1.64e-12	1.06e-12	3.70e-13	2.44e-13	8.18e-14	1.58e-14	2.79e-15
22.125	1.07e-12	1.24e-12	8.58e-13	2.77e-13	2.77e-13	6.26e-14	2.68e-14	1.58e-15
22.375	2.01e-12	1.00e-12	6.60e-13	3.66e-13	2.45e-13	4.20e-14	2.47e-14	7.69e-15
22.625	7.00e-13	1.64e-12	3.68e-12	2.75e-13	1.72e-13	3.32e-14	4.26e-14	5.25e-15
22.875	5.15e-13	8.23e-13	4.81e-13	1.78e-13	1.15e-12	3.76e-14	3.97e-14	1.21e-14
23.125	1.08e-12	1.21e-12	6.44e-13	6.16e-13	4.17e-13	2.25e-14	4.42e-14	3.55e-15
23.375	7.85e-13	7.25e-13	2.77e-13	2.73e-13	1.72e-12	6.51e-14	7.22e-14	1.88e-14
23.625	6.56e-13	1.82e-12	5.99e-13	2.14e-13	1.54e-13	2.59e-14	1.37e-14	5.81e-15
23.875	5.28e-13	4.03e-12	3.15e-13	1.87e-13	9.34e-13	3.19e-14	6.62e-15	1.07e-14
24.125	3.86e-13	8.78e-13	4.06e-13	7.53e-13	1.95e-13	3.48e-14	1.47e-13	1.32e-14
24.375	5.27e-13	5.71e-13	3.24e-13	2.20e-13	1.57e-13	1.17e-13	3.20e-14	4.46e-14
24.625	4.95e-13	3.78e-13	8.87e-13	1.85e-13	4.15e-14	1.14e-13	8.71e-15	1.22e-14
24.875	4.91e-13	4.18e-13	6.91e-13	2.50e-13	1.98e-13	3.01e-14	1.56e-14	3.33e-15
25.125	2.67e-13	3.74e-13	2.22e-13	2.46e-13	1.64e-13	2.87e-14	8.99e-15	3.76e-15
25.375	3.02e-13	6.05e-13	3.94e-13	2.02e-13	1.23e-13	2.06e-14	2.57e-14	2.57e-14
25.625	4.78e-13	3.25e-13	3.06e-13	1.33e-13	1.74e-13	2.56e-13	4.08e-15	3.59e-15
25.875	2.79e-13	2.82e-13	1.23e-13	8.87e-14	6.96e-14	1.72e-14	7.57e-15	2.01e-14
26.125	1.19e-13	4.10e-13	1.37e-13	7.24e-14	5.48e-14	2.64e-14	1.53e-14	1.60e-15
26.375	1.83e-13	2.78e-13	1.46e-13	5.64e-14	2.58e-14	3.76e-14	7.46e-15	3.75e-15
26.625	9.40e-14	1.86e-13	1.17e-13	3.96e-14	2.07e-14	1.68e-14	4.41e-14	6.73e-16
26.875	1.82e-13	2.03e-13	1.34e-13	6.55e-14	1.17e-13	2.91e-14	1.02e-14	2.34e-16
27.125	4.63e-14	2.68e-13	1.81e-13	5.06e-14	1.90e-14	1.32e-14	1.82e-14	2.78e-15
27.375	3.69e-14	7.01e-14	2.86e-14	4.75e-14	1.67e-14	1.24e-14	2.46e-15	0.00
27.625	2.17e-14	7.71e-14	2.27e-13	2.86e-14	2.54e-14	1.50e-14	3.18e-16	9.74e-16
27.875	3.95e-14	7.46e-14	4.71e-13	2.71e-13	7.72e-15	4.50e-15	9.00e-16	2.44e-16
28.125	3.25e-14	6.92e-14	1.08e-14	1.91e-14	2.14e-14	6.41e-16	1.67e-16	1.68e-15
28.375	8.80e-15	3.98e-14	3.80e-14	1.92e-14	8.39e-15	4.00e-15	0.00	0.00
28.625	7.85e-15	6.70e-15	1.95e-14	2.85e-12	2.57e-14	1.10e-14	6.30e-16	0.00
28.875	2.13e-15	7.29e-15	6.73e-15	1.76e-14	7.64e-15	1.14e-15	0.00	0.00
29.125	8.75e-17	1.46e-15	3.96e-16	5.76e-16	1.00e-14	0.00	0.00	0.00
29.375	0.00	2.58e-15	0.00	1.41e-15	0.00	0.00	0.00	0.00
29.625	0.00	0.00	0.00	0.00	0.00	0.00	0.00	0.00
29.875	0.00	0.00	0.00	0.00	0.00	0.00	0.00	0.00

Table A.6: Results of Production Monte Carlo for $M_{\mathrm{mQ}} = 1$ MeV/c^2.

	Angle (rad)							
Energy(GeV)	0.000250	0.000750	0.00125	0.00175	0.00225	0.00275	0.00325	0.00375
0.125	3.93e-13	1.05e-12	1.83e-12	2.34e-12	3.40e-12	3.30e-12	5.04e-12	5.02e-12
0.375	1.11e-12	6.58e-12	5.13e-12	1.00e-11	1.31e-11	1.43e-11	8.76e-12	1.18e-11
0.625	2.50e-12	6.47e-12	7.36e-12	1.01e-11	8.60e-12	1.12e-11	1.32e-11	1.36e-11
0.875	2.59e-12	5.46e-12	1.07e-11	8.94e-12	1.22e-11	1.17e-11	1.07e-11	1.76e-11
1.125	3.12e-12	5.55e-12	7.31e-12	9.01e-12	8.20e-12	8.74e-12	1.27e-11	8.16e-12
1.375	2.10e-12	6.38e-12	6.40e-12	7.11e-12	1.23e-11	7.66e-12	2.11e-11	7.85e-12
1.625	2.28e-12	5.64e-12	6.41e-12	6.49e-12	6.07e-12	8.39e-12	6.94e-12	5.34e-12
1.875	3.18e-12	5.58e-12	7.23e-12	6.20e-12	5.48e-12	2.11e-11	6.12e-12	3.90e-12
2.125	2.46e-12	4.52e-12	4.74e-12	5.85e-12	4.68e-12	8.85e-12	3.97e-12	4.28e-12
2.375	2.26e-12	4.37e-12	4.61e-12	5.04e-12	4.79e-12	3.32e-12	4.17e-12	3.61e-12
2.625	2.14e-12	4.51e-12	4.01e-12	1.76e-11	4.15e-12	3.23e-12	4.38e-12	2.81e-12
2.875	2.67e-12	3.53e-12	4.78e-12	3.55e-12	4.30e-12	2.56e-12	3.04e-12	2.80e-12
3.125	2.11e-12	3.92e-12	4.53e-12	3.62e-12	3.27e-12	1.69e-11	3.98e-12	3.35e-12
3.375	2.18e-12	7.89e-12	6.46e-12	4.10e-12	3.17e-12	2.52e-12	2.50e-12	1.67e-12
3.625	2.11e-12	3.60e-12	3.72e-12	2.75e-12	2.78e-12	1.97e-12	2.64e-12	1.18e-12
3.875	3.48e-12	2.77e-12	3.29e-12	2.99e-12	2.05e-12	2.23e-12	2.09e-12	1.09e-12
4.125	1.89e-12	3.25e-12	6.79e-12	2.99e-12	3.11e-12	1.48e-12	1.78e-12	6.53e-13
4.375	1.68e-12	3.29e-12	2.75e-12	2.31e-12	1.71e-12	1.24e-12	1.13e-12	6.55e-13
4.625	2.26e-12	2.65e-12	2.29e-12	2.72e-12	2.22e-11	1.08e-12	1.85e-12	7.77e-13
4.875	1.65e-12	4.51e-12	3.06e-12	2.34e-12	2.00e-12	1.40e-12	6.13e-13	4.18e-13
5.125	1.68e-12	2.48e-12	3.30e-12	1.70e-12	1.41e-12	1.10e-12	5.47e-13	4.60e-13
5.375	2.04e-12	5.45e-12	2.07e-12	1.48e-12	1.03e-12	1.17e-12	4.54e-13	3.15e-13
5.625	1.72e-12	2.58e-12	2.00e-12	1.82e-12	1.17e-12	1.25e-12	3.78e-13	3.02e-13
5.875	1.13e-12	2.21e-12	2.03e-12	1.46e-12	1.03e-12	6.07e-13	4.37e-13	2.73e-13
6.125	1.22e-12	1.97e-12	1.67e-12	1.15e-12	9.87e-13	7.40e-13	3.52e-13	2.81e-13
6.375	1.17e-12	1.82e-12	1.46e-12	1.57e-12	1.72e-12	8.09e-13	2.99e-13	2.87e-13
6.625	1.20e-12	1.99e-12	1.45e-12	1.00e-12	8.96e-13	5.71e-13	2.51e-13	2.17e-13
6.875	1.06e-12	1.55e-12	1.95e-12	1.40e-12	5.81e-13	3.27e-13	5.49e-13	1.51e-13
7.125	1.23e-12	2.77e-12	1.26e-12	1.20e-12	1.14e-12	2.75e-13	2.14e-13	1.35e-13
7.375	1.32e-12	1.58e-12	1.19e-12	8.65e-13	6.18e-13	4.03e-13	5.21e-13	1.07e-13
7.625	1.18e-12	1.52e-12	1.09e-12	7.70e-13	5.49e-13	3.64e-13	1.77e-13	1.07e-13
7.875	1.27e-12	2.03e-12	1.14e-12	7.73e-13	1.07e-12	2.77e-13	3.99e-13	2.68e-13
8.125	1.22e-12	1.74e-12	1.00e-12	8.74e-13	3.82e-13	2.87e-13	1.19e-13	4.42e-14
8.375	8.88e-13	1.49e-12	1.35e-12	6.00e-13	1.09e-12	2.19e-13	2.96e-13	6.22e-14
8.625	1.21e-12	1.27e-12	1.00e-12	1.04e-12	4.11e-13	2.88e-13	1.06e-13	1.07e-13
8.875	9.66e-13	1.14e-12	7.52e-13	9.51e-13	3.01e-13	1.96e-13	1.02e-13	3.58e-14
9.125	1.06e-12	1.91e-12	1.07e-12	6.45e-13	3.32e-13	2.04e-13	1.21e-13	4.27e-14
9.375	8.45e-13	1.33e-12	8.67e-13	4.83e-13	4.18e-13	1.41e-13	7.78e-14	3.16e-14
9.625	9.01e-13	1.17e-12	8.16e-13	6.02e-13	2.89e-13	2.90e-13	5.37e-14	3.05e-14
9.875	7.85e-13	1.49e-12	1.23e-12	4.62e-13	2.00e-13	1.19e-13	5.56e-14	4.91e-14
10.125	8.08e-13	1.09e-12	7.39e-13	5.70e-13	3.30e-13	2.06e-13	5.91e-14	4.03e-13
10.375	9.52e-13	1.29e-12	6.84e-13	3.18e-13	3.33e-13	1.23e-13	5.36e-14	3.32e-14
10.625	6.93e-13	1.26e-12	5.21e-13	5.37e-13	2.80e-13	1.05e-13	7.66e-14	2.29e-14
10.875	7.64e-13	8.47e-13	6.38e-13	3.41e-13	2.44e-13	1.36e-13	4.54e-14	4.61e-14
11.125	9.47e-13	1.44e-12	5.59e-13	3.79e-13	4.19e-13	2.01e-13	7.22e-14	1.78e-14
11.375	6.05e-13	8.55e-13	6.39e-13	6.58e-13	1.48e-13	9.32e-14	1.08e-13	4.27e-14
11.625	8.55e-13	1.10e-12	5.67e-13	3.21e-13	1.74e-13	1.25e-13	9.70e-14	1.42e-14
11.875	7.91e-13	7.12e-13	7.18e-13	2.47e-13	1.90e-13	6.49e-14	3.49e-14	2.64e-14
12.125	6.86e-13	9.10e-13	4.96e-13	2.26e-13	1.60e-13	6.55e-14	4.05e-14	1.63e-14
12.375	7.54e-13	1.16e-12	3.99e-13	2.51e-13	1.84e-13	5.18e-14	2.20e-14	6.70e-15
12.625	5.35e-13	9.02e-13	4.80e-13	5.12e-13	1.29e-13	1.91e-13	2.15e-14	2.11e-14
12.875	4.75e-13	8.04e-13	4.74e-13	2.73e-13	1.33e-13	6.28e-14	6.21e-14	6.06e-15
13.125	4.15e-13	1.29e-12	4.54e-13	1.97e-13	1.90e-13	4.81e-14	1.91e-14	7.70e-15
13.375	5.38e-13	7.47e-13	4.49e-13	2.17e-13	2.41e-13	4.18e-14	2.66e-14	9.85e-15
13.625	6.33e-13	7.98e-13	3.58e-13	1.52e-13	6.72e-14	4.39e-14	5.56e-14	8.57e-15
13.875	4.32e-13	7.44e-13	3.74e-13	1.68e-13	6.86e-14	3.73e-14	2.12e-14	5.69e-15
14.125	4.54e-13	8.94e-13	3.77e-13	1.53e-13	9.47e-14	4.04e-14	1.35e-14	5.05e-14
14.375	3.96e-13	5.20e-13	3.95e-13	1.37e-13	8.09e-14	3.61e-14	3.17e-14	2.74e-15
14.625	4.46e-13	4.92e-13	2.73e-13	1.64e-13	4.57e-14	6.00e-14	4.79e-14	3.63e-15
14.875	3.83e-13	6.02e-13	3.99e-13	1.42e-13	6.16e-14	4.02e-14	9.89e-15	1.04e-14

Table A.7: Continuation of Results for $M_{\mathrm{mQ}} = 1\ \mathrm{MeV}/c^2$.

	Angle (rad)							
Energy(GeV)	0.000250	0.000750	0.00125	0.00175	0.00225	0.00275	0.00325	0.00375
15.125	4.18e-13	5.35e-13	3.49e-13	2.05e-13	3.49e-14	2.76e-14	1.16e-14	7.60e-15
15.375	7.12e-13	4.88e-13	2.93e-13	1.30e-13	6.11e-14	2.12e-14	1.02e-14	2.62e-15
15.625	5.88e-13	6.31e-13	2.19e-13	1.22e-13	7.33e-14	1.91e-14	1.58e-14	2.71e-15
15.875	4.42e-13	5.11e-13	4.98e-13	8.67e-14	7.82e-14	2.10e-14	1.55e-14	1.88e-15
16.125	3.29e-13	4.59e-13	3.29e-13	8.51e-14	9.06e-14	3.40e-13	1.06e-14	5.74e-15
16.375	4.80e-13	5.86e-13	2.78e-13	2.23e-13	5.43e-14	2.74e-14	9.14e-15	2.49e-15
16.625	4.59e-13	3.38e-13	1.56e-13	1.66e-13	7.92e-14	5.17e-14	2.48e-14	1.89e-15
16.875	3.89e-13	6.54e-13	1.60e-13	2.25e-13	5.29e-14	1.20e-14	7.08e-14	6.34e-15
17.125	2.87e-13	3.21e-13	2.55e-13	7.75e-14	8.56e-14	1.78e-14	3.13e-14	2.96e-15
17.375	2.87e-13	3.31e-13	1.67e-13	5.76e-14	5.32e-14	1.96e-14	5.03e-15	2.92e-15
17.625	2.60e-13	2.94e-13	1.97e-13	9.15e-14	4.58e-14	1.17e-14	8.02e-15	5.52e-15
17.875	2.54e-13	2.79e-13	2.26e-13	5.73e-14	2.98e-14	1.61e-13	1.03e-14	1.84e-15
18.125	3.29e-13	4.37e-13	2.34e-13	6.45e-14	2.89e-14	5.32e-14	4.47e-15	1.69e-15
18.375	2.33e-13	3.13e-13	1.47e-13	8.01e-14	2.42e-14	2.47e-14	2.43e-14	1.14e-15
18.625	1.96e-13	8.37e-13	1.25e-13	4.76e-14	4.73e-14	7.21e-14	2.35e-15	1.44e-14
18.875	4.97e-13	2.24e-13	1.24e-13	5.46e-14	2.45e-14	1.71e-14	7.58e-15	2.49e-15
19.125	2.17e-13	2.67e-13	1.03e-13	4.29e-14	1.61e-14	1.09e-14	5.28e-15	3.47e-15
19.375	1.79e-13	2.71e-13	7.99e-14	6.19e-14	6.72e-14	1.48e-14	6.05e-15	1.30e-15
19.625	2.04e-13	2.26e-13	1.32e-13	6.67e-14	2.14e-14	1.07e-14	5.24e-15	1.63e-15
19.875	3.16e-13	2.02e-13	1.25e-13	4.17e-14	8.33e-14	1.41e-14	5.68e-15	6.98e-16
20.125	2.06e-13	2.20e-13	7.58e-14	4.16e-14	3.11e-14	1.96e-14	6.61e-15	1.78e-15
20.375	1.64e-13	2.41e-13	1.89e-13	3.08e-13	3.01e-14	9.21e-15	1.51e-14	2.70e-16
20.625	2.71e-13	2.15e-13	8.45e-14	5.97e-14	1.20e-13	6.33e-15	5.40e-15	5.36e-16
20.875	1.48e-13	3.41e-13	1.25e-13	4.07e-14	1.12e-14	3.18e-14	4.16e-15	9.49e-16
21.125	1.18e-13	1.48e-13	8.55e-14	3.95e-14	2.04e-14	2.35e-14	5.89e-15	7.67e-16
21.375	1.12e-13	1.10e-13	7.37e-14	3.97e-14	1.35e-14	1.05e-14	4.52e-15	1.92e-15
21.625	1.58e-13	1.51e-13	9.49e-14	4.06e-14	1.90e-14	1.76e-14	2.24e-15	5.06e-16
21.875	2.23e-13	5.20e-13	4.89e-14	3.02e-14	4.03e-14	2.24e-15	2.42e-15	1.20e-16
22.125	1.49e-13	1.58e-13	7.77e-14	3.53e-14	3.38e-14	6.61e-15	1.69e-15	2.21e-16
22.375	3.53e-13	9.01e-14	6.99e-14	2.19e-14	1.29e-14	6.20e-15	2.19e-15	4.76e-16
22.625	1.16e-13	1.26e-13	7.87e-13	3.64e-14	1.15e-14	6.05e-15	1.83e-15	3.47e-16
22.875	5.26e-14	1.18e-13	6.60e-14	1.95e-14	2.48e-14	3.59e-15	2.27e-15	1.45e-15
23.125	9.56e-14	9.29e-14	7.50e-14	1.25e-14	4.39e-14	1.95e-15	1.77e-15	6.00e-16
23.375	1.60e-13	8.41e-14	3.49e-14	1.91e-14	3.40e-14	2.16e-15	7.77e-16	2.32e-15
23.625	7.70e-14	6.11e-14	2.47e-14	3.75e-14	1.80e-14	2.40e-15	2.32e-15	2.69e-16
23.875	3.82e-14	5.27e-14	2.26e-14	1.43e-14	1.35e-13	2.39e-15	2.43e-15	1.17e-15
24.125	5.45e-14	2.90e-13	6.06e-14	1.59e-14	3.63e-14	3.95e-15	4.95e-15	3.08e-15
24.375	7.19e-14	1.87e-13	2.87e-14	1.24e-13	2.77e-14	1.89e-15	4.47e-15	2.82e-14
24.625	3.50e-14	5.06e-14	5.58e-14	1.32e-14	6.17e-15	1.11e-14	3.16e-15	1.13e-16
24.875	4.46e-14	3.74e-14	1.03e-13	1.02e-14	5.38e-15	1.07e-14	6.69e-16	5.70e-16
25.125	2.31e-14	4.68e-14	4.14e-14	1.82e-14	4.42e-14	1.91e-15	3.81e-16	3.76e-16
25.375	3.49e-14	2.72e-14	1.85e-14	1.85e-14	2.68e-14	1.95e-15	5.91e-16	1.84e-15
25.625	2.94e-14	5.61e-14	2.65e-14	8.48e-15	3.54e-14	4.55e-15	1.56e-15	3.40e-17
25.875	2.49e-14	2.13e-14	5.55e-14	1.49e-14	6.17e-15	1.81e-15	7.10e-16	1.88e-16
26.125	1.44e-14	1.75e-14	1.81e-14	4.22e-15	3.04e-15	4.62e-16	1.53e-15	3.83e-16
26.375	1.64e-14	4.54e-14	1.27e-14	6.42e-15	3.78e-15	3.46e-15	1.06e-15	2.04e-16
26.625	9.50e-15	1.49e-14	8.14e-15	3.11e-15	1.45e-15	1.57e-15	5.30e-15	6.77e-16
26.875	2.35e-14	1.51e-14	1.45e-14	5.42e-15	1.26e-14	1.89e-15	1.47e-15	4.40e-17
27.125	5.33e-15	3.21e-14	1.27e-14	9.66e-15	2.20e-15	4.44e-15	4.10e-16	3.98e-16
27.375	3.10e-15	6.73e-15	8.80e-15	5.09e-15	1.10e-15	1.12e-16	6.09e-16	1.46e-18
27.625	2.82e-15	4.42e-15	1.55e-14	9.92e-16	2.44e-15	2.64e-15	2.02e-17	3.82e-19
27.875	4.07e-15	2.70e-14	2.44e-15	7.36e-15	7.65e-16	2.51e-16	1.95e-16	7.44e-17
28.125	4.08e-16	6.30e-15	1.28e-15	1.26e-15	6.55e-16	2.99e-16	5.80e-17	1.80e-16
28.375	3.80e-16	1.07e-15	4.94e-15	1.89e-15	8.21e-16	1.49e-16	2.59e-18	0.00
28.625	1.03e-15	4.03e-16	4.26e-15	5.81e-14	2.15e-16	1.44e-16	1.53e-16	0.00
28.875	2.21e-16	2.00e-16	6.96e-16	9.30e-16	7.56e-16	1.13e-16	1.94e-17	0.00
29.125	2.50e-17	3.27e-16	5.36e-17	1.00e-16	1.08e-15	0.00	0.00	0.00
29.375	0.00	8.35e-17	0.00	2.55e-17	0.00	0.00	0.00	0.00
29.625	0.00	0.00	0.00	0.00	0.00	0.00	0.00	0.00
29.875	0.00	0.00	0.00	0.00	0.00	0.00	0.00	0.00

Table A.8: Results of Production Monte Carlo for $M_{\mathrm{mQ}} = 10$ MeV/c^2.

	Angle (rad)							
Energy(GeV)	0.000250	0.000750	0.00125	0.00175	0.00225	0.00275	0.00325	0.00375
0.125	1.20e-16	2.56e-16	4.43e-16	8.75e-16	5.41e-16	8.77e-16	1.24e-15	2.00e-15
0.375	6.18e-16	3.49e-15	1.10e-14	4.38e-15	1.02e-14	7.39e-15	4.22e-14	1.66e-14
0.625	1.43e-15	2.10e-14	8.19e-15	1.60e-14	1.67e-14	2.32e-14	4.36e-14	2.81e-14
0.875	2.01e-15	6.72e-15	9.88e-15	1.89e-14	2.14e-14	2.65e-14	3.55e-14	6.04e-14
1.125	2.58e-15	9.34e-15	1.70e-14	2.41e-14	2.85e-14	7.44e-14	2.99e-14	4.01e-14
1.375	2.61e-14	1.02e-14	2.34e-14	3.72e-14	3.04e-14	3.61e-14	4.28e-14	6.56e-14
1.625	3.66e-15	8.67e-15	2.58e-14	3.39e-14	3.34e-14	3.50e-14	4.01e-14	5.42e-14
1.875	3.38e-15	1.59e-14	2.95e-14	3.00e-14	3.82e-14	3.83e-14	4.52e-14	3.70e-14
2.125	3.47e-15	1.21e-14	1.98e-14	4.36e-14	5.74e-14	4.76e-14	9.68e-14	6.07e-14
2.375	5.76e-15	3.30e-14	3.21e-14	2.79e-14	3.43e-14	4.70e-14	3.50e-14	1.39e-13
2.625	1.23e-14	1.34e-14	2.02e-14	6.35e-14	3.03e-14	3.28e-14	4.40e-14	2.67e-14
2.875	5.25e-15	4.12e-14	1.84e-14	6.91e-14	4.67e-14	3.58e-14	8.23e-14	3.41e-14
3.125	9.89e-15	1.51e-14	2.04e-14	2.88e-14	4.25e-14	3.47e-14	2.38e-14	2.24e-14
3.375	6.89e-15	4.31e-14	1.59e-14	3.04e-14	4.28e-14	2.45e-14	2.95e-14	3.57e-14
3.625	1.73e-14	1.30e-14	2.34e-14	2.24e-14	3.97e-14	3.78e-14	3.95e-14	2.34e-14
3.875	5.54e-15	1.48e-14	2.48e-14	2.92e-14	4.21e-14	2.27e-14	2.38e-14	2.06e-14
4.125	5.35e-15	2.08e-14	2.66e-14	2.19e-14	1.09e-13	2.29e-14	2.24e-14	1.22e-14
4.375	5.44e-15	1.43e-14	2.92e-14	2.01e-14	3.64e-14	2.03e-14	1.69e-14	1.13e-14
4.625	5.24e-15	1.49e-14	3.83e-14	2.02e-14	4.47e-14	1.64e-14	2.16e-14	2.13e-14
4.875	8.89e-15	2.00e-14	2.53e-14	2.49e-14	3.44e-14	2.31e-14	1.44e-14	2.01e-14
5.125	5.97e-15	1.66e-14	2.39e-14	4.77e-14	2.01e-14	6.57e-13	8.36e-15	1.12e-14
5.375	4.71e-15	2.33e-14	2.06e-14	1.58e-14	1.47e-14	1.55e-14	8.91e-15	7.63e-15
5.625	5.01e-15	1.32e-14	1.75e-14	1.87e-14	2.08e-14	2.07e-14	1.09e-14	8.26e-15
5.875	5.71e-15	1.55e-14	2.29e-14	1.85e-14	2.23e-14	1.12e-14	1.33e-14	6.79e-15
6.125	1.15e-14	1.46e-14	1.46e-14	1.70e-14	1.76e-14	4.48e-14	7.27e-15	3.94e-15
6.375	9.47e-15	1.47e-14	1.50e-14	1.53e-14	1.56e-14	9.65e-14	8.78e-15	8.61e-15
6.625	6.22e-15	1.87e-14	3.48e-14	1.42e-14	2.63e-14	1.53e-14	5.51e-15	3.38e-14
6.875	5.08e-15	1.42e-14	1.99e-14	2.38e-14	1.19e-14	4.17e-14	4.97e-15	3.83e-15
7.125	2.04e-14	1.91e-14	2.06e-14	1.73e-14	2.49e-14	5.52e-14	8.03e-15	3.80e-15
7.375	6.04e-15	2.64e-14	1.40e-14	1.58e-14	1.90e-14	7.22e-15	4.40e-15	6.39e-15
7.625	7.46e-15	1.21e-14	1.41e-14	1.34e-14	1.12e-14	1.19e-14	4.25e-15	3.20e-15
7.875	5.61e-15	1.43e-14	2.95e-14	1.59e-14	1.24e-14	4.64e-15	4.19e-15	3.68e-15
8.125	5.24e-15	1.22e-13	1.66e-14	9.92e-15	4.38e-14	4.01e-15	2.94e-15	4.56e-15
8.375	5.98e-15	1.05e-14	3.82e-14	1.28e-14	2.78e-14	4.19e-15	4.94e-15	8.31e-15
8.625	5.72e-15	1.43e-14	1.16e-14	8.79e-15	1.19e-14	4.75e-15	2.03e-15	2.71e-15
8.875	5.52e-15	1.91e-14	1.58e-14	9.26e-15	6.75e-15	3.98e-15	3.79e-15	2.29e-15
9.125	5.77e-15	1.25e-14	1.53e-14	1.49e-14	1.30e-14	5.79e-15	1.97e-15	1.83e-15
9.375	7.98e-15	1.08e-14	2.07e-14	1.24e-14	6.06e-15	4.44e-15	3.36e-15	1.93e-15
9.625	1.41e-14	1.55e-14	1.11e-14	1.25e-14	1.97e-14	3.81e-15	2.25e-15	2.42e-15
9.875	7.19e-15	1.05e-14	1.02e-14	3.42e-14	1.21e-14	2.33e-15	5.24e-15	1.92e-15
10.125	5.49e-15	1.15e-14	9.26e-15	6.96e-15	1.47e-14	4.77e-15	1.51e-14	7.23e-16
10.375	7.70e-15	1.23e-14	5.71e-14	6.00e-15	3.80e-15	3.42e-15	1.59e-15	9.82e-16
10.625	7.19e-15	1.11e-14	2.82e-14	6.02e-15	6.20e-15	3.19e-15	2.95e-15	1.14e-15
10.875	3.68e-15	1.18e-14	8.61e-15	6.10e-15	2.98e-15	3.88e-15	1.61e-14	8.93e-16
11.125	4.33e-15	1.21e-14	9.89e-15	1.47e-14	4.91e-15	4.40e-15	5.33e-15	4.05e-16
11.375	4.60e-15	9.70e-15	1.03e-14	7.03e-15	3.09e-15	2.22e-15	1.28e-15	1.51e-15
11.625	5.80e-15	1.09e-14	8.30e-15	9.17e-15	2.58e-15	3.76e-15	4.71e-16	1.06e-15
11.875	5.22e-15	1.69e-14	6.88e-15	6.45e-15	3.82e-15	1.99e-15	5.47e-16	4.75e-16
12.125	5.35e-15	9.34e-15	1.30e-14	6.01e-15	3.19e-15	2.72e-15	1.17e-15	2.09e-15
12.375	3.75e-15	1.25e-14	5.85e-15	4.66e-15	2.22e-15	4.47e-15	6.80e-16	5.08e-16
12.625	4.17e-15	1.02e-14	1.41e-14	4.33e-15	5.32e-15	1.47e-15	4.41e-15	3.39e-16
12.875	6.45e-15	9.59e-15	8.99e-15	4.99e-15	4.02e-15	1.63e-15	6.41e-16	2.73e-16
13.125	5.51e-15	1.29e-14	8.41e-15	5.50e-15	2.72e-15	1.71e-15	7.14e-16	1.99e-16
13.375	5.69e-15	7.05e-15	5.04e-15	2.04e-14	4.20e-15	1.34e-15	9.21e-16	2.95e-16
13.625	9.60e-15	6.62e-15	7.75e-15	3.04e-15	3.70e-15	9.85e-16	1.60e-15	3.70e-16
13.875	4.51e-15	8.25e-15	4.45e-15	3.40e-15	1.22e-15	6.63e-16	2.68e-16	4.29e-16
14.125	4.45e-15	9.34e-15	9.78e-15	2.50e-15	9.48e-16	1.31e-15	1.85e-15	1.48e-15
14.375	3.36e-15	1.10e-14	6.40e-15	2.29e-15	1.56e-15	8.46e-16	5.40e-16	3.37e-16
14.625	4.43e-15	7.72e-15	4.72e-15	2.50e-15	1.33e-15	1.74e-15	3.85e-16	2.24e-16
14.875	5.72e-15	1.34e-14	4.53e-15	3.11e-15	1.36e-15	2.79e-15	4.42e-16	1.73e-16

Table A.9: Continuation of Results for $M_{\mathrm{mQ}} = 10$ MeV/c^2.

	Angle (rad)							
Energy(GeV)	0.000250	0.000750	0.00125	0.00175	0.00225	0.00275	0.00325	0.00375
15.125	8.99e-15	6.95e-15	6.75e-15	4.09e-15	1.88e-15	5.90e-16	4.42e-16	1.88e-16
15.375	3.85e-15	4.74e-15	9.40e-15	1.69e-15	1.17e-15	3.39e-16	3.17e-16	8.98e-17
15.625	5.26e-15	1.48e-14	4.11e-15	3.44e-15	1.90e-15	1.13e-15	1.59e-15	1.65e-16
15.875	3.73e-15	1.02e-14	3.71e-15	1.76e-15	1.33e-15	5.00e-16	3.80e-16	1.29e-16
16.125	6.01e-15	7.14e-15	4.79e-15	6.57e-15	6.41e-16	9.03e-16	3.77e-15	1.98e-16
16.375	4.03e-15	9.97e-15	3.78e-15	2.52e-15	5.48e-16	2.24e-16	1.51e-16	2.63e-16
16.625	2.61e-15	8.18e-15	5.39e-15	1.44e-15	6.09e-16	6.58e-16	2.48e-16	5.94e-17
16.875	1.50e-14	4.33e-15	2.98e-15	3.79e-15	1.58e-15	1.41e-15	2.42e-16	9.82e-17
17.125	3.34e-15	4.23e-15	1.76e-14	2.19e-15	1.52e-15	4.65e-16	2.18e-16	5.55e-17
17.375	8.53e-15	3.70e-15	3.08e-15	1.53e-15	8.47e-16	5.76e-16	9.64e-17	1.09e-15
17.625	1.50e-14	6.50e-15	2.19e-15	1.17e-15	5.33e-16	3.01e-16	3.37e-16	1.22e-16
17.875	2.38e-15	2.81e-15	4.77e-15	1.83e-15	5.93e-16	3.05e-16	1.21e-15	4.70e-17
18.125	2.15e-15	4.61e-15	1.92e-15	1.15e-15	3.38e-16	3.44e-15	6.87e-17	2.96e-17
18.375	3.81e-15	4.94e-15	4.40e-15	1.50e-15	4.41e-16	4.71e-16	3.16e-16	2.73e-17
18.625	2.22e-15	5.04e-15	1.61e-15	1.22e-15	4.53e-16	9.44e-16	2.20e-16	2.86e-17
18.875	2.18e-15	3.45e-15	1.77e-15	4.57e-15	4.56e-16	1.54e-16	8.26e-17	2.38e-17
19.125	3.03e-15	2.96e-15	2.89e-15	8.37e-16	5.06e-16	1.30e-16	1.55e-16	6.10e-17
19.375	3.67e-15	6.56e-15	1.67e-15	6.13e-16	3.70e-16	7.84e-16	2.91e-16	2.78e-17
19.625	2.11e-15	2.19e-15	4.46e-15	2.23e-15	3.63e-16	2.36e-16	4.93e-17	2.01e-16
19.875	2.35e-15	4.43e-15	8.92e-16	6.16e-16	3.56e-16	8.07e-17	1.03e-15	2.82e-17
20.125	4.92e-15	2.78e-15	2.24e-14	1.18e-15	1.44e-15	2.11e-16	8.10e-17	2.08e-17
20.375	2.06e-15	1.95e-15	1.17e-15	1.21e-15	8.96e-16	3.74e-16	2.70e-17	6.90e-17
20.625	1.24e-15	2.46e-15	2.22e-15	7.63e-16	4.06e-15	1.71e-16	6.68e-17	1.09e-17
20.875	1.38e-15	4.81e-15	1.92e-15	7.91e-16	3.20e-16	1.48e-16	4.88e-17	7.69e-18
21.125	9.64e-16	2.86e-15	1.25e-15	6.98e-16	3.19e-15	1.24e-16	3.73e-17	6.78e-17
21.375	1.99e-15	1.77e-15	2.38e-15	2.15e-15	3.06e-16	7.27e-17	3.18e-17	2.27e-17
21.625	1.81e-15	1.78e-15	1.84e-15	3.90e-16	1.73e-16	6.67e-17	3.24e-17	9.75e-18
21.875	1.82e-15	1.28e-14	1.26e-15	6.71e-16	2.77e-16	2.29e-16	2.32e-17	1.27e-17
22.125	4.29e-15	1.38e-15	8.97e-16	3.57e-16	8.15e-16	1.14e-16	1.06e-16	1.35e-17
22.375	1.03e-15	1.17e-15	1.09e-15	7.40e-16	1.96e-16	6.58e-17	5.01e-17	5.00e-18
22.625	2.85e-15	2.27e-15	1.49e-15	9.42e-16	1.81e-16	1.01e-16	2.12e-17	2.56e-17
22.875	8.33e-16	9.27e-16	1.03e-15	3.64e-16	1.18e-15	2.09e-16	1.24e-17	1.24e-17
23.125	1.02e-15	9.74e-16	9.50e-16	5.62e-16	1.28e-16	2.97e-17	2.84e-17	1.43e-17
23.375	1.46e-14	1.32e-15	5.54e-16	3.52e-16	1.13e-16	8.00e-17	3.91e-17	4.74e-17
23.625	8.93e-16	9.93e-16	7.23e-16	5.36e-16	1.60e-16	3.81e-17	1.29e-17	1.10e-17
23.875	6.45e-16	1.12e-15	2.17e-16	2.92e-16	1.38e-16	4.03e-17	2.34e-17	8.67e-18
24.125	2.68e-16	1.51e-15	5.56e-16	1.57e-15	6.30e-17	8.90e-17	1.78e-17	2.97e-18
24.375	1.05e-14	5.42e-16	1.72e-15	3.71e-16	4.67e-16	7.72e-16	3.77e-17	3.25e-17
24.625	2.41e-15	6.10e-16	6.66e-16	1.23e-16	6.17e-17	9.77e-17	1.55e-17	4.50e-18
24.875	3.16e-16	4.96e-16	4.59e-16	1.46e-16	7.74e-17	1.65e-16	1.59e-17	4.67e-18
25.125	5.87e-16	4.03e-16	3.03e-15	2.38e-16	4.72e-16	1.44e-17	3.93e-17	3.48e-16
25.375	4.97e-16	6.03e-16	2.83e-16	1.06e-16	8.69e-17	1.14e-15	7.86e-18	1.16e-17
25.625	8.58e-16	4.58e-16	3.07e-16	9.74e-16	5.66e-17	4.39e-17	3.68e-18	8.67e-17
25.875	1.60e-16	4.90e-16	1.57e-16	1.23e-15	1.16e-16	3.03e-17	1.61e-17	3.14e-18
26.125	1.45e-16	2.75e-16	8.08e-17	2.73e-16	2.55e-17	1.69e-17	1.81e-17	7.51e-19
26.375	8.54e-17	4.01e-16	3.31e-16	1.21e-16	3.29e-17	1.50e-17	2.42e-18	1.29e-18
26.625	3.60e-16	3.85e-16	9.68e-17	6.83e-17	3.40e-17	1.43e-17	2.67e-17	1.88e-18
26.875	3.54e-16	1.29e-16	9.54e-17	5.71e-17	1.78e-17	1.04e-16	7.87e-17	6.71e-18
27.125	7.98e-17	3.19e-16	2.08e-16	6.26e-17	3.06e-17	3.69e-17	2.94e-17	4.18e-18
27.375	3.34e-17	1.32e-16	2.60e-16	2.89e-17	2.87e-17	4.40e-17	1.89e-17	2.26e-18
27.625	1.57e-15	2.24e-16	4.66e-17	1.73e-17	3.90e-17	3.42e-18	2.94e-17	0.00
27.875	5.57e-17	3.89e-16	9.64e-17	1.10e-17	7.65e-18	8.81e-18	1.19e-18	2.97e-18
28.125	2.53e-18	1.31e-16	1.72e-17	1.42e-17	4.59e-18	5.38e-18	2.28e-18	7.70e-19
28.375	7.51e-18	2.10e-16	3.35e-17	2.42e-17	3.94e-18	1.10e-18	2.55e-20	1.88e-22
28.625	1.96e-17	2.96e-17	4.67e-18	1.54e-18	4.88e-18	2.69e-18	2.80e-18	3.27e-19
28.875	2.61e-18	6.74e-19	1.65e-17	2.94e-17	1.11e-18	1.26e-18	0.00	1.85e-19
29.125	1.58e-19	3.50e-18	7.54e-19	1.80e-18	2.72e-19	0.00	0.00	0.00
29.375	0.00	0.00	0.00	8.49e-19	0.00	0.00	0.00	0.00
29.625	0.00	0.00	0.00	0.00	0.00	0.00	0.00	0.00
29.875	0.00	0.00	0.00	0.00	0.00	0.00	0.00	0.00

Bibliography

[1] J. Baumann, R. Gahler, J. Kalus and W. Mampe, Phys. Rev. D **37**, 3107 (1988).

[2] H. F. Dylla and J. G. King, Phys. Rev. A **7**, 1224 (1973).

[3] M. Marinelli and G. Morpurgo, Phys. Lett. **137B**, 439 (1984).

[4] R. Foot, H. Lew and R. R. Volkas, J. Phys. G **19**, 361 (1993).

[5] B. Holdom, Phys. Lett. **166B**, 196 (1986).

[6] B. Holdom, Phys. Lett. B **178**, 65 (1986).

[7] M. I. Dobroliubov and A. Yu. Ignatiev, Mod. Phys. Lett. A **8**, 917 (1993).

[8] Yu. Kobzarev, L. B. Okun, and I. Ya. Pomeranchuk, Sov. J. Nucl. Phys. **3**, 837 (1966).

[9] C. Caso *et al.* (Particle Data Group), European Phys. J. **C3**, 1 (1988).

[10] A. Yu. Ignatiev and G. C. Joshi, Phys. Rev. D **51**, 2411 (1995).

[11] K. S. Babu and R. R. Volkas, Phys. Rev. D **46**, R2764 (1992).

[12] OPAL Collaboration (R. Akers *et al.*), Z. Phys. C **67**, 203 (1995); ALEPH Collaboration (D. Buskulic *et al.*), Phys. Lett. B **303**, 198 (1993); A. Miyamoto, KEK-Preprint-90-42, Jun 1990, published in $\mathbf{Z^0}$ **Physics:** Proceedings, edited by J. Tran Thanh Van, Editions Frontieres, 1990, pg 127.

[13] CDF Collaboration (F. Abe *et al.*), Phys. Rev. D **46**, R1889 (1992).

[14] A. G. U. Perera, S. R. Betarbet, Byungsung O, and D. D. Coon, Phys. Rev. Lett. **70**, 1053 (1993).

[15] M. Mori *et al.,* Phys. Rev. D **43**, 2843 (1991).

[16] M. Aglietta *et al.,* Astropart. Phys. **2**, 29 (1994).

[17] N. M. Mar *et al.,* Phys. Rev. D **53**, 6017 (1996).

[18] P. F. Smith in **New and Exotic Phenomina:** Proceedings, edited by O. Fackler and J. Tran Thanh Van, Editions Frontieres, 1987, pg 527.

[19] G. Huentrup *et al.,* Phys. Rev. C **53**, 358 (1996); S. Cecchini *et al.,* Astropart. Phys. **1**, 369 (1993).

[20] S. Davidson, B. Campbell and D. Bailey, Phys. Rev. D **43**, 2314 (1991).

[21] A. Abbas, Phys. Today **52**, 81 (1999); Phys. Lett. B **238**, 344 (1990); J. Phys. G **16**, L163 (1990).

[22] C. Q. Geng, Phys. Rev. D **41**, 1292 (1990); C. Q. Geng and R. E. Marshak, Phys. Rev. D **39**, 693 (1989).

[23] K. S. Babu and R. N. Mohapatra, Phys. Rev. D **42**, 3866 (1990).

[24] X.-G. He, G. C. Joshi, and B. H. McKellar, Europhys. Lett. **10**, 709 (1989).

[25] P. A. M. Dirac, Proc. Roy. Soc. London **A133**, 60 (1931).

[26] for a comprehensive enumeration of grand unified models, see M. Gell-Mann, P. Ramond and R. Slansky, Rev. Mod. Phys. **50**, 721 (1978).

[27] footnote 10 of H. Georgi and S. L. Glashow, Phys. Rev. Lett. **32**, 438 (1974).

[28] L. B. Okun, M. B. Voloshin and V. I. Zakharov, Phys. Lett. **138B**, 115 (1984).

[29] Q. Shafi, **Cosmology and Elementary Particles:** Proceedings, Edited by D. R. Altschuler and J. F. Nieves, World Scientific, 1988, pg 168.

[30] R. Foot, H. Lew and R. R. Volkas, Phys. Lett. B **272**, 67 (1991).

[31] I. Antoniadis and K. Benakli, Phys. Lett. B **295**, 219 (1992).

[32] M. B. Green, Nature **314**, 409 (1985).

[33] E. W. Kolb, D. Seckel and M. S. Turner, Nature **314**, 415 (1985); FERMILAB-CONF-85/114-A, Aug 1985, published in **New Trends in Particle Theory:** Proceedings, Edited by L. Lusanna, World Scientific, 1985, pg 111.

[34] see, for instance, Yu. Kobzarev, L. B. Okun, and I. Ya. Pomeranchuk, Sov. J. Nucl. Phys. **3**, 837 (1966); R. Foot, H. Lew and R. R. Volkas, Phys. Lett. B **272**, 67 (1991).

[35] Z. G. Berezhiani, Acta Phys. Polon. B **27**, 1503 (1996); Z. G. Berezhiani and R. N. Mohapatra, Phys. Rev. D **52**, 6607 (1995); R. Foot and R. R. Volkas, Phys. Rev. D **52**, 6595 (1995).

[36] J. Maalampi and M. Roos, Phys. Rept. **186**, 53 (1990).

[37] E. D. Carlson and S. L. Glashow, Phys. Lett. B **193**, 168 (1987).

[38] E. W. Kolb, D. Seckel and M. S. Turner, Nature **314**, 415 (1985).

[39] Ya. M. Kramarovskii, B. M. Levin and V. P. Chechev, Sov. J. Nucl. Phys. **55**, 243 (1992).

[40] Z. G. Berezhiani, A. D. Dolgov and R. N. Mohapatra, Phys. Lett. B **375**, 26 (1996).

[41] S. L. Glashow, Phys. Lett. **167B**, 35 (1986).

[42] R. Foot and R. R. Volkas, Phys. Rev. D **52**, 6595 (1995).

[43] Z. G. Berezhiani and R. N. Mohapatra, Phys. Rev. D **52**, 6607 (1995); Z. G. Berezhiani, Acta Phys. Polon. B **27**, 1503 (1996); R. N. Mohapatra and V. L. Teplitz, Astrophys. J. **478**, 29 (1997).

[44] A. Yu. Ignatiev and G. C. Joshi, Phys. Lett. B **381**, 216 (1996).

[45] M. Suzuki, Phys. Rev. D **38**, 1544 (1988).

[46] A. Yu. Ignatiev, V. A. Kuzmin and M. E. Shaposhnikov, Phys. Lett. **84B**, 315 (1979).

[47] L. Davis Jr., A. S. Goldhaber and M. M. Neito, Phys. Rev. Lett. **35**, 1402 (1975).

[48] L. B. Okun and Ya. B. Zeldovich, Phys. Lett. **78B**, 597 (1978); S. Nussinov, Phys. Rev. Lett. **59**, 2401 (1987).

[49] M. Maruno, E. Takasugi and M. Tanaka, Prog. Theor. Phys. **86**, 907 (1991).

[50] E. Takasugi and M. Tanaka, Phys. Rev. D **44**, 3706 (1991).

[51] G. Barbiellini and G. Cocconi, Nature **329**, 21 (1987).

[52] E. Golowich and R. W. Robinett, Phys. Rev. D **35**, 391 (1987).

[53] T. Mitsui *et al.,* UT-ICEPP-93-02, January 1993.

[54] R. N. Mohapatra and S. Nussinov, Int. J. Mod. Phys. A **7**, 3817 (1992).

[55] M. I. Dobroliubov and A. Yu. Ignatiev, Phys. Rev. Lett. **65**, 679 (1990).

[56] R. N. Mohapatra and I. Z. Rothstein, Phys. Lett. B **247**, 593 (1990).

[57] S. Davidson and M. Peskin, Phys. Rev. D **49**, 2114 (1994).

[58] R. Foot and H. Lew, Mod. Phys. Lett. A **8**, 3767 (1993).

[59] J. Yang *et al.,* Astrophys. J. **281**, 493 (1984).

[60] S. Sarkar, asto-ph/9903183 (1999).

[61] M. S. Smith, L. Kawano and R. A. Malaney, Astrophys. J. Suppl. **85**, 219 (1993).

[62] R. Foot and R. R. Volkas, hep-ph/9904336 (1999); R. Foot, M. Thomson and R. R. Volkas, hep-ph/9509327 (1995).

[63] S. Davidson, private communication (1998).

[64] M. I. Dobroliubov and A. Yu. Ignatiev, Mod. Phys. Lett. A **8**, 917 (1993).

[65] B. Holdom, Phys. Lett. B **178**, 65 (1986).

[66] M. I. Dobroliubov and A. Yu. Ignatiev, Phys. Rev. Lett. **65**, 679 (1990).

[67] A. G. Wright, J. Phys. A **6**, 79 (1973).

[68] S. R. Kelner, Sov. J. Nucl. Phys. **5**, 778 (1967).

[69] R. P. Kokoulin and A. A. Petrukhin, Acta Phys. Acad. Sci. Hung. **29**, Suppl. 4, 277 (1970). (The effect of including the nuclear form factor is discussed in R. P. Kokoulin and A. A. Petrukhin, Proc. 12th Int. Conf. Cosmic Rays, Hobart **6**, 2436 (1971), but we were unable to obtain consistent results using the formula in this reference.)

[70] W. R. Nelson, R. Hirayama and D. W. O. Rogers, SLAC Report No. SLAC-265, 1985.

[71] C. Caso *et al.* (Particle Data Group), Eur. Phys. J. C **3**, 144 (1988).

[72] Particle Data Group, Eur. Phys. J. C **3**, 146 (1998).

[73] Y.-S. Tsai, Rev. Mod. Phys. **46**, 815 (1974).

[74] A. C. Hearn, RAND Publication CP78 (Rev. 7/95).

[75] G. Marsaglia and A. Zaman, Computers in Physics **8**, 117 (1994).

[76] W. R. Nelson, private communication.

[77] SLAC Radiation Physics Department report "NCRP Report No. 94" (1993).

[78] W. R. Nelson, SLAC Radiation Physics Note "RP-93-6" (1993).

[79] T. P. Marvin, SLAC-PUB-95-7042, 1995.

[80] C. Caso *et al.* (Particle Data Group), Eur. Phys. J. C **3**, 145 (1988).

[81] A. J. Shields, *et al.,* Appl. Phys. Lett. **76**, 3673 (2000).